Dissertation

submitted to the
Combined Faculties of the Natural Sciences
and for Mathematics
of the Ruperto-Carola University of
Heidelberg, Germany
for the degree of
Doctor of Natural Science

presented by
Dipl.-Phys. Christian Tapken

born in Westerstede, Germany

Oral examination: June 1st 2005

Lyα emission galaxies in the FORS Deep Field

Referees:

Prof. Dr. Immo Appenzeller

Prof. Dr. Klaus Meisenheimer

Zusammenfassung

Lyα-Emissionslinien-Galaxien im FORS Deep Field
VLT/FORS-Spektren mit einer Auflösung von $A \approx 2000$ von 18 Galaxien mit einer Rotverschiebung von $z = 2.7$ bis 5 werden präsentiert. Die Sternentstehungsraten der 18 Galaxien reichen von $UV_{\rm SFR} = 2$ bis 60 $\rm M_{\odot} yr^{-1}$ und ihre effektiven Radien von r <0.2 bis 1.8 kpc. Der Vergleich mit synthetischen Spektren ergibt, dass die Galaxien jung sind und ungefähr SMC/LMC-Metallizität haben. Die breiten, blauverschobenen, niedrig-angeregten interstellaren Absorptionslinien weisen darauf hin, dass die Galaxien Superwinde besitzen. Die Stärke dieser Absorptionslinien ist bestimmt durch die Geschwindigkeitsdispersion des ausströmenden Mediums und nicht durch dessen Abdeckungsgrad. Alle Spektren enthalten die Lyα-Linie, welche von reiner Absorption bis zu starker Emission (Emissions-EW = -20 bis 270 Å) reicht. Die meisten Emissionslinien sind asymmetrisch, drei Galaxien besitzen ein Lyα-Profil mit zwei Emissionskomponenten. Die asymmetrischen als auch die komplexeren Profile können mit einem kompakten Starburst erklärt werden, der von einer neutralen Schale umgeben ist. Die Stärke der Lyα-Emissionslinie wird durch die Entweichwahrscheinlichkeit der Lyα-Photonen bestimmt, welche wiederum durch die mittlere Geschwindigkeit, die Geschwindigkeitsdispersion und den Ionisationsgrad des ausströmenden Mediums bestimmt wird. Die mögliche Existenz einer zusätzlichen Galaxien-Population mit ausserordentlich starker Lyα-Emissionsline wird diskutiert.

Abstract

Lyα emission galaxies in the FORS Deep Field
VLT/FORS spectra with a resolution of $R \approx 2000$ of 18 galaxies in the redshift range of $z = 2.7$ to 5 are presented. The star-formation rates of the 18 galaxies range from $UV_{\rm SFR} = 1.2$ to 63.2 $\rm M_{\odot} yr^{-1}$ and their half-light radii from $r < 0.2$ to 1.8 kpc. A comparison of the rest-frame UV spectra with synthetic spectra show that the objects are young starburst galaxies with approximately SMC/LMC metalicity. The broad, blue-shifted, low-ionisation interstellar absorption lines indicate a galaxy-scale outflow. The strengths of these lines are found to be determined by the velocity dispersion and not by the covering fraction of the outflowing medium. Each spectrum includes the Lyα line, which ranges from pure absorption to strong emission (emission EW = -20 to 270 Å). Most of the lines show an asymmetric profile, three galaxies show a double-peak profile. The asymmetric and the double-peak profiles are explained by an expanding shell around a compact starburst region. The emission strength of the Lyα line is determined by the escape probability of the Lyα photons, which in turn depends on outflow velocity, velocity dispersion and the degree of ionisation of the outflowing material. The possibility of a distinct population, showing exceptionally strong Lyα emission, is discussed.

Contents

Chapter 1

Introduction

1.1 The formation and evolution of galaxies in the young universe

The Big Bang marks the beginning of the universe, which thereafter expanded and evolved into the universe we observe today. The cosmic microwave background displays the universe approximately 370 000 years after the Big Bang (Spergel et al. 2003). At this time the universe was very homogenous with only tiny density fluctuations, while 13.7 Gyr later the density fluctuations have evolved into the objects we know today: galaxies, stars, and planets. This process of formation and evolution of galaxies in the young universe is a widely discussed and analysed topic in modern astrophysics.

The structural growth is dominated by an unknown form of matter, which is called Cold Dark Matter. The Cold Dark Matter interacts only gravitationally. Under the influence of dark matter the structure collapse and form halos, which grows by infall of dark matter. The smaller halos will form first, since they are denser. The sequence of structural growth is called the hierarchical model, since the larger structures will form due to merging of smaller structures. The clustering and mass spectrum of dark halos can be calculated from a given cosmological model (Giavalisco 2002). Galaxies form within the potential well of dark halos when the cooled and condensed gas is converted into stars (White & Rees 1978). The supernovae and stellar winds of the newly formed stars have an impact on the surrounding medium, resulting in a feedback. The feedback is poorly understood, since it depends on the physics of star formation, which is up today not well understood.

Because the universe is expanding, the light of the galaxies is redshifted. The redshift z of a distant object is defined as

$$z = \lambda_{\text{observed}}/\lambda_{\text{lab}} - 1 \tag{1.1}$$

and is measured by the identification features in the spectra of galaxies. It is the one of the most important quantities for investigations of the high-redshift universe. Because the cosmological parameters have been measured by WMAP[1]

[1]Wilkinson Microwave Anisotropie Probe

and other observations very precisely (Spergel et al. 2003), the redshift can be accurately converted into physical parameters like the distance of the object or its age, when the light was emitted. Since light travels with a finite speed, the signal of high-redshift galaxies we observe today was emitted when the universe was much younger. The higher the redshift of an object, the larger is it distance and the younger it was, when its light was emitted. Hence when we observe galaxies at different redshifts, we see galaxies at different epochs of the universe. This fact enables us to witness the evolution of young galaxies into the galaxies we see today. On the other hand, looking at different redshifts, means that we not observe the same galaxies. To solve this problem we need to know how the galaxies of the local universe have looked like in the past to derive the evolution of galaxies correctly.

1.2 High-redshift galaxies

In the past ten years great improvements in the study of the young universe have been made. The 8-10 meter class telescopes have made it feasible to investigate details of the galaxies in the young universe. Moreover, the Hubble Space Telescope (HST) obtains deep images, allowing to see galaxies at high redshifts in great detail. Since these telescopes are optical and near infrared telescopes, the redshifted galaxies are observed mainly in the UV rest-frame. Hence physics and interpretation of UV spectra of high-redshift galaxies play an important role in understanding the galaxy evolution.

The observed continua in rest-frame UV spectra originate from young, massive O and B stars, which are up to few tens of millions years old. Thus the UV-bright galaxies are showing strong star formation and their spectra resembles those of local starburst galaxies. The UV-flux distribution are dominated by various types of absorption lines:

- The stellar photospheric lines are generated in the photospheres of stars
- Interstellar lines are caused by resonance transitions of species in the interstellar medium
- Stellar wind lines are generated in the radiatively driven wind of O and B stars

Moreover some nebular emission lines are sometimes visible, e.g. the Lyα emission line. The young stars ionise HII regions, resulting in recombination emission lines. The ratio of the emission lines can be used to determine the physical properties of the emitting HII region (Osterbrock 1989). The stellar photospheric lines are weak compared to the strongest interstellar absorption lines, which are in most cases saturated. In many high-redshift galaxies the interstellar absorption lines are blue-shifted with respect to nebular emission lines, which was firstly noted by Franx et al. (1997). Although the rest-frame UV spectra of high-redshift galaxies provide a wealth of spectral diagnostics, the weakness of the photospheric lines hamper the ability to derive the stellar content.

The majority of the identified high-redshift galaxies were detected on the basis of their UV colours. High-redshift galaxies show a significant decrease of flux

shortward of 912 Å and of 1216 Å. Photons with a wavelength lower than 912 Å can ionise neutral hydrogen and hence are easily absorbed by neutral hydrogen in the galaxy itself or not fully ionised regions of the intergalactic medium (IGM). Photons with a wavelength below 1216 Å are absorbed by Lyα in the intervening IGM. The so-called Lyman-break galaxies are selected by this continuum steps describes above, using three filters (for a review see Giavalisco 2002). The Lyman-break criterion only identifies candidates in a certain redshift range, while the more sophisticated technique of photometric redshift (Gabasch et al. 2004a) uses more filters to derive a redshift and a type, based on the spectral properties of the galaxy. Since selection by the Lyman-break proved as very efficient in terms of telescope time, a large sample of high-redshift galaxies was derived. Shapley et al. (2003) presented the spectra of 798 galaxies at a redshift of ≈ 3. Some high-redshift galaxies have been found on basis of their sub-millimeter and radio emission (Chapman et al. 2004). Moreover many galaxies especially in the high-redshift universe have been found by means of a strong Lyα line (e.g., Hu et al. 2004). All these galaxies are only a part of the complete galaxy population at high-redshift. To compare the physical properties of galaxies at different redshift is necessary to understand the different selection criteria.

1.3 Lyα emission galaxies (LAEs)

Partridge & Peebles (1967) pointed out that young primordial galaxies may have a strong Lyα line and hence could be detected in narrow-band searches out to high redshifts. Subsequently many workers tried to detect the Lyα emission of high-redshift galaxies. For many years the searches were not successful (e.g. Thompson & Djorgovski 1995 or Pritchet 1994). Hu & McMahon (1996) and Djorgovski et al. (1996) discovered the first galaxies with strong Lyα emission not powered by an active galactic nuclei (AGN). Since these discoveries many high-redshift galaxies with a strong Lyα line have been found, the so-called Lyα emission galaxies (LAEs) (for a review see Taniguchi et al. 2003). LAEs are now widely detected in narrow-band searches (e.g., Hu et al. 2004). There are various physical properties of the young universe that can be derived from LAEs like the star-formation rate density (Ajiki et al. 2003) or the epoch of reionisation (Rhoads et al. 2004). Moreover, their luminosity function can be compared to theoretical models (Thommes & Meisenheimer 2005).

Despite the fact that LAEs are widely used to, e.g., derive the star formation rate, the cause of the strong Lyα emission is still debated. It is assumed that the Lyα photons are produced by recombination in HII region ionised by young stars, although the role of shocks by supernovae is unsolved. Charlot & Fall (1993) finds a negligible contribution of supernova shells to the Lyα flux, while Bithell (1991) finds the opposite. Active Galactic Nuclei (AGN) seem not to play an important role, since X-rays surveys did not detect a strong contribution of AGNs (Wang et al. 2004). While the production of Lyα photons is rather well understood, the fraction of Lyα photons, which can escape the star-forming regions, is difficult to calculate. Since Lyα is a resonance line, neutral hydrogen absorbs and re-emits Lyα photons in random directions. Hence the Lyα photons have a longer optical

path compared to UV-photons with a slightly higher or lower wavelength. With each scattering event the frequency of the Lyα photons is shifted. The photons will diffuse in physical and frequency space. Photons with a strongly shifted frequency are far less likely to be absorbed by neutral hydrogen and hence have higher escape probability. Many theoretical efforts have been made to treat the radiation transfer of resonance lines, both numerically (Auer 1968; Adams 1972; Ahn et al. 2001) and analytically (e.g., Osterbrock 1962 and Neufeld 1990).

The interstellar medium in galaxies consists of several components, including dust. The amount of the dust extinction (scattering and absorption) is decreasing with increasing wavelength and is strongest in the UV. The light of galaxies is absorbed in the UV and re-emitted by the heated dust particles in the far-infrared. Any dust distributed uniformly in a neutral medium would affect the Lyα photons more strongly as UV-continuum photons, since the Lyα photons have an increased optical path. Large amounts of neutral hydrogen and dust can even affect the stellar continuum (Chen & Neufeld 1994), leading to a strong absorption of Lyα in high-redshift galaxy spectra as observed by, e.g., Shapley et al. (2003). For a long time the high probability of absorption of Lyα photons was an explanation for the non-detection of strong Lyα emitters in the young universe (Pritchet 1994) and the weak Lyα emission compared to the continuum in local starburst galaxies. The strong Lyα emitters found in the young universe have been explained in this model to be dust-free galaxies (Kudritzki et al. 2000).

But soon it was realized that this simple picture may not be valid. Giavalisco et al. (1996) found no strong relation between the attenuation of the galaxy and the Lyα equivalent width. In addition extreme metal-deficient galaxies, and thus galaxies with a very small amount of dust, can show no Lyα emission at all (Kunth et al. 1998). These results are in contradiction to the expectation that the amount of dust is the most important factor determining the detectability of Lyα emission. The spatial distribution of the dust relative to the neutral hydrogen, as demonstrated by Neufeld (1991), plays also an important role. He showed that in a two-phase interstellar medium, Lyα can even be less affected by dust than the continuum radiation.

In the local universe Kunth et al. (1998) found strong indications that a large-scale outflow is responsible for the detection of Lyα photons. Blue-shifted neutral hydrogen will not absorb Lyα photons generated at the system velocity of the galaxy. Dawson et al. (2002) have presented evidence that for high-redshift galaxies the superwind is an important factor for the escape of Lyα photons.

Recent studies of Shapley et al. (2003) and Noll et al. (2004) show a variety of the Lyα line properties in the spectra of UV-bright high-redshift galaxies. The Lyα is observed in absorption, or in emission plus absorption, or emission alone. This variety of the Lyα line and the physical reasons for the strength of this line are not well understood.

1.4 The aim of this thesis

Observations of galaxies with strong Lyα emission are an important test of current scenarios of galaxy formation and evolution, but these galaxies are not well under-

stood. Various suggestions have been made to explain the origin of the strong Lyα line. The theoretical situation is sufficiently complex and requires observational tests. Thus the aim of this thesis is to analyse a meaningful sample of high-redshift galaxies showing Lyα in emission and to derive the origin of this Lyα emission, the evolutionary state and the physical properties of this galaxies. The galaxies are analysed by obtaining medium-resolution spectra of the UV rest-frame, including the Lyα line. Analysing the Lyα line profiles will help to determine the state of the interstellar medium in these galaxies and to constrain the production mechanism of the Lyα photons. The rest-frame UV spectral features produced by young stars are used to analyse the evolutionary state and the starburst properties. Also the kinematics of the interstellar medium are investigated. The detailed analysis of the rest-frame UV spectra of the galaxies shall allow us to determine the production mechanisms of the Lyα photons and the parameters which influence their escape probability.

Chapter 2

Observations and data reduction

One objective of this work is to analyse Lyα profiles of high-redshift galaxies. Comparison with low-redshift objects (Kunth et al. 1998) and existing studies of high-redshift galaxies (e.g. Dawson et al. 2002) demonstrate that a resolution element of $\delta v \approx 100$ km/s (which converts to a medium spectral resolution of $R = \frac{\lambda}{\delta\lambda} \approx 3000$) should be achieved to investigate the kinematics of the LAEs. Instruments capable of obtaining many medium-resolution spectra with one exposure cannot provide medium-resolution spectra with a wide spectral range. Echelle spectrographs can provide spectra of high-resolution with large spectral range, but they lack (up today) the capability of obtaining many spectra with one exposure. A limited spectral range has the disadvantage that only a few spectral features are observed. The object cannot be classified and hence no redshift or any other information can be derived from medium-resolution spectra. Therefore they are not well suited for classifying objects, which are not or little constrained by further observations. The small spectral range also limits the possibility to derive further information on the galaxies. To save observing time and to derive as much information as possible on the objects, an existing photometric and spectroscopic survey was used to select and analyse the objects. For this study the FORS Deep Field was chosen and in the following the advantages of the FORS Deep Field survey are presented. Moreover, the selection criteria for the follow up medium-resolution spectroscopy and the reduction of the this spectra are described.

2.1 The FORS Deep Field

The FORS Deep Field (FDF) is a deep photometric and spectroscopic survey (Appenzeller et al. 2000) carried out with the FORS instrument at the Very Large Telescope (VLT). The aim of the FDF is to study the formation and evolution of galaxies, especially in the young universe. The FORS Deep Field has an area of 7 ' $\times$ 7' and is four times larger than the two Hubble Deep Fields combined. The FORS Deep Field is located near the south galactic pole, resulting in a low Galactic extinction. The basic strategy of the FORS Deep Field was to obtain deep broadband photometry, which formed the basis for photometric redshifts. This

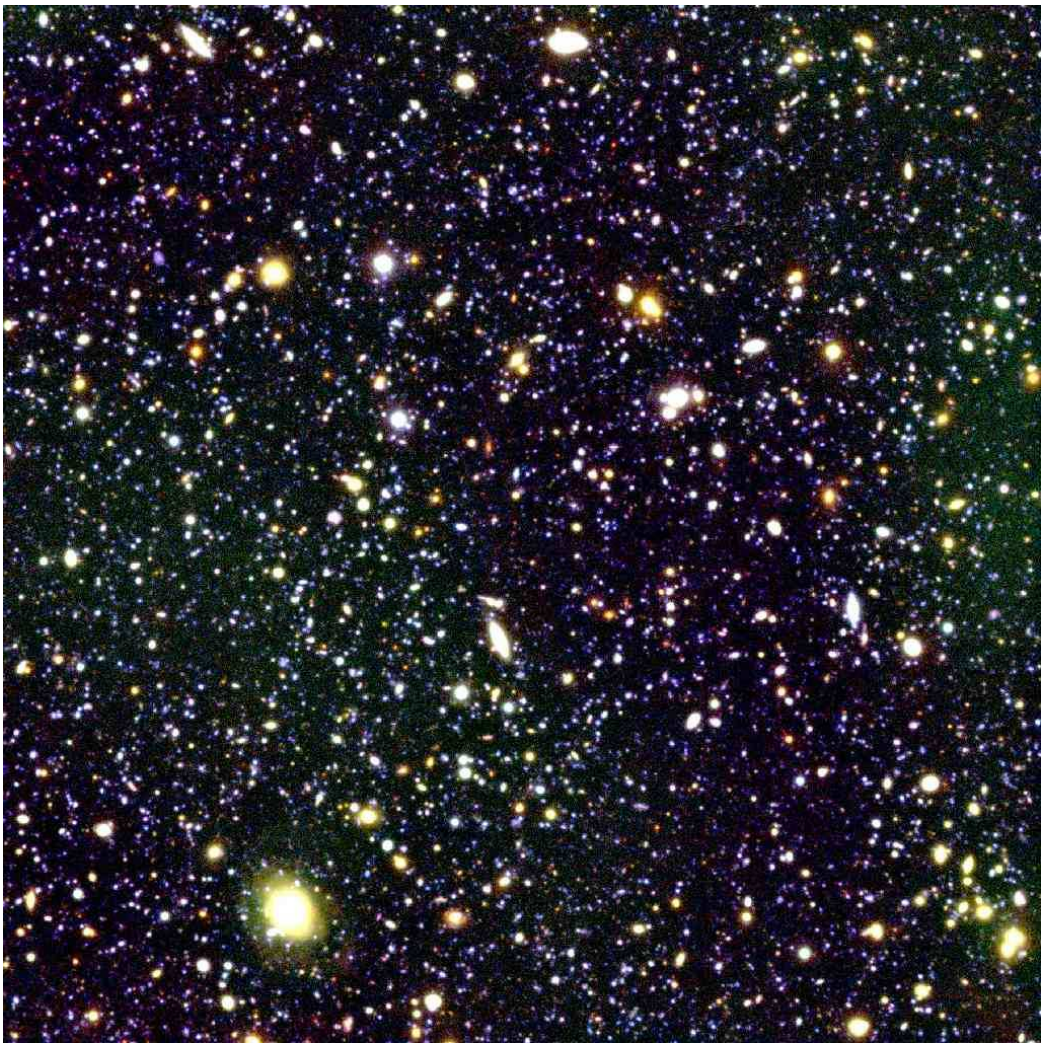

Figure 2.1: BRI composite image of the FORS Deep Field (by Jochen Heidt). North is up, east is left. Most of the objects seen are distant galaxies.

allowed, e.g., the selection of galaxies at high-redshift for a spectroscopic survey. High signal-to-noise spectra with a low resolution of $R \approx 200$ of a well defined sample of high-redshift galaxies were obtained in this FDF spectroscopic survey (Noll et al. 2004). Several studies based on the FDF improved our understanding of the galaxies in the young universe, e.g. the chemical evolution of high-redshift galaxies (Mehlert et al. 2002), the metal absorption systems in the continuum flux of the QSO[1] Q0103-260 using $R \approx 40000$ spectra (Frank et al. 2003), the evolution of the luminosity function and the star formation rate in the FDF (Gabasch et al. 2004a,b).

The deep photometry and the well defined sample of the FDF spectroscopic survey formed the basis for the studies of this work.

[1]Quasi-Stellar Objects

Table 2.1: Characteristics of the FDF (Heidt et al. 2003)

Field centre	$1^h6^m3^s$ -25^{o}45'46" (2000)
mean E(B-V)	0.018 mag
HI column density	1.92×10^{20} cm^{-2}
Radio sources	none with flux > 2.5 mJy
Bright stars (<5 mag)	none within 5^o

Table 2.2: Overview of the broadband observations (Heidt et al. 2003). The seeing given is by the width, $FWHM$(full width half maximum), of the point spread function. The 50 % completeness limit is the magnitude, to which the FDF is 50 % complete for a point source.

Filter	Exposure time [s]	$FWHM$["]	50 % completeness limit [mag]
U	44400	0.97	25.64
B	22650	0.60	27.69
g	22145	0.87	26.86
R	26400	0.75	26.68
I	24900	0.53	26.37
J	4800	1.20	22.85
Ks	4800	1.24	20.73

2.1.1 Characteristics and photometry of the FDF

Characteristics of the FDF

The field selection and characteristics of the FDF are described in Heidt et al. (2003). The important ones are summarised in Table 2.1.

To obtain photometry of faint extragalactic objects, the FDF was chosen to have a low galactic extinction. Moreover no bright stars are within the FDF avoiding saturation of the CCD. Very bright stars in the surrounding of the FDF are absent to avoid stray light. The FDF was also selected because the bright radio-quiet QSO Q0103-260 is located at a redshift of z = 3.36 in the field. The richly structured Lyα forest observed in the spectrum of the QSO allows the study of the intergalactic medium along the line-of-sight of the QSO. Since a representative study of the distant universe is intended, a field with apparently no galaxy cluster was selected. However the photometric redshifts showed that a galaxy cluster at a redshift of $z = 0.33$ is located in the south west part of the FDF.

Photometric observations and catalog

The FDF survey consists of deep optical U, B, g, R, I observations obtained with FORS at the VLT and near-infrared J and Ks observations obtained with SoFI at the ESO-NTT (Heidt et al. 2003). Table 2.2 provides an overview of the broadband observations. The magnitudes in Heidt et al. (2003) and in this work are in the Vega magnitude system. Based on these observations a B and I selected catalog was generated (Heidt et al. 2003), which contains 8753 objects.

Additional narrow-band images centred at 4850, 5300, 8100, 8150, 8230 and 8340

Å have been obtained. The reduction and analysis will be described in forthcoming paper. Additionally the FDF was observed with the Very Large Arey (VLA) at 1.6 GHz and 5 GHz. A preliminary catalog of radio sources has been obtained (Wagner, private communication).

The FORS Deep Field was observed with the Advanced Camera for Survey (ACS) on board of the Hubble Space Telescope (HST) using the I-band filter F814W in autumn 2002. The FDF was covered in four pointings, resulting in an area nearly as large as the field covered by FORS. Each pointing was observed for a total of 40 min. Pannella (private communications) subtracted the bias, corrected the flatfield and obtained a photometric calibration using the CALACS software. The final combined image, which has a pixel scale of 0.05"/pixel, was obtained by the multi-drizzle task (Pannella, private communications). The cosmics were not removed in an optimal way in the final image and hence masking during the analysis of the image is necessary. The variations of the point-spread-function on position within an ACS frame is small (5%, Pannella, private communications).

2.1.2 FDF spectroscopic survey

The FDF spectroscopic survey has been carried out as part of the FORS Deep Field survey (Noll et al. 2004). It aimed to obtaining high signal-to-noise ratio (≈10), low-resolution spectra (R≈200) of a well defined sample of high-redshift galaxies. The high signal-to-noise ratio allows investigations of the galaxies in detail. The low-resolution results in a large wavelength range, guaranteeing many observable spectral features. Since this survey forms the basis of this work and the low-resolution spectra are used to derive physical information on the selected galaxies, the main properties of the survey are described.

Selection of galaxies

The galaxies were selected on basis of the deep photometric observations, which allowed to derive photometric redshifts (Bender et al. 2001; Gabasch et al. 2004a). The photometric redshifts were improved during the course of the survey since additional photometric observations were obtained. In addition the existing photometric observations were reduced with higher quality and the first spectroscopic results helped to calibrate the photometric redshifts. The fraction of misidentification at the end of the FDF spectroscopic survey amounts to few percent and the rms error of $z_{\rm phot} - z_{\rm spec}$ is ≈ 0.13 (Noll et al. 2004). The majority of the objects were selected as intrinsically bright galaxies with a redshift between 1 and 5. The selection criterion for galaxies between $z_{\rm phot} = 2.0$ and 4.0 are $m_{\rm I} \leq 24.5$ mag. About half of the galaxies with $m_{\rm I} \leq 24.0$ mag and $z_{\rm phot} = 2.0$ to 4.0 were observed in the FDF spectroscopic survey. About one third of the galaxies with $m_{\rm I} \leq 25.0$ mag and $z_{\rm phot} > 4.0$ were observed. Three additional objects were selected on basis of narrow-band photometry in the vicinity of the QSO Q 0130-260 and four galaxies were selected on the basis of a g-Band excess.

The deep broadband photometry and the excellent photometric redshifts allowed to search for LAE candidates on basis of broadband filters. Galaxies with strong Lyα emissions should have an accurate photometric redshift, but have an excess

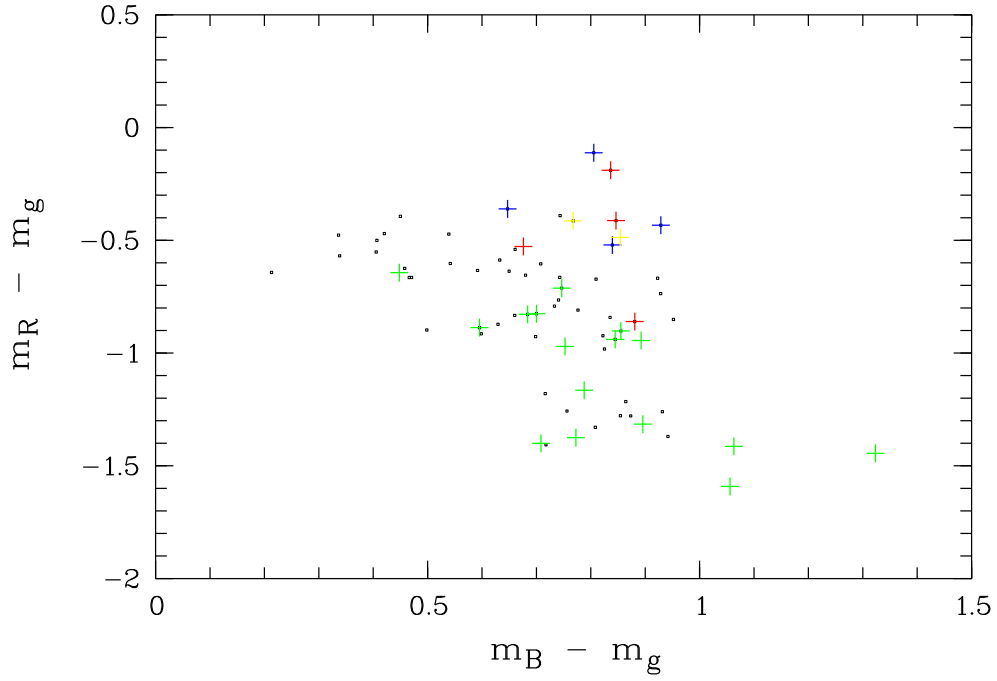

Figure 2.2: Colour-colour diagram of galaxies in the FDF with $z_{\rm phot} = 2.7$ to 3.4 and $m_{\rm g} <$ 26 mag (dots). Red crosses indicates galaxies with a strong Lyα line, yellow crosses indicates quasars, green crosses indicates high-redshift galaxies with no or weak Lyα emission. Blue crosses indicates the galaxies which have been selected for follow-up spectroscopic.

in the filter covering the Lyα emission. The Gunn g filter was chosen to search for an excess, because it is relatively narrow and not contaminated by strong sky emission. A colour-colour diagram was created with galaxies having a photometric redshift of $z_{\rm phot} = 2.7$ to 3.4 (see Fig. 2.2). Galaxies already identified as Lyα emission galaxies (red crosses) or galaxies with Lyα in absorption (green crosses) are displayed in the colour-colour diagram. A region around the known galaxies with strong Lyα emission was selected as a likely region and four galaxies were chosen as LAE candidates (blue crosses in Fig. 2.2). They were observed in the course of the FDF low-resolution spectroscopic survey. Three (FDF-7644, FDF-7452, and FDF-8215) of the four galaxies show a strong Lyα emission (Noll et al. 2004).

Also a number of galaxies was observed serendipitously as they were caught by the slits.

Observations and data reduction

The spectroscopic observations were carried out with FORS1 and FORS2 at the ESO VLT at Paranal, Chile. The spectroscopic observations were obtained in the modes MOS and MXU, allowing the simultaneous observations up to 40 objects. The grism[2] 150I and a slit width of 1" were used. The spectra cover a wavelength

[2]Grism is combination of a transmission GRating and a prISM

range of 3400 Å to 10000 Å and have a resolution of $R \approx 200$. To achieve a high signal-to-noise an integration time up to 10 h per object was scheduled. The observations were carried out in several runs, reaching a total integration time of 63.7 h.

The spectra were reduced using MIDAS (Munich Image Data Analysis System). The co-added one-dimensional spectra were corrected for Galactic extinction, slit losses and the atmospheric B and A absorption bands were removed. For further details of the data reduction we refer to Noll (2002) and Noll et al. (2004).

Spectroscopic catalog

604 one-dimensional spectra were reduced. Noll et al. (2004) derived the redshift and a type based on the spectrum of the object. The catalog of Noll et al. (2004) lists 341 objects with secure or probable redshifts. The object number (ID) is taken from Heidt et al. (2003). For objects which are not included in the photometric catalog numbers starting with 9001 have been assigned. The spectroscopic catalog gives the redshift, spectral type, SNR, quality of the spectrum and further information.

Some galaxies in the FDF spectroscopic catalog show only one conspicuous feature, a strong emission line. The classification based on one spectral feature is not very reliable. However the deep spectroscopic observations usually allow to detect a second feature, a continuum break at the wavelength of the emission line. This continuum break and the absence of other emission features over a broad spectral range allows the identification of the single emission as Lyα.

2.2 The medium-resolution spectra

2.2.1 Target selection for the medium-resolution spectroscopy

Two different selection criteria were applied to select candidates for medium-resolution spectroscopy. First, galaxies with strong Lyα emission were selected. Secondly, UV-bright continuum galaxies were selected. The rest-frame UV spectra show in the range of 1200 to 1800 Å several absorption features, allowing to derive the physical properties of starburst galaxies. The spectra of the FDF spectroscopic survey have low-resolution, which do not allow to detect photospheric lines and to distinguish between stellar and interstellar absorption lines.

FORS2 has the capability to obtain spectra of many objects with a medium-resolution in one exposure and thus was selected for observing the high-redshift galaxies. Comparing the redshift distribution and the wavelength range of the grisms, two grisms are suitable at FORS2: 1400V (central wavelength $\lambda = 5200$ Å) and 1200R (central wavelength $\lambda = 6500$ Å). The galaxies were selected in a way that the spectral feature(s) fall into the wavelength range of the grisms and that the signal-to-noise ratio is sufficiently high. For the 1400V (1200R) grism UV-bright continuum galaxies with $z = 2.3 - 3.5$ ($z = 3.0 - 3.5$) and $m_{\rm g} \leq 24.5$ mag ($m_{\rm R} \leq 24.5$ mag) were selected. Moreover galaxies with a Lyα emission strength of $F_{\rm Ly\alpha} \geq 30\ (20) \times 10^{-21}{\rm Wm}^{-2}$ at $z = 3.0 - 3.5$ ($z = 4.5 - 5$) were selected.

2.2.2 Observation

All medium-resolution spectra were obtained with the Very Large Telescope (VLT) and FORS2. The VLT, located at Paranal, Chile, consists of four 8.2 meter ground-based telescopes. It is run by the European Southern Observatory (ESO). The four telescopes can be operated in single mode or can be combined for interferometry. FORS 2, and its twin instrument FORS1, were build by a German consortium run by the Landessternwarte Heidelberg (Appenzeller et al. 1998). FORS (FOcal Reducer Spectrograph) is an imager/spectrograph for the optical wavelength range.

The observations were obtained with FORS2 at VLT-UT4 using the holographic grisms 1400V (Prop. ID: 69.A-0105) and 1200R (Prop. ID: 71.A-0307). Both setups (1200R and 1400V grism) were observed in service mode using one MXU mask each, allowing a flexible selection of targets[3]. The FORS2 detector consists of two 2k × 4k MIT CCD[4] chips, which were used in the 100kHz readout mode with high gain (see FORS Manual for details). A 2×2 binning was performed during the readout.

The observations with the 1400V grism were carried out during August 2002 (see Table A.1 for details). The 1400V grism has a wavelength range from 4560 Å to 5860 Å and a resolution of R = 2100 (Pixel scale = 0.62 Å / rebinned pixel). Eight single exposures with 47 min integration time resulted in a total integration time of 6.25 h. The average seeing was 0.81 ".

The observations with the 1200R grism were carried out during July - September 2003 (see Table A.2 for details). The 1200R grism has a wavelength range of 5750 Å to 7310 Å and a resolution of R = 2140 (Pixel scale = 0.76 Å / rebinned pixel). 14 single exposures with a total integration time of 10.05 h were obtained. One exposure was excluded from the reduction process, because of moonlight contamination, decreasing the total effective integration time to 9.45 h. The average seeing was 0.92".

2.2.3 Data reduction

MIDAS [5] with the programme package MOS allows the reduction of Multi-Object Spectrocopy. Special routines were added to MOS by W. Fürtig, S. Möhler, O. Stahl, E. Sutorius and T. Szeifert to extract FORS spectra. S. Noll used this programme package in his PhD-Thesis to reduce the low-resolution spectra of the FDF spectroscopic survey (Noll 2002; Noll et al. 2004). The reduction of the medium-resolution spectra of this work were done using this MIDAS-MOS programme packages, too.

The reduction of spectra of faint objects is hampered by the fact that the surface brightness of the sky is much brighter the objects. The medium-resolution spectra have also the disadvantage that the flux per pixel is very low, which makes the object detection difficult. The reduction has to achieve an optimal reduction of the weak signal and to prevent systematic errors. The overall strategy is to cali-

[3]The so-called MXU masks are cutted by laser, allowing a high degree of freedom
[4]Charged coupled device
[5]Munich Image Data Analysis System, devoloped and maintained by ESO

brate each two-dimensional spectrum and to extract the one-dimensional spectra with an signal-to-noise optimising algorithm. The one-dimensional spectra are then co-added signal-to-noise weighted. Also a noise function is generated during the extraction of the one-dimensional spectra, and is used to derive the noise function of the co-added spectra.

The reduction consists of the following steps:

- Bias subtraction
- Distortion correction
- Flatfield correction
- Wavelength calibration
- Sky subtraction
- Extraction of the one-dimensional spectra using the Horne-algorithm
- Absolute wavelength corrections
- Co-addition of the spectra
- Response function correction

Bias subtraction

To each image a constant value (bias) is added during the readout. This offset has to be determined and subtracted. A master bias image is generated from bias images provided by ESO. Each raw image is corrected by subtracting the master bias.

Distortion correction

The spectra obtained with FORS2 show a distortion, depending on the position in x and y. The distortion is increasing towards the outer parts of the CCD chip. To extract very faint objects is necessary to correct for this effect. The two-dimensional spectra are rectified by rebinning. The spatial upper and lower boundaries of the spectra are determined as a function of dispersion. The boundaries is described by a polynomial, which is used to rebin the spectra. Since this process is increasing the noise and hampering the detection of cosmics, only the most distorted spectra were rebinned.

Flatfield correction

Pixel defects and different pixel sensitivity are corrected by division with a flat field. Internal screen flats are obtained during the daytime with a calibration unit by observing a homogeneous light source. The flatfields are obtained with the same setup as the spectroscopic science images. A master flatfield is then generated by co-adding the screen flats. Since only pixel to pixel variations have to be corrected, the master flatfield is normalised using a median filter. The science images are corrected by dividing by this normalised master flatfield.

Wavelength calibration

The wavelength calibration converts the units of the dispersion axis from a pixel scale to a physical scale. The wavelength calibration is achieved in two steps. First a dispersion relation is generated, secondly the spectra are rebinned. The dispersion relation is derived from wavelength calibration images, which are obtained by observing gas discharge lamps, producing well defined lines. The procedure calculates a first dispersion relation using grism parameters, searches for lamp emission lines, determines the position using a Gauss-fit, and identifies the lines on the basis of the first dispersion relation. The dispersion relation is obtained by fitting the wavelengths and the x-positions by a polynomial of usually fourth order. To minimise errors due to statistical fluctuations the positions are fitted by a polynomial of second order in spatial direction when obtaining the dispersion relation. The two-dimensional spectra are rebinned using the dispersion relation. The rebinned pixel scale is 0.5 Å per pixel. The relative accuracy of the wavelength calibration is usually 1/10 of a pixel.

Sky subtraction

Since the surface brightness of the sky is much brighter than that of the objects, the sky subtraction is a crucial step in the reduction. Before subtracting the sky, the object position on the two-dimensional spectra has to be defined. For this purpose the pixels are added up along the dispersion direction and the spatial profile of the slit is plotted. The reference regions of the object and of the sky are defined interactively. For very faint objects the two-dimensional spectra are co-added and the spatial profile is derived for the co-added two-dimensional spectra. After the reference area of the object and of the sky is defined, the sky along the slit is approximated on basis of the sky in the sky reference area. There are two ways in extrapolating the sky, a polynomial fit and a median filter. The sky in the sky reference area is interpolated by polynomial fits of first, second or (only in a very few cases) higher order. Alternatively the sky is smoothed by a median filter using a width of 7 to 15 pixel. After smoothing the sky in the reference area of the sky, the sky in the reference area of the object is derived by a linear interpolation between the smoothed sky values at pixels below and above the reference area of the object.

Extraction of the one-dimensional spectra

The extraction of the one-dimensional spectra is done with the algorithm of Horne (1986). The advantages of the Horne algorithm are a signal-to-noise optimised extraction, rejection of cosmics[6] and providing an error function based on the noise statistic. The extraction of the one-dimensional spectra consists of the following steps:

- Extraction of a standard spectrum
- Construction of a spatial profile

[6]Cosmics are traces caused by cosmic rays and natural radio activity

- Masking cosmics
- Extraction of the optimal spectrum

Extraction of a standard spectrum: The algorithm needs start values for the derivation of the optimal spectrum. A standard spectrum is computed by summing up pixels along the spatial direction for each bin along the direction of dispersion. The noise function is derived from the noise statistics and the readout noise.

Construction of a spatial profile: The algorithm of Horne sums over the pixels with a weight optimising the signal-to-noise ratio. To calculate the signal-to-noise the spatial profile is derived. The algorithm only assumes that the spatial profile is a smooth function of wavelength. For non-resolved high-redshift galaxies this assumption is justified. A polynomial of a high order is fitted along the dispersion direction for each spatial bin. The spatial profile is determined for each dispersion bin by evaluating the values of the polynomial fits along the dispersion direction.

Masking cosmics: With the given spatial profile, any outliers, like cosmics, can be identified. The advantage of this approach is that strong emission lines are not rejected, but cosmics are identified as outliers and are masked.

Extraction of the optimal spectrum: The pixels along the spatial direction are summed up. The weight is derived from the spatial profile, giving pixels with an expected lower signal-to-noise less weight. Pixels affected by cosmics are omitted. Also a noise function based on the statistics and the readout noise is derived. The noise function is mainly given by the Poisson error of the detected electrons. Since removing cosmics changes the spatial profile an iteration of the last three steps is necessary, until the optimal spectrum is becoming stable.

Relative flux calibration

For flux calibration standard stars are observed during the observing nights with the same instrument configuration as the science exposures. A response function is generated from these observations to correct for the wavelength-dependent efficiency of the instrumental setup. The one-dimensional spectra are corrected for atmospheric extinction.

Absolute wavelength calibration

The relative wavelength calibration is achieved by calibrating the science frames with wavelength calibration images. The daytime calibration images are obtained in zenith position and thus the science frames are usually obtained at a different telescope position. This can cause a small shift in the dispersion direction. This effect is determined and if necessary corrected, using sky lines, namely [OI] 5577.3 Å and [OI] 6300.31 Å. Both lines are strong and stable in wavelength. Finally the spectrum is rebinned linearly. During the rebinning the spectra are shifted into the

heliocentric reference frame and are transformed from air to vacuum wavelengths. The last two steps are incorporated into the absolute wavelength calibration to decrease the amount of smoothing by multiple rebinning.

Co-addition of the spectra

The spectra are signal-to-noise weighted and co-added, removing persistent cosmics with a sigma-clipping. The pixels are signal-to-noise weighted and according to:

$$F(\lambda) = 1/\sum(1/E_{\rm i}(\lambda)^2) \times \sum(M_{\rm i}F_{\rm i}(\lambda)/E_{\rm i}(\lambda)^2) \tag{2.1}$$

co-added. $F_{\rm i}$ is the i spectrum and $E_{\rm i}$ the corresponding error function. $M_{\rm i}(\lambda)$ is a mask and can have the values 0,1. The mask is generated by firstly deriving the median function $F_{\rm (med)}(\lambda)$ of the spectra. Using this median, values of $F_{\rm i}(\lambda)$ are excluded by setting $M_{\rm i}(\lambda) = 0$ if $F_{\rm i}(\lambda) \leq F_{\rm (med)}(\lambda) - 10 \times E_{\rm i}(\lambda)$ or $F_{\rm i}(\lambda) \geq F_{\rm (med)}(\lambda) + 10 \times E_{\rm i}(\lambda)$.

Since the noise function produced by the Horne-algorithm does not include noise contribution introduced by the sky subtraction and flatfield correction, a mean error is also calculated according to:

$$\sigma_i = \sqrt{1/n * (\sum(F_{\rm i}(\lambda) - F(\lambda))^2)}, \tag{2.2}$$

where n is the number of the spectra.

Absolute flux calibration

The absolute flux calibration has to correct for the slit-losses, the galactic extinction and for a varying response function. The holographic grisms used in this work have the disadvantage of a varying response function, which depends strongly on the incident angle of the light. The response function shifts towards redder or bluer wavelengths dependent of the position of the object in the telescope focal plane. Since the response function is generated by observing standard stars with a certain position, the response function is only valid for this position. The low-resolution spectra of Noll et al. (2004) are obtained with a normal grism, which show a much smaller variation of the response function. They are also corrected for slit-losses and the Galactic extinction. Hence for all medium-resolution spectra of objects with existing low-resolution spectra, the spectra of Noll et al. (2004) were used to correct for this effect. The corresponding low- and medium resolution spectra were divided and the resulting function was fitted by a low-order polynomial fit. The medium-resolution spectra are corrected with this polynomial fit. Some objects were only observed with medium-resolution spectra. The varying response function was corrected by means the sky background. The sky was extracted from all slits and was divided by the sky in those slits, which had almost the same position as the corresponding slits used in the standard star calibration exposures. The divided sky shows the correction of the response function and was fitted by a low-order polynome. The spectra were corrected with this function. This procedure has been verified with spectra which have been corrected with low-resolution data. The aperture photometry of Heidt et al. (2003) has been used to determine and

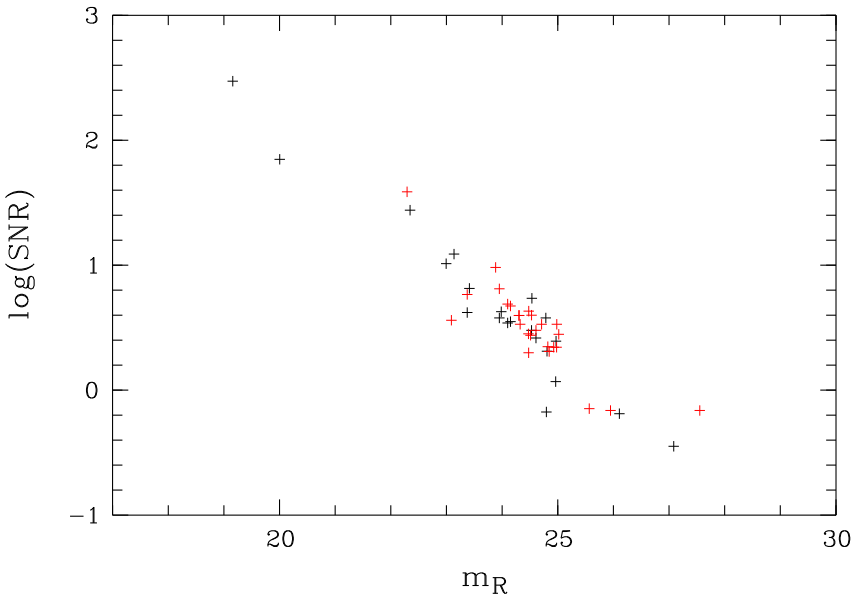

Figure 2.3: The average continuum signal-to-noise ratio as a function of the magnitude. Black crosses correspond to the spectra of the 1400V setup and red crosses correspond to the 1200R setup.

correct for slit-losses. After the correction of the slit-losses the Galactic extinction (see Noll et al. 2004 for details) has been corrected.

2.2.4 Results of the medium-resolution spectroscopy

Tables A.3 and A.4 list objects with reduced spectra. The wavelength range and the average continuum signal-to-noise ratio per resolution element of each spectrum are also in the tables included. 22 spectra in the 1400V setup, have been reduced and 27 spectra in the 1200R setup. 43 objects have been observed, 6 objects are included in both setups. The wavelength range for each setup is narrow ($\approx$ 1300 Å for the 1400V setup and 1500 Å for the 1200R setup in the observed wavelength range). In Fig. 2.3 the average signal-to-noise ratio measured in the complete wavelength range of the grisms is plotted against the magnitude $m_{\rm R}$. The magnitudes of most of the targets are between $m_{\rm R} = 23$ and 25 mag and the signal-to-noise ratio is low, thus the signal-to-noise ratio for most of the galaxies is < 5 (see Tables A.3 and A.4).

Chapter 3

Observational results

3.1 Basic spectral properties of the medium-resolution sample

3.1.1 The redshift distribution

The majority of the 43 observed objects are galaxies. Only one object is classified as a quasar (QSO Q0103-260 or FDF-4683), and one as a star (FDF-0511). Since the low-resolution spectra have a much broader wavelength range and consequently more spectral features, the redshift for all objects with low-resolution spectra available was taken from Noll et al. (2004).

However eleven objects observed with medium-resolution spectra have no corresponding low-resolution spectra in the final FDF spectroscopic catalog (five objects in the 1400V setup and six objects in the 1200R setup). One object (FDF-0511) can be identified as a star, three galaxies (FDF-1267, FDF-8304 and FDF-9015) show a strong emission line and are identified as (likely) Lyα emitters. The other seven objects (FDF-672, FDF-1331, FDF-1383, FDF-1474, FDF-1502, FDF-4186 and FDF-7341) lack strong spectral features in the observed wavelength range and thus the objects could not be classified and their redshift could not determined.

In Table A.5 the 30 high-redshift galaxies are listed with the covered rest-frame wavelength range. The following analysis and discussion is restricted to the 18 galaxies, where the medium-resolution spectrum contains the Lyα line. In Table 3.1 the redshift and the apparent magnitude m_{R} are listed. These 18 galaxies are the so-called medium-resolution sample.

In Fig. 3.1 the distribution of redshifts of all objects observed in both medium-resolution grisms is displayed. Indicated in red are the galaxies of Table 3.1. The redshift ranges from $z = 2.77$ to $z = 4.995$. There is a strong peak at a redshift of $z \approx 3.3$. This strong peak in the redshift distribution of Fig. 3.1 is the combined effect of selection effects and a clustering of galaxies in the FDF at this redshift range. Galaxies selected for observing the Lyα line with the 1400V setup and selected for observing the UV-continuum with the 1200R setup have redshifts of $z \approx 3$. The distribution of the redshifts in the FDF low-resolution spectroscopic survey (Noll et al. 2004) showed several peaks, including a peak at the redshift of the QSO Q0103-260 at a redshift of $z = 3.375$.

Table 3.1: The so-called medium-resolution sample of galaxies. The medium-resolution spectrum of these 18 galaxies contains the Lyα emission line. The redshift z and the apparent magnitude $m_{\mathrm{R}}$of the galaxies are shown.

ID	z	m_{R}
1267	2.7876 ± 0.0005	27.08 ± 0.07
1337	3.4025 ± 0.0035	24.15 ± 0.01
2384	3.3143 ± 0.0043	24.60 ± 0.01
3389	4.5825 ± 0.0056	25.56 ± 0.02
4454	3.0854 ± 0.0041	26.10 ± 0.03
4691	3.3036 ± 0.0043	24.79 ± 0.01
5215	3.1480 ± 0.0041	24.53 ± 0.01
5550	3.3829 ± 0.0035	23.95 ± 0.01
5744	3.4011 ± 0.0031	24.81 ± 0.01
5812	4.9947 ± 0.0060	27.55 ± 0.11
5903	2.7743 ± 0.0030	23.13 ± 0.01
6063	3.3967 ± 0.0035	23.37 ± 0.01
6557	4.6822 ± 0.0057	25.94 ± 0.02
7539	3.2874 ± 0.0034	24.10 ± 0.01
7683	3.7812 ± 0.0038	24.92 ± 0.01
8304	4.2050 ± 0.0030	24.98 ± 0.01
9002	3.3747 ± 0.0044	
9015	3.9593 ± 0.0026	

3.1.2 UV continuum

UV flux and star-formation rate

The UV continuum of starburst galaxies is the result of the integrated light of thousands of O and B stars. O stars have a typical lifetime of 10 Myr, hence these stars are less than 10 Myrs old. Assuming a constant star-formation rate and using stellar synthesis models, the star-formation rate can be derived from the UV luminosity.

The UV spectral flux for the medium-resolution sample has been derived at a rest-frame wavelength of 1500 Å with a window of 40 Å (see Table A.6). For the flux derivation the low-resolution spectra have been used. In the absence of the low-resolution spectra, the medium-resolution spectra were taken. For FDF-5812, FDF-9015 and FDF-6557 the UV-spectral flux has been measured at λ = 1340 Å , 1355 Å , 1400 Å respectively, because the continuum was heavily affected by OH-bands at a rest-frame wavelength of 1500 Å. The error given is based on the photon statistics. Any systematic errors due to inaccurate absolute flux calibration are not included. The UV spectral flux has been converted into an absolute UV spectral luminosity assuming a flat, Λ-dominated universe ($\Omega_\Lambda = 0.7$, $\Omega_M = 0.3$ and $\mathrm{H}_0 = 70$ kms^{-1} Mpc^{-1}). A spherically symmetric emission characteristic is assumed. The UV luminosities range from $L_{\mathrm{UV}} = 1.3 \times 10^{34}$ WÅ^{-1} to 6×10^{34} WÅ^{-1}, with a mean value of $L_{\mathrm{UV}} = 2.1 \times 10^{34}$ WÅ^{-1}. $\mathrm{L}_\star$ is about 1.34×10^{34} WÅ^{-1} for galaxies at $z = 3$ (Inoue et al. 2005). Also the UV fluxes and spectral

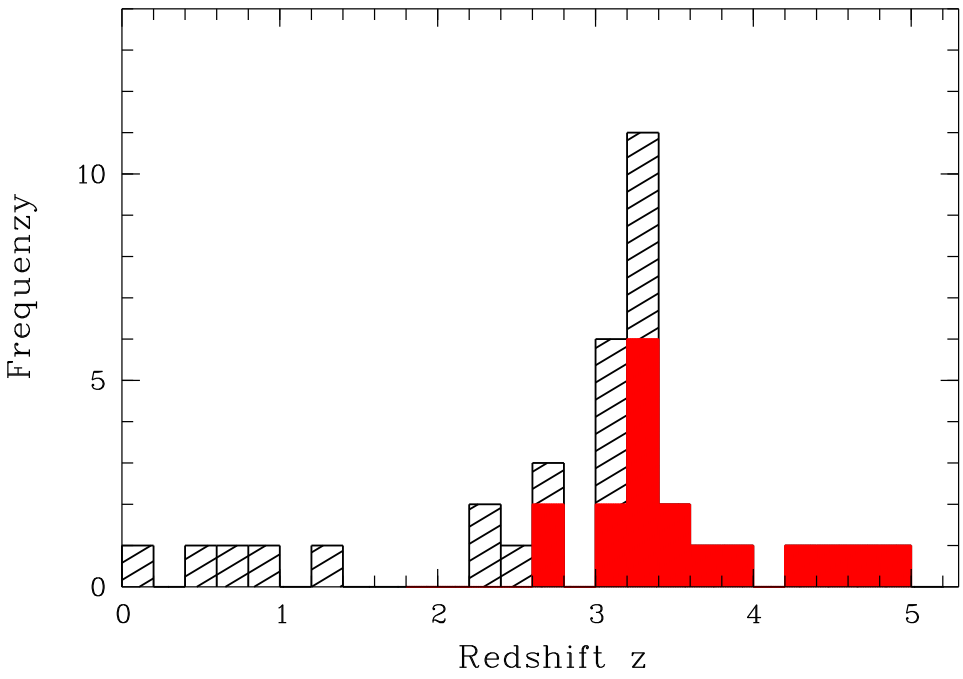

Figure 3.1: Distribution of the redshifts of all objects observed in both medium-resolution grisms (black hashed histogramm). Red indicated are the 18 galaxies of Table 3.1, which include the Lyα line in the wavelength range of the medium-resolutions spectra. The strong peak at $z \approx 3.3$ is the combined effect of selection effects and a clustering of galaxies in the FDF at this redshift range (see text).

luminosities of the 91 high-redshift galaxies of the FDF spectroscopic survey have been derived. The mean value is $L_{\rm UV} = 1.52 \times 10^{34}$ WÅ^{-1} , which is somewhat lower than the mean value of this sample. This is a selection effect, since brighter galaxies were selected for medium-resolution spectroscopy (see Sec. 2.2.1).

Using synthesis population models, Kennicutt (1998) give the following calibration[1]

$$SFR(\mathrm{M_\odot yr^{-1}}) = 1.046 \times 10^{-33} \mathrm{L_{UV}(W Å^{-1})} \qquad (3.1)$$

A Salpeter initial mass function in the mass range of 0.1 to 100 $\mathrm{M_\odot}$, solar metalicity, and 100 Myr old starburst with continuous star-formation, are assumed for this conversion. Application of different assumptions about the starburst changes the conversion factor. The star-formation rate for a 10 Myr old starburst is 46 % higher for the same luminosity and 7 % lower for a 300 Myr old starburst.

The star-formation rates range between 1.16 $\mathrm{M_\odot yr^{-1}}$and 60 $\mathrm{M_\odot yr^{-1}}$, with a mean of 22 $\mathrm{M_\odot yr^{-1}}$. This is in the range of other high-redshift galaxies, selected on the basis of the UV flux (Kennicutt 1998). This star-formation rates are without any correction for dust. The total star-formation rate of galaxies in the local universe ranges from zero in gas-poor elliptical galaxies to 20 $\mathrm{M_\odot yr^{-1}}$ in gas rich spiral

[1]Kennicutt (1998) give the calibration for $\mathrm{L_\nu}$ which was converted into $\mathrm{L_\lambda}$ for a wavelength of 1500 Å .

galaxies, while Ultra Luminous Infrared Galaxies (ULIRGs) show much stronger star-formation rates ($\approx$ 1000 $M_{\odot}yr^{-1}$) (Kennicutt 1998).

Slope of the UV continuum

The slope of the rest-frame UV-continuum depends on the metalicity, population (defined by Initial Mass Function (IMF) and the star-formation history), the age of the OB stars and the attenuation by dust. Studies by, e.g., Calzetti et al. (1994) and Heckman et al. (1998) showed that the UV-restframe continuum between 1216 Å and 3000 Å of starburst galaxies can be approximated by

$$F(\lambda) \approx \lambda^{\beta} \tag{3.2}$$

If hot stars dominate the galaxy spectrum, the continuum slope should has $\beta \approx -2.5$, varying only between β = -2.7 and -2.2 for a wide range of starburst parameters (Leitherer et al. 1999, Fig. 72b and Fig.74b), if a continuous star-formation is assumed. However, the observed continuum slope show a much broader range of values, from β = -2.7 to 2. Calzetti et al. (1994) gave evidence that attenuation of the UV continuum by dust is changing the continuum slope. In the following the term extinction is used to describe the absorption and scattering of light by dust of a point source, while attenuation describes the absorption and scattering of an extended light source. The attenuation is not only defined by the properties of the dust particles itself, but also by the spatial distribution of the dust relative to the stars. Since the intrinsic UV slope is a relatively robust quantity, the measured β can be used to derive the attenuation (Heckman et al. 1998). For starburst galaxies a gray attenuation law has been found (Calzetti et al. 2000).

The slope β of the galaxies in the FDF spectroscopic survey was measured and described in Noll et al. (2004). The slope of the UV-continuum was measured between 1200 Å and 1800 Å. The slope β could be measured up to a redshift of z = 4 . For more highly redshifted galaxies the OH-band prevents the determination of the continuum. The galaxies in the FDF have β between 1 and -3. The continuum slope β shows a dependence of the redshift, in the sense that galaxies are getting bluer for higher redshifts (Noll et al. 2004). The slope β derived for the galaxies of the medium-resolution sample are shown in Table A.6. They range from β = -0.55 to β = -2.46 with a mean value of β = -1.68.

3.2 Properties of the Lyα lines

3.2.1 Flux and star-formation rate

The Lyα flux $F_{\mathrm{Ly}\alpha}$ is measured for most galaxies in the low-resolution spectra, but some Lyα fluxes are measured in the medium-resolution spectra, because of absence of low-resolution spectra or the emission line were only detected in the medium-resolution spectrum. The distribution of the fluxes is shown in Fig. 3.2(a). While most of the galaxies of the FDF-spectroscopic survey have fluxes around zero (mean value = 8.66 $\times$ 10^{-21}Wm^{-2}), the medium-resolution sample, indicated in red in Fig. 3.2(a) has higher fluxes (mean value = 37.87 $\times$ 10^{-21}Wm^{-2}). This is caused by the target selection of galaxies with strong Lyα line. The flux of the

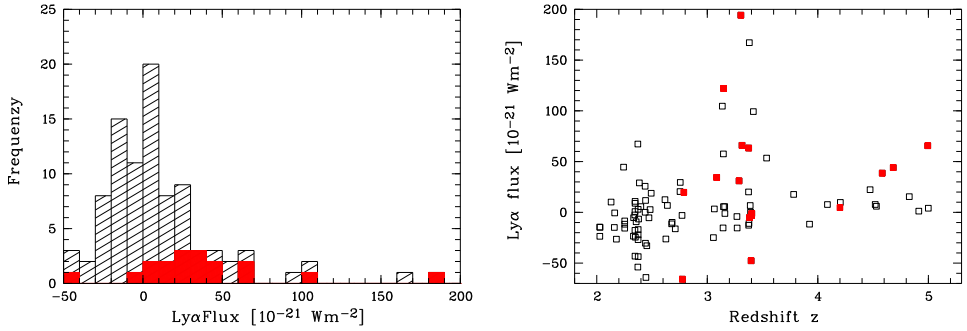

(a) **(b)**

Figure 3.2: (a) Histogram of the Lyα fluxes of the FDF spectroscopic sample (black hashing). In addition the histogram of the Lyα fluxes of the medium resolution sample have been included (red filled histogramm). (b) The Lyα fluxes of the FDF spectroscopic sample (black boxes) as a function of the redshift. Red boxes indicates the medium-resolution sample. The strong peak at $z \approx 3.2$ is the combined effect of selection effects and a clustering of galaxies in the FDF at this redshift range.

Lyα line of the medium-resolution sample (see Table A.7) and of all galaxies in the FDF spectroscopic sample with $z > 2.0$ is plotted in Fig. 3.2(b) as function of redshift. The medium-resolution sample is indicated in red. The Lyα fluxes range up to $200 \times 10^{-21}\mathrm{Wm}^{-2}$. The peak at a redshift of $z = 3.3$ arises from the large scale clustering in the FDF and of the target selection of the medium-resolution spectroscopy (see Sec. 3.1.1). While not all galaxies with a strong Lyα at a redshift of $z = 3$ are included in the medium-resolution sample, all galaxies with strong Lyα emission at a redshift of $z = 4.5$ to 5 are included.

Several surveys at high redshift have detected LAEs. The narrow-band imaging survey of Kudritzki et al. (2000) yielded nine LAEs with fluxes between 20 and 170 $\times\ 10^{-21}\mathrm{Wm}^{-2}$ at a redshift of $z = 3.1$. Assuming a flux limit of $20 \times 10^{-21}\mathrm{Wm}^{-2}$, 50 % of the medium-resolution sample in the lower redshift regime (z< 4) would have been observed in the survey of Kudritzki et al. (2000). The deep survey of Fynbo et al. (2003) detected 41 LAEs galaxies up to a flux limit of $8 \times 10^{-21}\mathrm{Wm}^{-2}$ in the redshift range from $z = 1.98$ to $z = 3.47$. 2/3 of the medium-resolution sample in the lower redshift regime ($z < 4$) would have been observed. The wide narrow-band survey of CADIS (Maier et al. 2003), searching for LAEs at the redshifts of $z = 4.8$, 5.7 and 6.7 has a flux limit of $F_{\mathrm{LIM}} = 30 \times 10^{-21}\mathrm{Wm}^{-2}$. 3 galaxies of the medium-resolution sample with $4 \leq z$ match this flux limit criterion.

¿From the flux of the Lyα line we computed the star-formation rates (SFR). The line luminosities are derived by assuming a standard cosmology model (see Sec. 3.1.2) and an isotropic emission. Synthetic models predict the rate of ionising photons $Q(H^0)$ of a stellar population. The ionising photons rate $Q(H^0)$ can be converted into Lyα photons assuming Case B recombination. In Case B recombination all ionising photons are absorbed in the HII-region and transformed into emission line photons. The medium is assumed to be optically thick for all Lyman continuum and Lyman line photons, thus each recombination generates a Lyα pho-

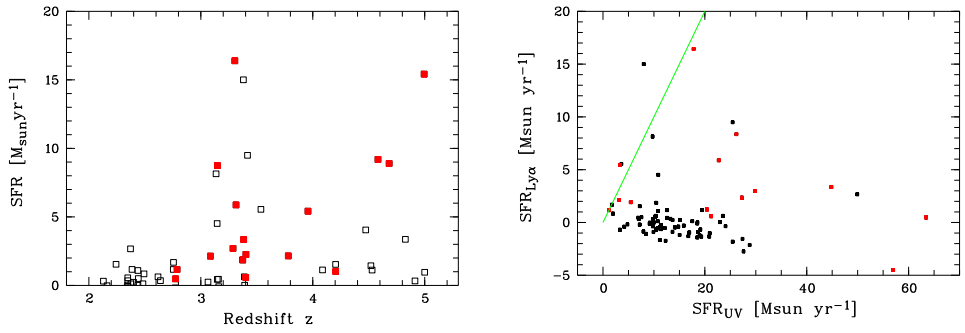

(a) **(b)**

Figure 3.3: (a) The star-formation rate $SFR_{\mathrm{Ly}\alpha}$ of the FDF spectroscopic sample (black squares) as a function of the redshift. Red squares indicate the medium-resolution sample. (b) The star-formation rate $SFR_{\mathrm{Ly}\alpha}$ as a function of the star-formation rate SFR_{UV} for the FDF spectroscopic sample (black dots). Red dots indicate the medium-resolution sample. The green line indicates where $SFR_{\mathrm{Ly}\alpha} = SFR_{\mathrm{UV}}$. For (b) only galaxies with $2 \leq z \leq 4$ have been plotted.

ton ($2^2\mathrm{P} \rightarrow 1^2\mathrm{S}$) or two-photon emission ($2^2\mathrm{S} \rightarrow 1^2\mathrm{S}$). The ratio of Ly$\alpha$ photon / two-photon emission is a low varying function of temperature and approximately 2/3 of all recombinations go through 2^2P and lead to Lyα emission (Osterbrock 1989).

To derive the star-formation rate the calibration of Kennicutt (1998) (See Sec. 3.1.2) is used:

$$SFR(M_{\odot}yr^{-1}) = 1.08 \times 10^{-53} Q(H^0)(s^{-1}) = 9.1 \times 10^{-36} L_{\mathrm{Ly}\alpha}(W) \qquad (3.3)$$

In Fig. 3.3(a) the distribution of $SFR_{\mathrm{Ly}\alpha}$ is shown (see Table A.7). The SFR ranges between 0 and 20 $\mathrm{M}_{\odot}\mathrm{yr}^{-1}$. The distribution is comparable to the distribution of the line fluxes. The Lyα emitters in the redshift range from $z = 4$ to 5 have star-formation rates comparable to the Lyα emitters in the redshift range from $z = 3$ to 4, while the observed line fluxes of the Lyα emitters in the redshift range from $z = 4$ to 5 were lower as the line fluxes of the Lyα emitters in the redshift range from $z = 3$ to 4 . This is simple because the higher redshift results in an higher distance modul.

The star-formation rate derived from the Lyα line is lower on average than the star-formation rate derived from the UV continuum (see Table 3.5 for $SFR_{\mathrm{Ly}\alpha}$/ SFR_{UV} or Fig. 3.3 (b)). For the medium-resolution sample a ratio of $SFR_{\mathrm{Ly}\alpha}$ / $SFR_{\mathrm{UV}} = 0.52$ is derived. The conversion of luminosities to star-formation rates are influenced by systematic uncertainties, but for most galaxies it can be concluded, that the Lyα emission is too low compared to that expected from the star-formation rate derived by the UV continuum. This behaviour has been observed in the local universe and the high-redshift universe. E.g., Ajiki et al. (2003) found a ratio of $SFR_{\mathrm{Ly}\alpha}$ / $SFR_{\mathrm{UV}} = 0.47$ for high-redshift LAEs.

3.2.2 Lyα equivalent width

The emission equivalent width EW is defined as

$$EW = \int_{\lambda_1}^{\lambda_2} \left(\frac{S(\lambda)}{C(\lambda)} - 1 \right) d\lambda, \tag{3.4}$$

where $S(\lambda)$ is the total flux at the wavelength λ and $C(\lambda)$ is the flux of the continuum. λ_1 and λ_2 give the lower and upper limit of the wavelength range of the line. For LAEs this is a important quantity, since LAEs are defined by a large Lyα equivalent width. The measurement of the equivalent width needs a good definition of the continuum. Due to the absorption by the IGM blue-ward of the Lyα line the measurement of the equivalent widths of Lyα is complex. Several methods were used, including the measurements using defined windows for line and continuum, applying an approximated continuum based on the UV-slope and a manual measurement. Note that all equivalent widths are quoted in the rest frame of the object. Besides the systematic errors, also the statistical error is large, since the continuum is in the nominator. LAEs with weak continuum have thus very uncertain equivalent widths.

In Fig. 2.1 the distribution of $EW_{\mathrm{Ly}\alpha}$ measured manually is shown. The black histogram shows 91 galaxies of the FDF spectroscopic survey, where the red histogram shows the 18 galaxies of the medium-resolution sample (see also Table A.7). The 91 galaxies of the FDF spectroscopic survey show that the Lyα line ranges from absorption ($EW_{\mathrm{Ly}\alpha}\approx$ -25 Å) to strong emission ($EW_{\mathrm{Ly}\alpha} \approx 270$ Å), while most galaxies have a $EW_{\mathrm{Ly}\alpha}$of ≈ 0 Å (see Fig. 2.1). The mean equivalent width is 15 Å. The 18 galaxies of the medium-resolution sample have a higher mean Lyα equivalent width ($EW_{\mathrm{Ly}\alpha} = 53$ Å). 10 of the 18 galaxies of the medium-resolution samples have a Lyα equivalent width of $EW_{\mathrm{Ly}\alpha} \geq 20$ Å.

The intrinsic $EW_{\mathrm{Ly}\alpha}$ can be derived with synthesis population models when it is assumed that the Lyα photons are produced by recombination in HII region ionised by young stars. Also stars have Lyα in absorption and emission, which has to be included when computed Lyα equivalent widths of galaxies (Charlot & Fall 1993). The role of shocks by supernovae is unsolved. Charlot & Fall (1993) finds a negligible contribution of supernova shells to the Lyα flux, while Bithell (1991) finds the opposite.

In dust-free galaxies, the more important parameters are the slope and the upper mass limit of the initial mass function (IMF), the metalicity and the star-formation history which determines the strength of the Lyα line. For a constant star-formation the most important parameter is the age of the starburst. The Lyα equivalent width is then decreasing with time. Malhotra & Rhoads (2002) find that the Lyα equivalent width is decreasing from 300 Å at 1 Myrs to 100 Å at 100 Myrs (for a Salpeter IMF and 1/20 solar metallicity). For very young ($\approx$ 2 Myr) and very low metalicity ($< 4 \times 10^{-4}$ $Z_{\odot}$), the Lyα equivalent width can reach up to 1500 Å (Schaerer 2003). Synthesis models show that star-forming galaxies, with moderate age (>10 Myr) and metalicity and IMF in the range of values observed in the local universe, have an $EW_{\mathrm{Ly}\alpha}$ in the range from 50 to 200 Å (Charlot & Fall 1993). The Lyα equivalent width can be interpreted as a comparison of $SFR_{\mathrm{Ly}\alpha}$ with SFR_{UV}, since $EW_{\mathrm{Ly}\alpha}$and $SFR_{\mathrm{Ly}\alpha}/\ SFR_{\mathrm{UV}}$ both give the ratio of Lyα flux

to UV-continuum flux. Most of the galaxies in the FDF have much weaker Lyα emissions compared to the continuum as expected. It has been proposed that dust decreases the $EW_{\mathrm{Ly}\alpha}$ (Charlot & Fall 1993). Since an dust screen in front of the galaxy would affect both Lyα and UV-continuum, the $EW_{\mathrm{Ly}\alpha}$ would not change. A different mechanism is needed to explain the relatively stronger attenuation of the Lyα photons compared to the UV photons. One possible explanation is the resonance scatterings of Lyα photons in neutral hydrogen, enriched with dust. The Lyα photons are resonance scattered and hence have a larger optical path. More Lyα photons are absorbed by dust than UV-continuum photons (Charlot & Fall 1993). The observed lower ratio of $SFR_{\mathrm{Ly}\alpha}$ / SFR_{UV} can be explained also by this mechanism. Chen & Neufeld (1994) explained the broad and strong absorption at the wavelength of Lyα seen in many high-redshift galaxies by this mechanism. If the column density is sufficiently high, not only the Lyα emission, but also the underlying stellar continuum is affected and a broad absorption is seen.

The target selection of the FDF spectroscopic survey based on photometric redshifts, which is more sophisticated as the selection of galaxies by the Lyman-Break technique. While LBG galaxies and the galaxies in the FDF spectroscopic survey are selected by conceptually similar but different techniques, the galaxies do not strongly differ. Noll et al. (2004) showed that galaxies of the FDF spectroscopic catalog and galaxies of the sample of Shapley et al. (2003) have similar average spectra, if galaxies in the same redshift range are compared. For comparison the $EW_{\mathrm{Ly}\alpha}$ distribution derived by Shapley et al. (2003) has also been included in Fig. 3.4. With respect to the Lyα equivalent width both the FDF spectroscopic survey and the sample of Shapley et al. (2003) essentially observe the same high-redshift galaxy population.

There exits the possibility that the above described samples of UV-selected galaxies consist of two different galaxy populations or galaxies in different evolutionary stages. One population show a strong Lyα emission line, one population show a weaker Lyα emission line. To test the plausibility of this hypothesis, the Lyα equivalent width distribution of Shapley et al. (2003) and Noll et al. (2004) were modelled with two Gaussian components. In Table 3.2 the fit parameters are given. The difference between the two distribution may arise due to cosmic variance and the different redshift range.

Table 3.2: Parameters of the Gaussian components, which fit the Lyα equivalent distribution of Noll et al. (2004) and Shapley et al. (2003). Center gives the central position, σ is the standard deviation and flux the relative fluxes of the two components.

Parameter	Noll et al. (2004)	Shapley et al. (2003)
Center(1) [Å]	0	-7
σ(1) [Å]	17	11
Flux(1)	87 %	64 %
Center(2) [Å]	60	20
σ(2) [Å]	102	85
Flux(2)	13 %	36 %

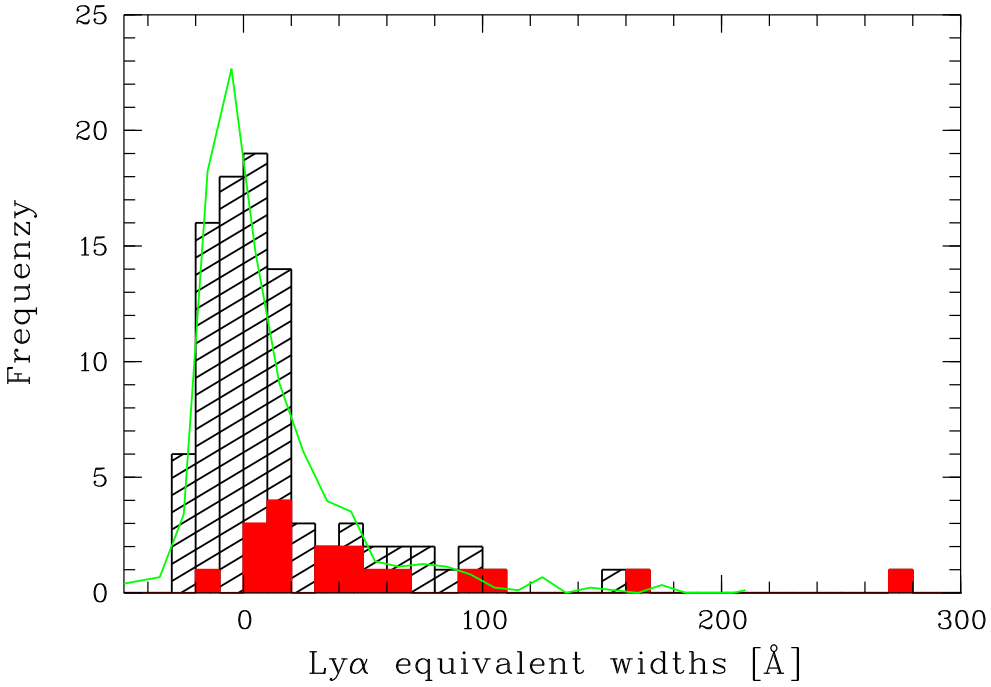

Figure 3.4: Distribution of the Lyα equivalent width of the FDF spectroscopic sample (hashed black histogram). The red histogram show the 18 galaxies of the medium-resolution sample. The green line is the distribution of Lyα equivalent widths of the sample described in Shapley et al. (2003).

3.2.3 The observed Lyα line profiles

In Fig. 3.5 four example profiles of the medium-resolution sample are presented. All spectra are converted to the rest-frame system. The Lyα profile show a large variety of properties, from absorption (see FDF-5903, Fig. 3.5 a), to absorption with emission, to strong emission. Complex profiles are observed in some cases (see FDF-5215, Fig. 3.5 d).

Distribution of the line widths

The Full Width Half Maximum (FWHM) of the Lyα emission have been measured for all lines, which shows an emission component (16 galaxies). The FWHM was converted into velocity widths after subtracting quadratically the effective instrumental profile. The distribution is shown in Fig. 3.6(a). It ranges from 200 kms^{-1} up to 1500 kms^{-1}. Most lines have line widths below $FWHM \approx 600$ kms^{-1}, but FDF-4691, FDF-9015, and FDF-7539 have higher line widths. Note that FDF-4691 and FDF-7539 have a double peak profile and here line widths are given for the complete profile. Rhoads et al. (2003), Dawson et al. (2004) and Venemans et al. (2004) analysed LAEs at a redshift of $z > 5$ and found line widths of $FWHM < 500$ kms^{-1}.

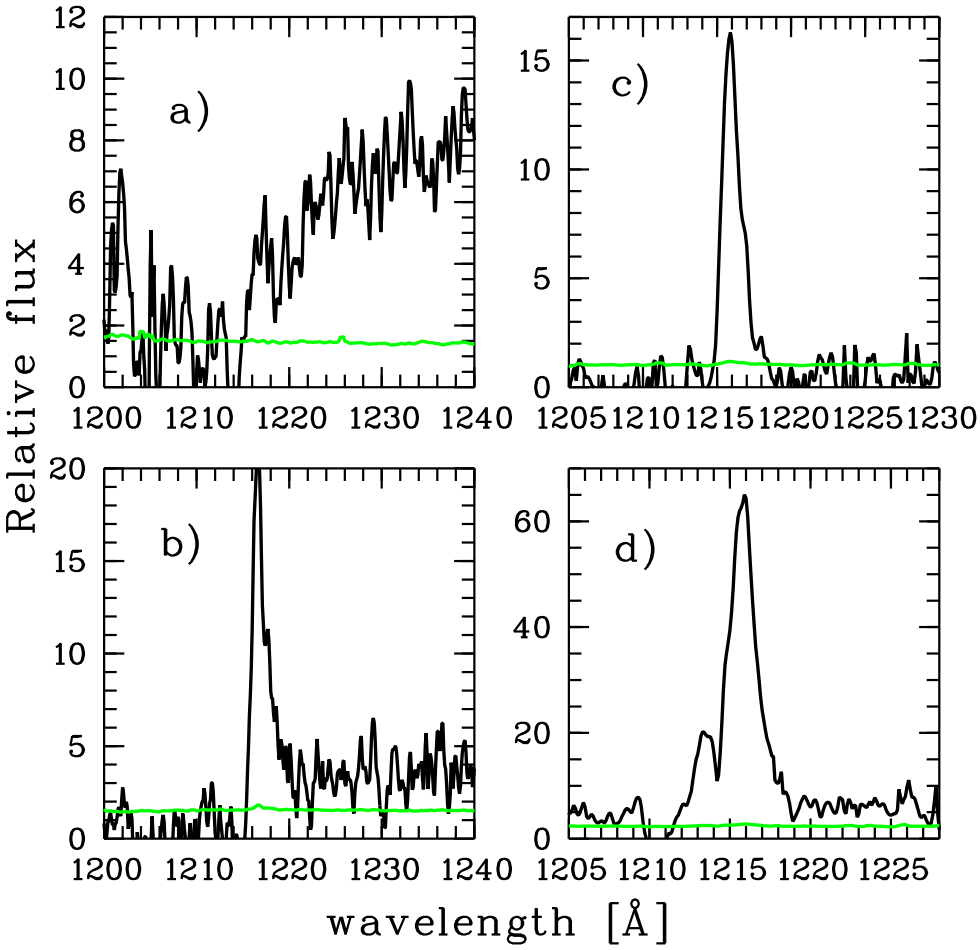

Figure 3.5: Four examples of Lyα profiles in the FDF. a) FDF-5903, b) FDF-5550, c) FDF-4454, d) FDF-5215. The green line indicates the noise level.

Distribution of asymmetry

Emission lines of candidates of high-redshift LAEs are often observed with a low signal-to-noise ratio and relatively low-resolution. The asymmetry of the emission line is an important tool to identify the line as Lyα. In order to quantify the asymmetry of the Lyα line Rhoads et al. (2003) introduced the parameters $a_{\rm flux}$ and $a_{\rm wave}$. $a_{\rm wave}$ gives the wavelength ratio and $a_{\rm flux}$ the flux ratio of the blue and red part of the Lyα profile.

$$a_{\rm flux} = \frac{\int_{\lambda_{10,\rm b}}^{\lambda_{\rm peak}} f(\lambda) d\lambda}{\int_{\lambda_{\rm peak}}^{\lambda_{10,\rm r}} f(\lambda) d\lambda} \tag{3.5}$$

and

$$a_{\rm wave} = \frac{(\lambda_{10,\rm r} - \lambda_{\rm peak})}{(\lambda_{\rm peak} - \lambda_{10,\rm b})} \tag{3.6}$$

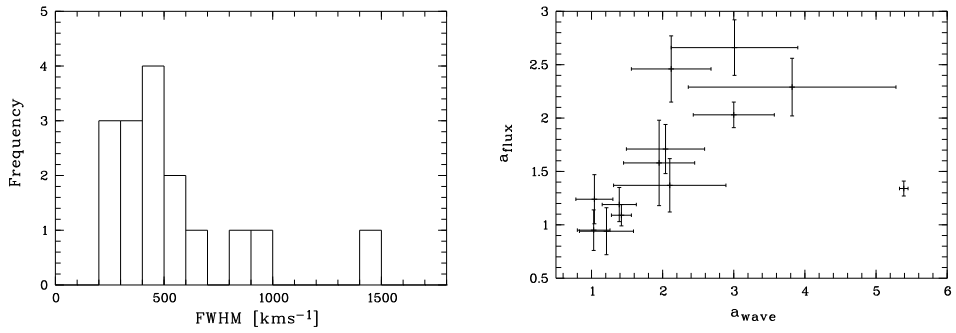

(a) **(b)**

Figure 3.6: (a) Distribution of the line widths ($FWHM$) of the Lyα emission line of the medium-resolution sample. (b) The asymmetry parameter $a_{\rm flux}$ as a function of the asymmetry parameter $a_{\rm wave}$.

$\lambda_{\rm peak}$ is defined as the wavelength of the peak of the emission. $\lambda_{10,\rm b}$ is the wavelength where the flux reaches 10 % of his peak flux level on the blue side and $\lambda_{10,\rm r}$ on the red side respectively.

In Table A.8 the values of $a_{\rm flux}$ and $a_{\rm wave}$ including error are listed. In Fig. 3.6 $a_{\rm flux}$ is plotted as a function of $a_{\rm wave}$. Most of the profiles have $a_{\rm wave}$ and $a_{\rm flux}$ > 1 and thus are extended to the red, which is in good agreement with results from Dawson et al. (2004). They analysed mainly galaxies with $z > 4$. Moreover Dawson et al. (2004) found for 28 galaxies at $z \approx 1$ asymmetry parameters of the [OII] $\lambda\lambda$3726.2, 3728.9 line of $a_{\rm wave}$ and $a_{\rm flux} \approx 1$.

The drawback of these parameters is the uncertainty in determining $\lambda_{\rm peak}$ and $\lambda_{10,\rm b}$, which are highly affected by noise. Dawson et al. (2004) raised and lowered the threshold but found no benefit of using other values than 10%. Lowering the threshold increases the contamination from continuum noise, while raising diminishes the contribution of the red wing.

3.3 Analyses of the rest-frame UV spectral features

3.3.1 UV-spectral features

Equivalent widths and line fluxes

The line fluxes and equivalent widths of absorption and emission lines in addition to the Lyα line have been measured in the low- and medium-resolution spectra of the medium-resolution sample. The measurements were mostly consistent in the spectra, but the measurements in the medium-resolution spectra were preferred, because of the higher accuracy. In Table A.9 the equivalent widths of the interstellar absorption lines SiII λ 1261, OI/SiII λ 1303 and CIIλ 1335 are given. OI/SiII λ 1303 is a blend of the lines OI λ 1302.17, SiII λ 1304.4 and could be resolved in some galaxies of the medium-resolution sample. Following Shapley et al. (2003) the average absorption equivalent width $EW_{\rm LIS}$ of the strongest low-ionisation inter-

Table 3.3: Velocity offset between the Lyα line and the prominent low-ionisation interstellar absorption lines. The widths of the interstellar absorption lines are also included.

ID	δv [kms^{-1}]	$FWHM_{\rm LIS}$ [kms^{-1}]	$EW_{\rm LIS}$[Å]
1337	-607 ± 45	350 ± 35	-1.78 ± 0.21
5550	-620 ± 85	540 ± 40	-2.54 ± 0.31
5744	-560 ± 120	460 ± 100	-2.6 ± 0.64
5903	-760 ± 80	770 ± 50	-3.08 ± 0.12
6063		645 ± 75	-2.64 ± 0.38
7539	-80 ± 30	380 ± 100	-1.23 ± 0.14
8304	-860 ± 140	550 ± 140	-2.05 ± 0.22

stellar absorption lines (see Table 3.3) is derived. Since only the three prominent interstellar absorption lines of Table A.9 have been frequently derived, the average equivalent width $EW_{\rm LIS}$ is derived from these three lines only. In Table A.10 the equivalent widths of the interstellar absorption lines SiII λ1526, FeII λ1608, AlII λ1671 and AlIII $\lambda\lambda$1856,1863 are given. Table A.11 lists the equivalent widths of the stellar wind lines SiIV $\lambda\lambda$1394,1403 and CIV $\lambda\lambda$1548, 1551. Table A.12 gives the equivalent widths of Lyβ and the photospheric line SV* λ1501.76. The equivalent widths and fluxes of HeII λ1640 and of CIII] λ1909 are listed in Table A.13.

The Tables A.9 to A.13 show that most lines are detected with a low signal-to-noise ratio only. The low signal-to-noise ratio is the reason for constructed and analysing composite spectra of high-redshift galaxies, as shown by Shapley et al. (2003) and Noll et al. (2004). No strong high-ionisation emission lines were detected in the low-resolution or the medium-resolution spectra. Only weak HeII λ1640 and CIII] λ1909 are seen in some spectra. HeII λ1640 can be explained by WR stars. CIII] λ1909 is seen in nearby starburst galaxies in emission (Heckman et al. 1998). There is trend for stronger CIII] λ1909 in nearby starburst galaxies with decreasing metalicity, which is explained by a decrease of the electron temperature in higher metalicity gas (Heckman et al. 1998). The absence of high-ionisation emission lines indicates that strong AGN activity it rather unlikely. The properties of the absorption lines can only be measured for galaxies showing a sufficient spectral UV flux. Thus the equivalent widths of absorption lines is measured only in galaxies with a low Lyα equivalent. The measured equivalent widths of the interstellar absorption lines and the stellar wind lines are in the range of the galaxies presented by Shapley et al. (2003). Based on at the line ratios of interstellar absorption lines Shapley et al. (2003) concluded that the most prominent interstellar absorption lines are saturated.

Kinematics of the interstellar absorption lines

The centers and line widths of the interstellar absorption lines could be measured for seven galaxies of the medium-resolution sample. Using the redshift of the Lyα emission component as a reference, the velocity offsets between the Lyα emission and the interstellar absorption lines were derived. Six galaxies show a velocity offset between the Lyα emission line and the interstellar absorption lines. This can be explained by either a Lyα emission redshifted with respect to the system redshift

or blue-shifted interstellar absorption lines, or both. This kind of velocity offset has been observed in many high-redshift galaxies (Franx et al. 1997; Shapley et al. 2003). Adelberger et al. (2003) analysed 14 near-infrared spectra of high-redshift galaxies and found that the Lyα is redshifted with a mean of $v_{\rm delta}$ = 310 kms^{-1} with respect to optical nebular emission lines (e.g. [OIII] $\lambda\lambda$4959, 5007). The low-ionisation interstellar absorption of the 14 high-redshift galaxies are blue-shifted with a mean of $v_{\rm delta}$ = -150 kms^{-1}.

The broad interstellar absorption lines have often been detected in UV-restframe spectra of Lyman-break galaxies (e.g., Steidel et al. 1996). Shapley et al. (2003) found for their sample of about 800 spectra of high-redshift galaxies an average velocity dispersion for the low-ionisation interstellar absorption lines of $FWHM_{\rm LIS}$ = 560 $\pm$ 150 kms^{-1}. An explanation for this large widths of the interstellar absorption lines are interstellar shocks and supernova winds rather than gravitational virial dynamics (Shapley 2003).

3.3.2 Modelling the UV-spectra with STARBURST99

We modelled the medium-resolution sample with the synthetic medium-resolution spectra of STARBURST99 (Leitherer et al. 1999) and assuming a Calzetti attenuation law (Calzetti et al. 2000). The slope of the continuum and the strength and shape of the stellar wind lines allows to derive parameters of the starburst. As discussed in Sec. 3.1.2 the slope of the UV-continuum is mostly determined by the attenuation, while the age and the metalicity of the starburst have only little influence on the slope. The age and the metalicity of the starburst is derived by modelling the stellar wind lines, namely NV $\lambda\lambda$1239,1243 and CIV $\lambda\lambda$1548, 1551, with STARBURST99. While Mehlert et al. (2002) argued that CIV $\lambda\lambda$1548, 1551 is a good metalicity indicator because it is present in O stars of all luminosity classes, SiIV $\lambda\lambda$1394, 1403 is less useful to derive the metalicity, because its strength increases from dwarfs to supergiant stars (Walborn & Panek 1984a) and SiIV has a maximum in early B stars. Hence SiIV $\lambda\lambda$1394, 1403 is not only dependent on metalicity, but also on the population composition. Since the stellar wind feature only becomes apparent in supergiant stars, in the composite spectra of galaxies the SiIV $\lambda\lambda$1394, 1403 is dominated by interstellar absorption lines (Shapley 2003). Moreover the medium-resolution spectra of FDF-5903 show that SiIV $\lambda\lambda$1394, 1403 is dominated by interstellar absorption lines (see Sec. 3.4).

Leitherer et al. (1999, 2001) developed STARBURST99, a procedure, allowing to calculate a wide range of properties of star-forming galaxies, including synthetic medium-resolution (R$\approx$ 1500) rest-frame UV spectra. Since only stars in the Milky Way and stars in the Small and Large Magellanic Cloud (SMC, LMC) can be observed with sufficient resolution, STARBURST99 provides only two metalicities for synthetic medium-resolution spectra, namely solar or SMC/LMC metalicity. The number of observed stars was too small to generate a set of synthetic spectra for SMC and LMC metalicity each. Two star formation histories are provided: continuous and instantaneous. Other parameters like the initial mass function or the stellar mass ranges can be altered less stringent. The initial mass function yields the distribution of the masses of the recently new-formed stars and is approximated by a power-law ($\Phi(m) = \frac{dN}{dM} = cm^{-\alpha}$), while α is the free parameter and c a

Table 3.4: Parameters of the STARBURST99 models. A Calzetti attenuation law was assumed. All six galaxies were modelled with SMC/LMC metallicity. Except for FDF-4691 a Salpter-IMF was used. For FDF-4691 a a shallower IMF was used. ($\alpha = 1.5$)

ID	$E(B-V)$ [mag]	age [Myrs]
4691	0.1	10
5215	0.15	60
5550	0.25	300
5903	0.25	100
6063	0.25	100
7539	0.2	100

constant. In the local universe the slope is for sites of massive star-formation is $\alpha = 2.35$ (Salpeter IMF) (Larsen et al. 2004). The lower and upper limits of the IMF determines the stellar masses to be considered. Usually 1 $M_\odot$ and 100 $M_\odot$ are chosen as limits. While the lower mass limit is not crucial for starburst galaxies, the upper mass limit is important, since the most massive stars are the most luminous and observed in distant galaxies. Also they show strong stellar wind lines.

The attenuation was modelled by assuming $F_{\rm att} = F_{\rm intr} \times 10^{E(B-V)\times A(\lambda)}$, where $F_{\rm intr}$ is the intrinsic spectrum given by STARBURST99, $E(B-V)$ parameterise in this modell the amount of attenuation and $A(\lambda)$ is the attenuation law. $F_{\rm att}$ is the attenuated STARBURST99 spectrum. Initially derived for local starburst galaxies (Calzetti et al. 2000) the Calzetti law is commonly used for high-redshift galaxies (Giavalisco 2002). But there are indications that the Calzetti is only appropriate for blue starburst galaxies (Noll et al. 2005).

The full set of the STARBURST99 parameters could not be investigated, since in many cases the medium-resolution spectra only covered a part of the UV-restframe spectra. The low-resolution spectra have the disadvantage of not resolving the stellar wind profiles. Also interstellar lines cannot be distinguished from stellar wind lines. Hence the free parameters were restricted to the metalicity, age, and the amount of attenuation in most cases. All spectra have been modelled with SMC/LMC metalicity, which in agreement with the results of Mehlert et al. (2002), who estimated the metalicity of high-redshift galaxies in FDF using the CIV $\lambda\lambda$1548, 1551 equivalent width. In Fig. 3.7 a comparison with observed and synthetic spectra is presented. As it can be seen in Table 3.4 most galaxies are modelled with a starburst age of ≈ 100 Myrs and a attenuation of $E(B-V) = 0.2$ mag. This corresponds to $A_{\rm UV} = 2$ mag. Thus the dust corrected UV-continuum fluxes and hence the dust-corrected star-formation rates are factor 6 higher as the uncorrected.

3.4 Remarks on individual objects

18 galaxies observed with the medium-resolution setup show the Lyα line in one of the medium-resolution spectra. In Table 3.5 we summarise some properties of the medium-resolution sample. In addition the half-light radii of the galaxies are also included, which have been derived from HST/ACS images (see Fig. 3.8). The

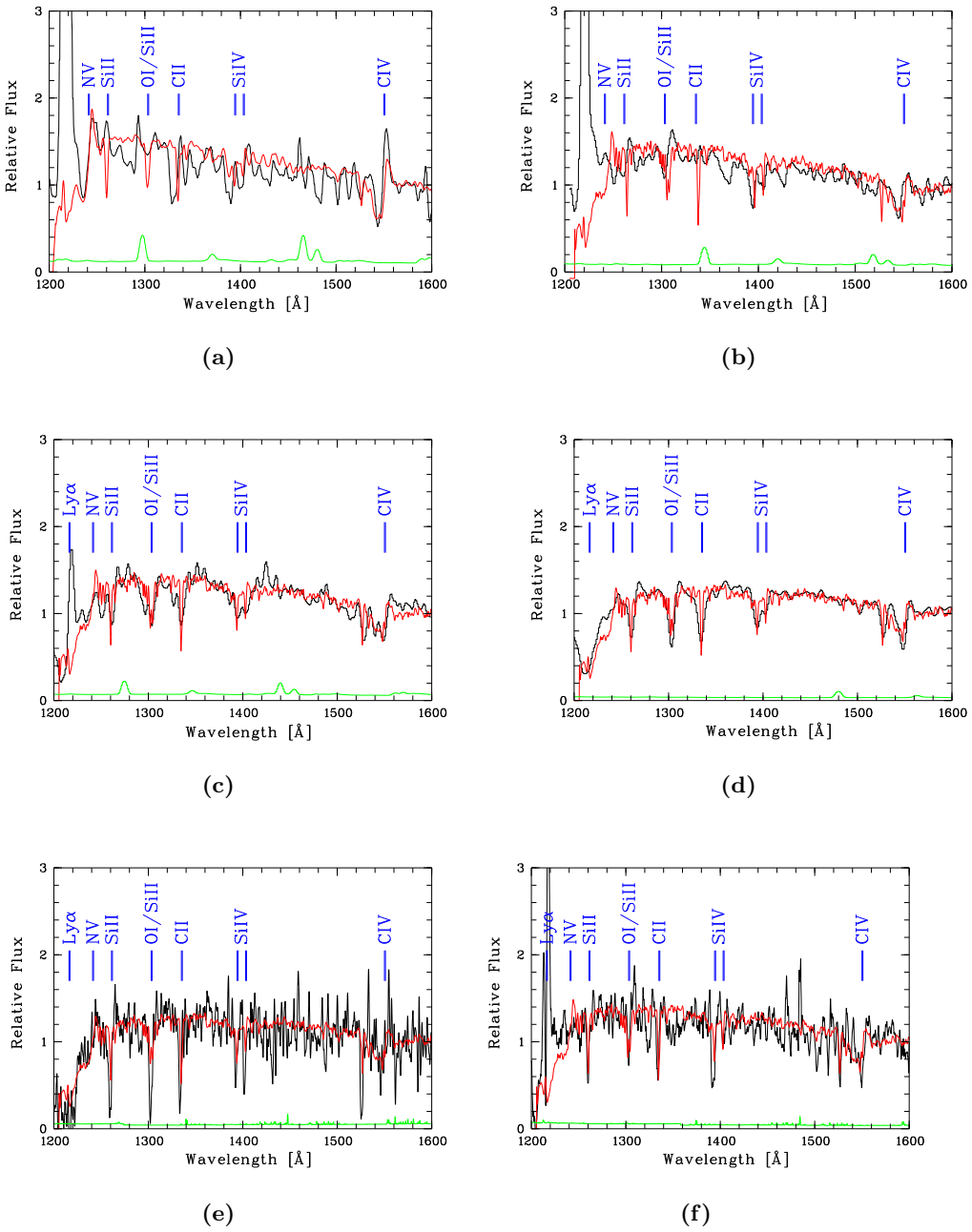

Figure 3.7: Comparsion of observed spectra with STARBURST99. The model parameters are given in Table 3.4. a)FDF-4691, b) FDF-5215, c)FDF-5550 ,d) FDF-5903, e) FDF-6063, f) FDF-7539

Table 3.5: Some properties of the medium-resolution sample of galaxies.

ID	z	β	$\mathrm{EW}_{\mathrm{Ly}\alpha}$ [Å]	$SFR_{\mathrm{Ly}\alpha}/\ SFR_{\mathrm{UV}}$	radius [kpc]
1267	2.788		95	1.003	
1337	3.403	-2.43	11	0.086	0.82
2384	3.314	-0.55	41.17	0.259	
3389	4.583		51	0.621	0.621
4454	3.085	-2.42	70	0.676	
4691	3.304	-2.46	103	0.924	< 0.2
5215	3.148	-1.71	36	0.318	0.73
5550	3.383	-1.81	11	0.075	0.825
5744	3.401	-1.02	13.31	0.027	1.875
5812	4.995		270	2.970	< 0.15
5903	2.774	-1.15	3.05	0.008	1.58
6063	3.967	-2.02	-19		1.58
6557	4.682		38	0.499	
7539	3.287	-1.74	13	0.997	0.61
7683	3.7812	-1.16	13.18	0.060	0.90
8304	4.205		7.2	0.044	0.77
9002	3.374		57	0.352	
9015	3.957		162	1.631	

half-light radii are converted from apparent into physical radii using the cosmology of Sec. 3.1.2. The average radius is 0.9 kpc, which is much smaller than the Milky Way (diameter = 10 kpc). The HST/ACS image observe the rest-frame UV of the starburst galaxies, which is dominated by young stars and not by the entire stellar population. Moreover the surface brightness scales with $(z+1)^{-4}$, thus the extended regions of the galaxies are not easily detected.

FDF-1267

FDF-1267 is a serendipitous detection in the 1400V setup, which has not been observed by the FDF spectroscopic survey. The spectrum only shows a emission line at $\lambda = 4604.7$ Å. The continuum is barely detected($\approx 3.5\ \sigma$) in the spectrum (see Fig. 3.9). The continuum is very weak ($m_{\mathrm{R}} = 27.08 \pm 0.07$ mag) and hence no photometric redshift is available. The [OII] doublet $\lambda\lambda$3726.2, 3728.9 can be ruled out to produce the observed emission since the doublet would be resolved at our resolution. The emission line is not [OIII] λ 5007, because [OIII] λ 4959 is not detected. Since the line is asymmetric, it is likely that the galaxy is a LAE at a redshift of z = 2.786. Also the small line width of the Lyα and the non-detection of the NV $\lambda\lambda$1238.82, 1242.80 emission line makes an Type II AGN[2] unlikely (Stern et al. 2002). The good agreement between SFR_{UV} and $SFR_{\mathrm{Ly}\alpha}$ shows that the Lyα is not strongly affected by dust.

[2]Active Galactic Nucleus

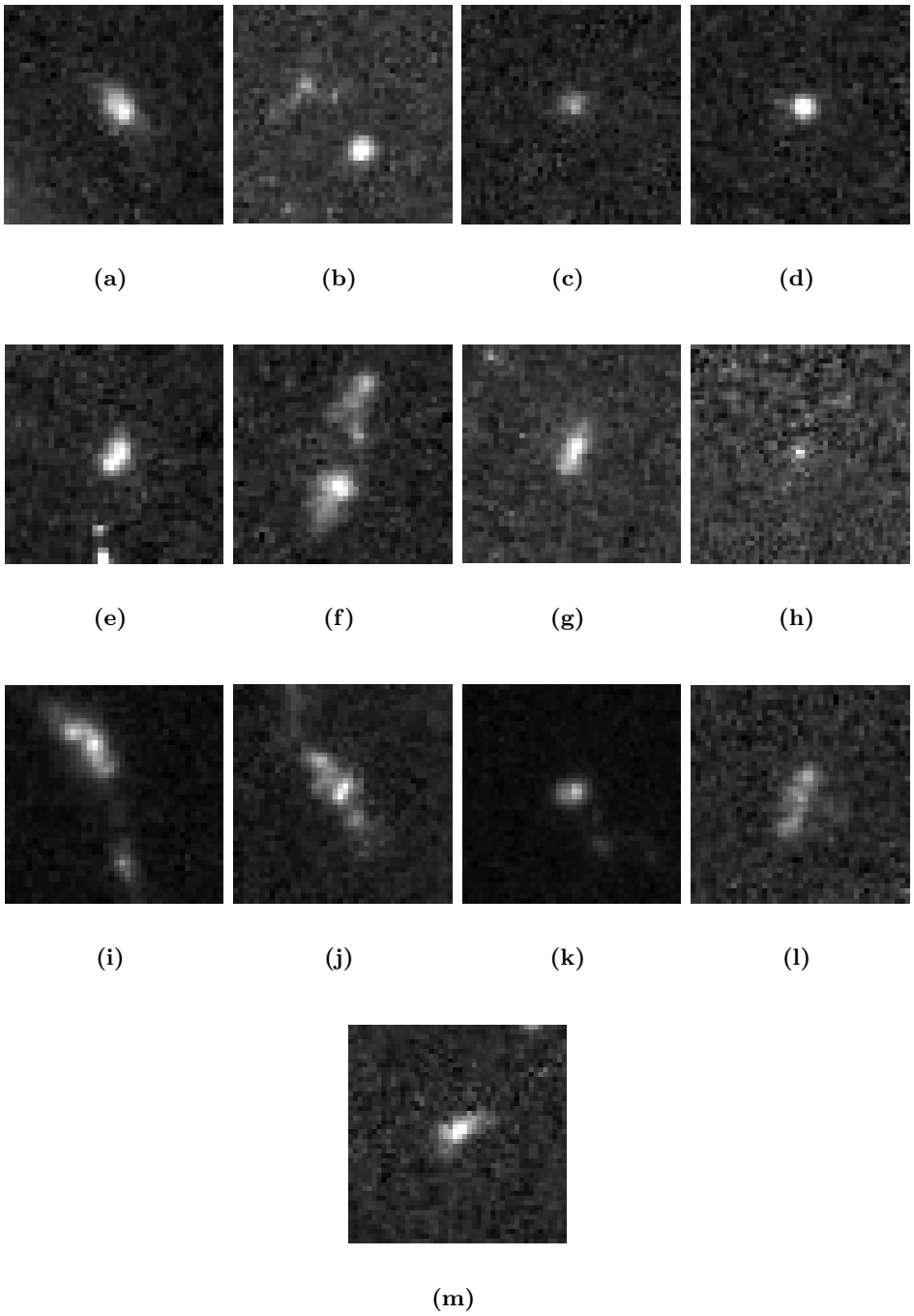

Figure 3.8: HST/ACS images of the sample of medium-resolution galaxies. Each image is 15 × 15 kpc large, north is up, east is left. (a) FDF-1337, (b) FDF-2384, (c) FDF-3389, (d) FDF-4691, (e) FDF-5215, (f) FDF-5550, (g) FDF-5744, (h) FDF-5812, (i) FDF-5903, (j) FDF-6063, (k) FDF-7539, (l) FDF-7683, (m) FDF-8304

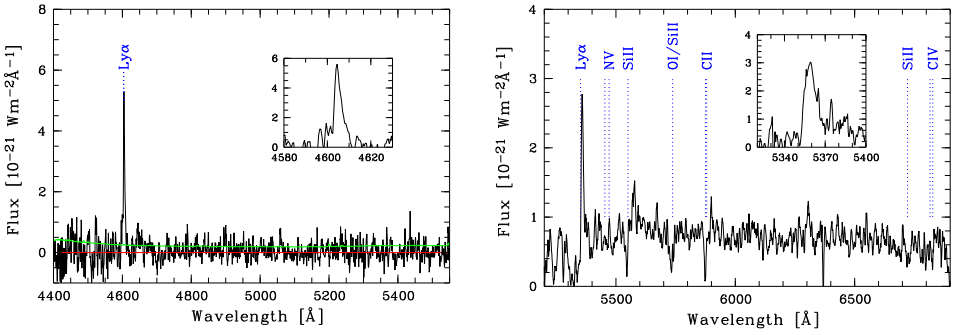

(a) **(b)**

Figure 3.9: a) FDF-1267 spectrum obtained with the 1400V setup FDF-1267. The red line indicates zero flux and the green line the noise function. b) Composite medium-resolution spectrum of FDF-1337. The spectrum have been smoothed by a box-car filter.

FDF-1337

The galaxy FDF-1337 ($m_{\rm R}$ = 24.15 mag) has a redshift of z = 3.4025 and has been observed with all grisms (150I, 1200R, 1400V). While the spectrum observed with the 1400V grism covers just the Lyα line, the spectrum observed with the 1200R grism covers the rest-frame UV from 1234 to 1570 Å. In Fig. 3.9 a composite spectrum of both medium-resolution spectra is shown. The composite spectrum has been smoothed. The $SFR_{\rm Ly\alpha}$ / $SFR_{\rm UV}$ ratio of 0.08 is low, the Lyα is heavily affected by absorption of dust or absorption of the interstellar medium. The Lyα flux and equivalent width is measured in the medium-resolution spectra, since the increase of resolution allows a better derivation of these quantities. Unfortunately a bright galaxy in the neighbourhood, FDF-1371 ($\rm m_R$ = 21.36 mag), prevents a good sky subtraction, resulting in uncertain spectra.

FDF-2384

FDF-2384 ($m_{\rm R}$ = 24.61 mag) was identified in the FDF spectroscopic survey as a starburst galaxy at z = 3.3143 on the basis of the strong emission and the continuum break at the emission line. The low-resolution spectrum show a rather featureless, red continuum (see Fig. 3.10) with a strong Lyα emission line. FDF-2384 consists of two objects in the HST/ACS image. FDF-2384(B) is not resolved in the HST/ACS images, while FDF-2384(A) is extended. The two objects are separated by approximatly 0.6 arcseconds.

Interestingly, the inspection of the two-dimensional spectrum obtained with the 1400V grism shows that the red continuum and the Lyα line are spatially separated by approximately 0.6 arc-second. The two components can be identified as two objects in the photometric data, the component showing the strong Lyα, FDF-2384(A), has a fainter flux in the broad-bands and bluer colours while the continuum component FDF-2384(B) is brighter and redder. In the FDF-catalog the two objects are designed to FDF-2384. The spectrum obtained with the 1200R

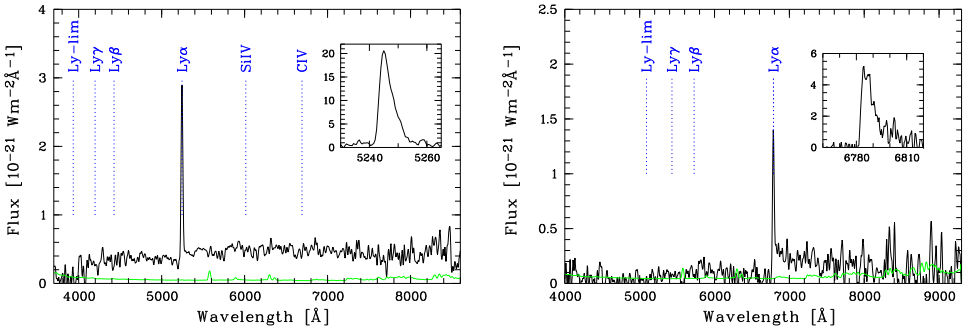

Figure 3.10: (a) Low-resolution spectrum of FDF-2384. The inset shows the medium-resolution spectrum centered at the Lyα line. (b) Low-resolution spectrum of FDF-3389. The inset shows the medium-resolution spectrum centered at the wavelength of theLyα line

grism is targeted on the brighter component FDF-2384(B). The continuum of the low-resolution spectrum or the spectrum obtained with the 1200R grism does not allow the redshift determination of FDF-2384(B). While the emission line can be identified as Lyα emission and thus FDF-2384(A) is at redshift of $z = 3.3143$, the object FDF-2384(B) may not belong to FDF-2384(A) and be a foreground object.

FDF-3389

This high-redshift ($z = 4.5821$) galaxy FDF-3384 has one of the highest continuum fluxes for galaxies in this redshift regime in the FDF and hence a significant continuum step at the wavelength of the Lyα emission line (see Fig. 3.10). The strong Lyα line shows a typical asymmetric profile. The continuum slope could not be derived since the UV continuum is redshifted into the OH bands. The Lyα emission line is measured in the 1200R grism.

FDF-4454

This z = 3.0854 galaxy shows a strong Lyα line (see Fig. 3.11). The UV continuum is too weak to detect further lines. The Lyα line shows a typical asymmetric emission profile.

FDF-4691

This $z = 3.304$ galaxy has been analysed in Tapken et al. (2004). Apart from the strong Lyα line the low-resolution spectrum (Fig. 3.12) shows a for this redshift normal starburst spectrum. The medium-resolution spectrum covers only the rest-frame wavelength range of 1088 to 1393 Å, which includes the Lyα and the CII λ1355 line. The Lyα line shows a double peak profile. The galaxy is not resolved on the HST/ACS image, which place an upper limit on the radius of $r = 0.2$ kpc.

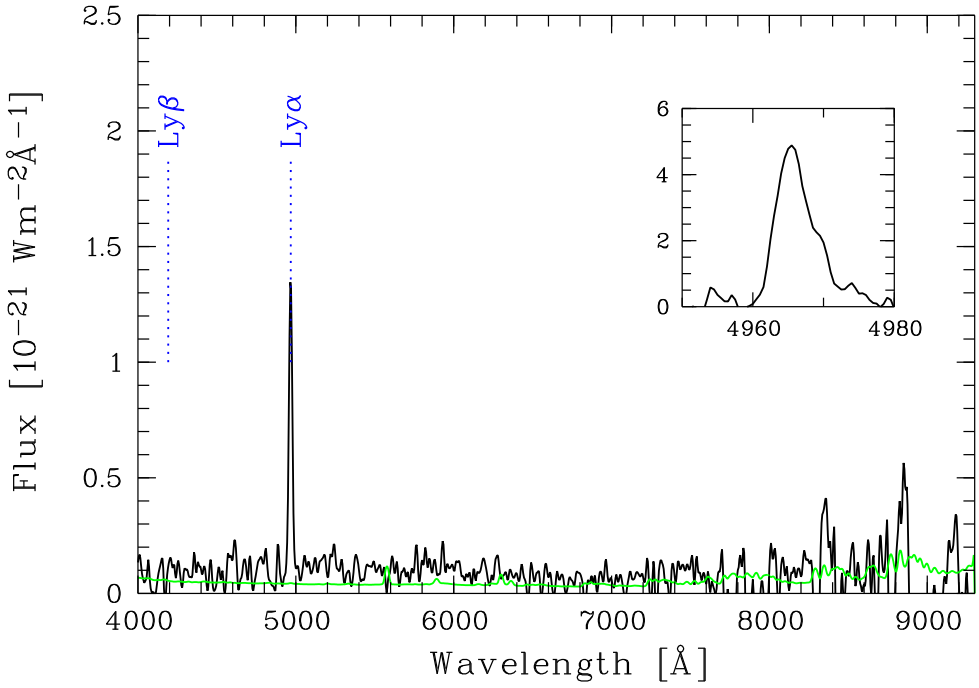

Figure 3.11: Low-resolution spectrum of FDF-4454. The inset shows the medium-resolution spectrum centered at the wavelength of the Lyα line.

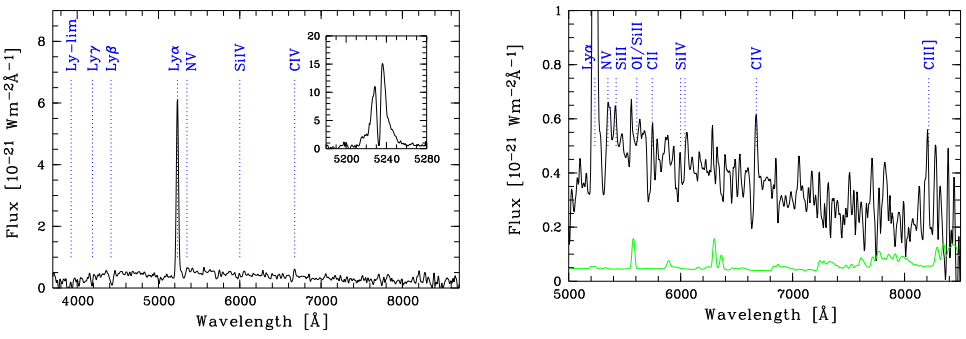

(a) **(b)**

Figure 3.12: (a) Low-resolution spectrum of FDF-4691, (b) Scaled version of 3.12. The green line indicates the noise level.

The continuum break at the wavelength of Lyα is caused by absorption of the Lyα forest. Also Lyβ and Lyγ are detected. As shown by Fig. 3.12 at least three prominent stellar wind lines are detected: NV $\lambda\lambda$1239, 1243 and CIV $\lambda\lambda$1548, 1551 show P-Cygni profiles and SiV $\lambda\lambda$1394, 1403 is mainly in absorption. HeII λ1640 and CIII] λ1909 appear in emission.

AGN or starburst The Lyα profile ($FWZI$[3] $\approx$ 2000 kms^{-1}) differs from the other Lyα profiles observed in this survey and from other high-redshift galaxies observed by, e.g., Dawson et al. (2002). The typical Lyα profile show narrow, asymmetric profiles with $FWHM \approx 300$ kms^{-1} with a sharp blue cut-off and a red wing. On the other hand, van Ojik et al. (van Ojik et al. 1997) found for high-redshift radio galaxies symmetric Lyα profiles with line widths of the order of $\approx$ 1500 km s^{-1}. As some of these profiles have the same line widths and similar profiles as FDF-4691, one might suspect that the Lyα line of FDF-4691 is excited by an AGN. Furthermore the galaxy is not resolved on the HST/ACS images, placing an upper limit of $r = 0.2$ kpc on the radius of the object. Typical LBG galaxies have half-light radius of $r = 1.5$ kpc (Venemans et al. 2005).

Appenzeller et al. (2005) analysed a high-resolution spectrum of SDSS J1553+0056, which was previously classified as a possible LBG galaxy (Bentz et al. 2004). The UV-restframe spectrum of SDSS J1553+0056 shows a strong Lyα line, no other emission lines and several prominent absorption features. Appenzeller et al. (2005) found no indication for starburst activity in the high-resolution spectra and concluded that SDSS J1553+0056 is indeed an AGN mimicking a starburst galaxy in the UV-restframe spectra. SDSS J1553+0056 is belonging to the class of broad absorption line (BAL) QSOs, probably belonging to the rare FeLoBALQSO class. While the spectrum SDSS J1553+0056 closely resemble those of starburst galaxies, Appenzeller et al. (2005) found several features in the spectra of SDSS J1553+0056 which are not seen in the UV-restframe spectra of starburst galaxies. This feature includes a broad CII λ1335 absorption line, a deep absorption trough at NV $\lambda\lambda$1239, 1243 and the continuum features caused by excited Fe II levels in the rest-frame 1550-1800 Å range. While FDF-4691 shows no deep absorption trough at NV $\lambda\lambda$1239, 1243 and no features in rest-frame 1550-1800 Å range, FDF-4691 also shows a broad CIIλ 1335 absorption line. There exists the possibility that FDF-4691 could be also a rare broad absorption line QSO.

However, the hard radiation field of an AGN would be expected to result in higher NV / Lyα, CIV / Lyα and CIII] λ1909 / Lyα line ratios than observed. For example, the observed CIV / Lyα = 0.025 is ten times smaller than the ratio in the composite spectra of AGNs (CIV / Lyα = 0.25, Osterbrock 1989). However, Hall et al. (2004) presented one object SDSS J113658.36+024220.1, showing only one strong, moderately broad (FWHM = 1430 kms^{-1}) Lyα line and no detectable metal-line emission. The unusual continuum slope and the variability show that this object is an QSO. But these objects are uncommon, Hall et al. (2004) analysed the SDSS Data Release 1 Quasar Catalog (Schneider et al. 2003), which consists of 2400 objects with Lyα in the wavelength range of the grisms. Hall et al. (2004) find only one object showing a strong Lyα line without metal-line emission.

[3]Full Width Zero Intensity

Radio observations of the FDF have shown that at 1.4 GHz no radio source > 100 μJy is present at the position of FDF-4691 (Wagner 2003, private communication). However, since the radio data is not deep, this criterion is not very constraining. Assuming a UV/Radio ratio of the radio-quiet QSO Q0103-260 (FDF-4683, z=3.36), which is detected in the radio survey, FDF-4691 would have a radio flux of 16 μJy, well below the detection limit.

Starburst99: In the following discussion we assume that the Lyα emission of FDF-4691 is excited by the continuum radiation of the hot stars in this galaxy.

In order to constrain the starburst age and metalicity of FDF-4691 we compared the low-resolution spectrum with STARBURST99 models assuming a Calzetti et al. (2000) reddening curve. The best fit for the UV slope and the profiles of the stellar wind lines was found for continuous star-formation, low starburst age (< 20 Myr), SMC/LMC metalicity, a non-Salpeter IMF of $\alpha = 1.5$ and $E(B-V) = 0.1$ mag (see Fig. 3.7). But other combinations also provide good fits, including models with an instantaneous starburst and a very young age ($\simeq$ 5 Myr)

The metalicity derived from the CIV absorption equivalent width ($|EW| = 3.0 \pm$ 0.9 Å) using the calibration given in Mehlert et al. (2002) is also in agreement with the SMC/LMC value. This metalicity is normal for this redshift (Mehlert et al. 2002). The reddening of $E(B-V) = 0.1$ mag is among the lowest observed in this redshift range in the FDF spectroscopic survey. Note that this value depends on the reddening curve used. The steeper extinction law of the SMC (Bouchet et al. 1985) would yield $E(B-V) = 0.03$ mag. The low reddening is not unexpected in view of the anti-correlation between the strength of the Lyα line and the reddening as derived from the UV continuum slope β found by Shapley et al. (2003).

The CIV $\lambda\lambda$1548, 1551 emission component is stronger in FDF-4691 than in this model. This may indicate the presence of early O stars or Wolf-Rayet stars, which are known to show such CIV profiles (Wu et al. 1983; Walborn & Panek 1984b; Willis & Garmany 1989). Wolf-Rayet stars are massive stars in late phase of their evolution, where a significant fraction of their outer envelope have been blown away by their massive stellar winds. WC stars show strong carbon emission lines and are a subclass of the Wolf-Rayet stars. The fact that the low-ionisation interstellar lines (SiII λ1260, OI/SiII λ1303, CII λ1335), visible in the STARBURST99 model, are not present in FDF-4691, is again consistent with the correlation found by Shapley et al. (2003) between the reddening and the strength of the interstellar absorption lines. The presence of the strong CII λ1335 line (blue-shifted by 1400 kms^{-1} in respect to the Lyα line) may be explained by the presence of WC stars in FDF-4691, which tend to show strong blue-shifted CII λ1335 lines (Willis & Garmany 1989). Meynet & Maeder (2005) computed the ratios of O stars to WC stars in starbursts. They computed a typical ratio of WC/O $\approx$ 0.02 for a continuous starburst and low metalicity (Z = 0.004). Since O stars do not show a strong CIIλ1335 line feature, the detection of the CIIλ1335 line can only be explained by an over-enhancement of WC stars. WC stars may also provide an explanation for the strength of the HeII and CIII] emission. The presence of very young stars and WR stars together with the large equivalent width of Lyα indicate that the starburst is very young (< 5 Myr).

We conclude that the spectrum of FDF-4691 can be explained by a young starburst spectrum. An AGN activity cannot be ruled out (see discussion above). Thus the nature of this object is not well constrained. In the following analysis of the sample of the medium-resolution sample, we assume that FDF-4691 is a starburst galaxy.

FDF-5215

FDF-5215 is a z = 3.1480 galaxy with a moderate Lyα emission. This starburst galaxy is observed in all grisms with good signal-to-noise ratio. The Lyα profile shows a strong emission line, with a blue-shifted second emission line (see Fig. 3.13).

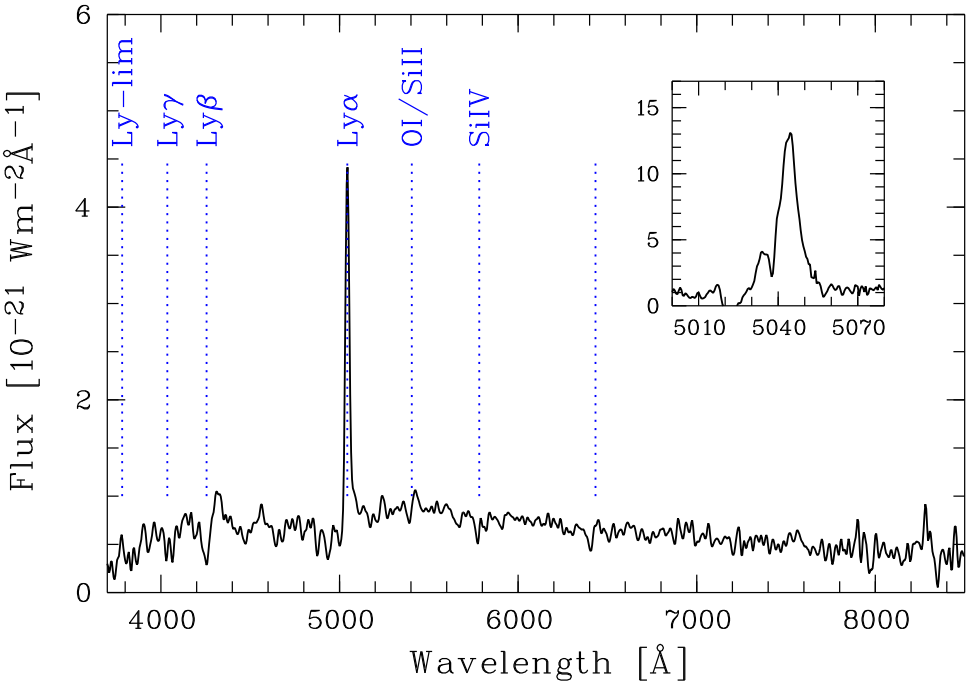

Figure 3.13: Low-resolution spectra of FDF-5215, prominent lines are indicated.

In the low-resolution spectrum (see Fig. 3.13) the interstellar absorption line OI/SiII λ 1303 could be detected. It has a P-Cygni profile, but in the medium-resolution spectrum no interstellar absorption line is detected. In the low-resolution spectrum the stellar wind lines SiIV $\lambda\lambda$1394, 1403 and CIV $\lambda\lambda$1548, 1551 are detected. The SiIV $\lambda\lambda$1394,1403 line falls not within the wavelength range of any of the medium-resolution grism. The spectrum obtained with the 1200R setup shows the CIV $\lambda\lambda$1548, 1551 feature. Moreover the nebular emission CIII] λ 1909 is detected in the low-resolution spectrum.

The low-resolution spectrum of FDF-5215 can be fitted with an older starburst ($\approx$ 60 Myr), SMC/LMC metalicity, and moderate extinction ($E(B-V) = 0.15$ mag) (see Fig. 3.7). The range of possible parameters is large, especially the age is is not well constrained.

FDF-5550

FDF-5550 is a bright ($m_{\rm R}$ = 23.95 mag) z = 3.3818 galaxy with a weak Lyα line (see Fig. 3.14). The inset in Fig. 3.14 (a) shows the asymmetric Lyα profile. The object is observed in both setups and the composite medium-resolution spectrum ranges in the UV-restframe from 1053 Å to 1656 Å. Inspections of the HST/ACS reveals that FDF-5550 consists of two galaxies, separated with a projected distance of 0.825 arc-seconds. The less luminous galaxy FDF-5550(A) is located north-west of FDF-5550(B), which is mainly observed by the medium-resolution spectroscopy. Both galaxies FDF-5550(A) and FDF-5550(B) have the same colours, indicating that the redshift is almost the same.

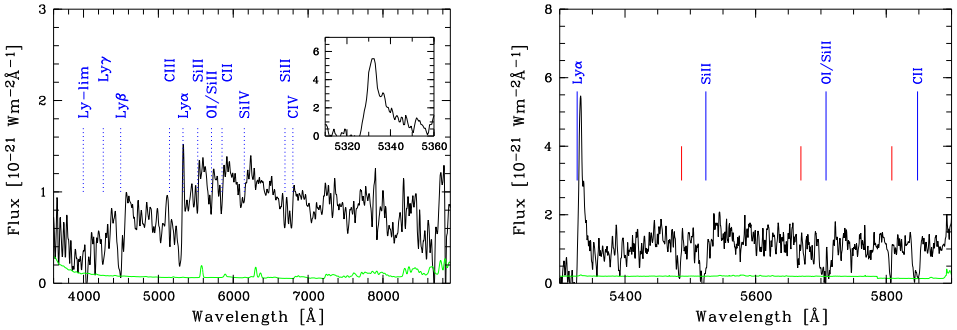

Figure 3.14: (a) Low-resolution spectrum of FDF-5550. (b) Medium-resolution spectrum (1400V) of FDF-5550. The interstellar absorption lines and Lyα are indicated in blue. Indicated in red is the absorption line system at the redshift of $z \approx 3.351$.

In the medium-resolution spectra an intervening absorption line system is detected, the following lines are detected at a redshift of $z \approx 3.351$: SiII λ 1261, OI/SiII $\lambda\lambda$1302, 1304 , CII $\lambda\lambda$1334.5,1335.7, SiIV $\lambda\lambda$1394, 1403, SiII λ1527, and CIV $\lambda\lambda$1548, 1551. The intervening absorption line system has a velocity offset of about 2200 kms^{-1} to the systematic redshift of the galaxy. Given the great velocity offset, it is unlikely that the system is physically connected to the galaxy. In the high-resolution spectrum of the QSO Q0103-260 (Frank et al. 2003) no corresponding absorption line system is seen. The projected distance between the QSO Q0103-260 and FDF-5550 is 43“, which corresponds to 323 kpc at this redshift. Since the absorption line system is not observed in the QSO spectrum, a contribution of the IGM is not likely. A possible explanation is that the line of sight intersects a foreground galaxy with a slightly lower redshift. It is likely that the interstellar lines detected at a redshift of $z \approx 3.351$ are produced by FDF-5550(B). FDF-5550(B) appears extended on the HST/ACS images (diameter = 3.064 kpc), but the distance to FDF-5550(A) is 6.12 kpc. Either FDF-5550(B) is more extended as indicated by the HST/ACS images or the interstellar absorption lines originate from a galaxy scale wind, which drives material into the intergalactic medium.

The medium-resolution spectrum of FDF-5550 allows to derive the redshift of

prominent low-ionisation interstellar absorption lines (see Fig. 3.14). All three lines are saturated, hence the equivalent width can not be used to derive the column density of the lines. The photospheric line SV λ 1501.76 is detected at a redshift of z = 3.3835. Since Lyα has a redshift of z = 3.388, the velocity offset between Lyα and the interstellar absorption lines is $\delta v \approx 600$ kms^{-1}, while the interstellar absorption lines at line center are about ≈ 360 kms^{-1} blue-shifted to the stellar component of the galaxy. The SiIV $\lambda\lambda$1394, 1402 doublet could be resolved in the medium-resolution spectra. The small line width and the redshift is showing that these lines are probably interstellar lines.

The low-resolution spectrum of FDF-5550 can be fitted with an older starburst modell ($\approx$ 300 Myr), SMC/LMC metalicity and moderate extinction (E(B-V)=0.15 mag) (see Fig. 3.7). As FDF-5215, the range of possible parameters is large, especially the age is is not well constrained.

FDF-5744

FDF-5744 has a redshift of $z = 3.4011$ and a magnitude of $m_{\rm R}$= 24.8. The Lyα line is in absorption in the low-resolution spectrum (see Fig. 3.15). Several absorption lines are seen in the low-resolution grism. While Lyα is seen only in absorption in the low-resolution grism, the better resolution of the medium-resolution spectrum (see Fig. 3.15) allows to detect a weak Lyα line ($F_{\rm Ly\alpha} = 6.2 \pm 0.89 \times 10^{-21}$Wm^{-2} and $EW_{\rm Ly\alpha}$= 13.31 $\pm$ 5.92 Å). But the low signal-to-noise ratio ($SNR = 3$ per resolution element in the spectral region of the Lyα) does not allow the derivation of useful parameters of the Lyα profile.

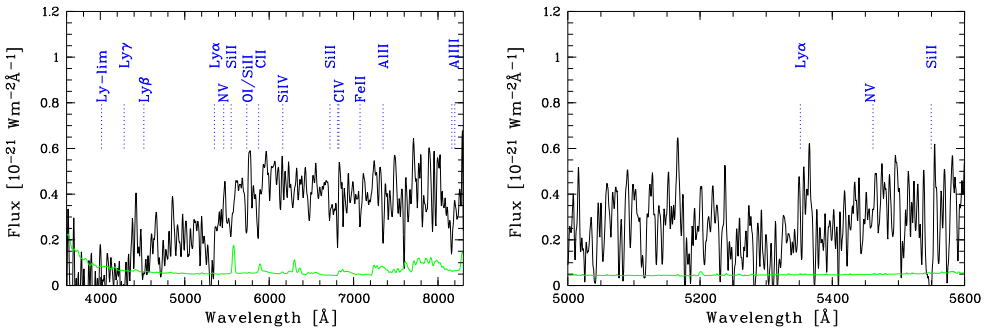

(a) **(b)**

Figure 3.15: (a) Low-resolution spectrum of FDF-5744. (b) Medium-resolution spectrum of FDF-5744.

FDF-5812

This galaxy has the highest spectroscopic redshift in the FDF, $z = 4.994$. The Lyα line is the only visible feature, the continuum is only detected weakly (0.04 $\pm$ 0.01 10^{-21}Wm^{-2} Å^{-1}) in the spectra (see Fig. 3.16). The galaxy has the highest equivalent width ($EW_{\rm Ly\alpha}$= 270^{+91}_{-51} Å) in the FDF. While the high equivalent

width is uncertain, since the error of the weak continuum measurement determines the error of the Lyα equivalent widths, the Lyα equivalent width is higher as expected from synthesis population models. Moreover since neutral hydrogen of the intergalactic medium will likely absorb a part of the Lyα flux, the $EW_{\mathrm{Ly}\alpha}$ is likely higher. They are no high-ionisation state emission lines and the Lyα line width is small ($FWHM = 283$ kms^{-1}). Also the Lyα profile show a typical asymmetric profile.

Lyα emission galaxies found with narrow-band searches show sometimes a strong Lyα equivalent width (Malhotra & Rhoads 2002). E.g., Dawson et al. (2004) found four galaxies with $EW_{\mathrm{Ly}\alpha} > 240$ Å . An AGN activity is not likely, because these sources are not detected in X-rays (also the stacked images are not detected in X-rays (Wang et al. 2004)). In addition no accompanying high-ionisation state emission lines, which indicate AGN activity, are detected in these galaxies with large Lyα equivalent width (Dawson et al. 2004). Malhotra & Rhoads (2002) suggest that these galaxies are in the very early stages of evolution of a galaxies. These galaxies might have zero metalicity and a top heavy initial mass function. Dawson et al. (2004) analysed the spectra of high-redshift Lyα emission galaxies, which shows large Lyα equivalent widths. They found no indication for primordial stars, the so called PopIII stars. But not all surveys for Lyα emission galaxies report large equivalent widths. Hu et al. (2004) analysed 19 spectra of $z = 5.7$ galaxies. The large majority of their sample have equivalent widths below 240 Å and thus could be explained by young starburst galaxies with a Salpeter IMF. In addition Hu et al. (2004) stressed the point that the equivalent width is very sensitive to the continuum-band exposures. Indeed the 4 galaxies of their sample with $EW_{\mathrm{Ly}\alpha} > 240$ Å could be well below $EW_{\mathrm{Ly}\alpha} > 240$ Å , given the large error. Ajiki et al. (2004) derived the equivalent width of four galaxies and found that all have $EW_{\mathrm{Ly}\alpha} < 200$ Å.

FDF-5903

FDF-5903 is the brightest ($m_{\mathrm{R}} = 23.02$ mag) galaxy in this sample. The $z = 2.77430$ galaxy show Lyα mainly in absorption, while a possible emission is detected in the medium-resolution spectrum (See Fig. 3.17).

The medium-resolution spectrum ranges from 1180 to 1523 Å and besides the lines mentioned above several weak emission lines are detected. SiII* λ1264.74 ($F = 7.2 \pm 1.34 \times 10^{-21}$ W m^{-2} and $EW = 0.61 \pm 0.15$ Å) and SiII* λ1309.28 ($F = 9.35 \pm 1.32 \times 10^{-21}$ W m^{-2} and $EW = 0.85 \pm 0.16$ Å) are also detected. The doublet SiIV $\lambda\lambda$ 1393.76, 1402.77 can be resolved. The two components have the same redshift has the interstellar lines and are probably of interstellar origin. Several stellar photospheric lines are intimated, but none is detected significantly.

The emission of these excited lines was detected in composite spectra by Shapley et al. (2003). The excitation energy for the excited states are roughly 0.04 eV. The Einstein A coefficients of the SiII* transitions range from 10^8-10^9 s^{-1}. Only in very dense environments the line is dominated by collisional excitation or de-excitation Shapley (2003). Shapley et al. (2003) found no explanation for the lines, discussing a origin in photoionised HII regions or a origin in large scale outflows.

The low-resolution spectrum of FDF-5903 is in agreement with the synthetic

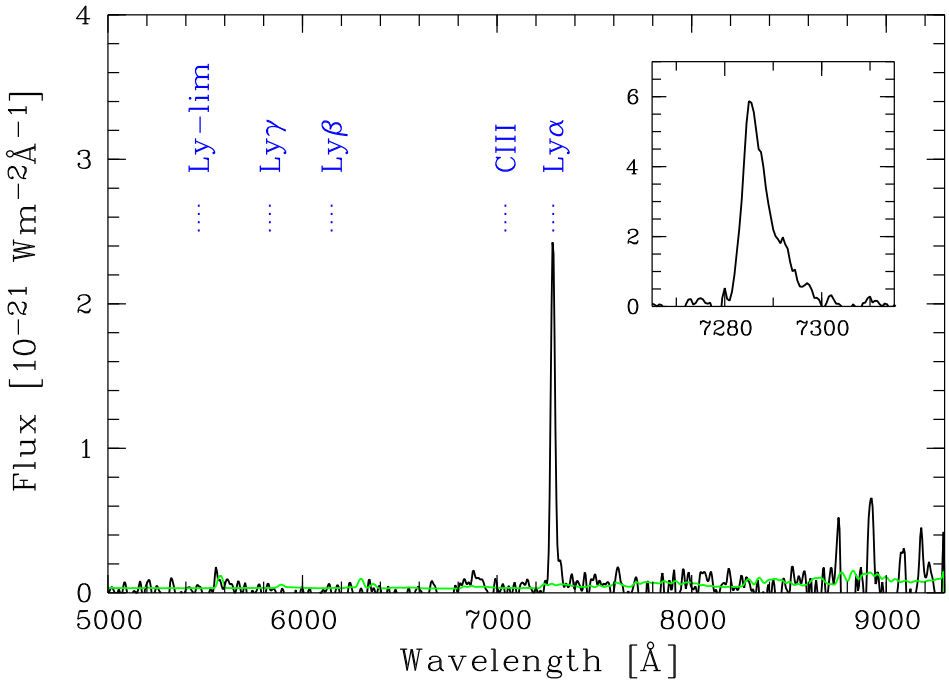

Figure 3.16: Low-resolution spectrum of FDF-5812, the inset shows the medium-resolution spectrum centered at the Lyα line.

spectra of STARBURST99 using a Salpeter intial mass function. The absorption component of the CIV profile can be fitted with SMC/LMC metalicity. The weak P-Cygni profile NV $\lambda\lambda$1238.82, 1242.80 is best fitted with an old starburst. As before the parameters could not well defined with the low-resolution spectrum. In Fig. 3.7 the low-resolution spectrum is compared with STARBURST99 spectrum (age = 300 Myr, E(B-V) = 0.25 mag, α = 2.35)

The medium-resolution spectrum only covers the rest-frame wavelength range from 1180 to 1523 Å, hence CIV $\lambda\lambda$1548, 1551 is not included. The emission component of the P-Cygni NV $\lambda\lambda$1238.82, 1242.80 allows an age determination (assuming a SMC/LMC metalicity, an IMF of α = 2.35 and an E(B-V) = 0.25 mag) of age = 100 $\pm$ 20 Myr.

FDF-5903 is well detected in the infrared bands. The flux in the J and Ks filter is in agreement with a SMC/LMC metalicity, an IMF index of α = 2.35 and an E(B-V) = 0.20 mag and an age of 100 Myr. The degeneracy of the parameters is still present. The fluxes are also fitted with higher attenuation and a younger age (E(B-V) = 0.25 mag and an age of 20 Myr). But an underlying old stellar population is not likely.

FDF-6063

FDF-6063 is a bright ($m_{\rm R}$= 23.37 mag) galaxy with a redshift of $z = 3.3969$. The medium-resolution spectra cover the restframe-wavelength range of 1086 to 1609 Å. The Lyα line is seen in absorption (see Fig. 3.18). The galaxy is lensed by the

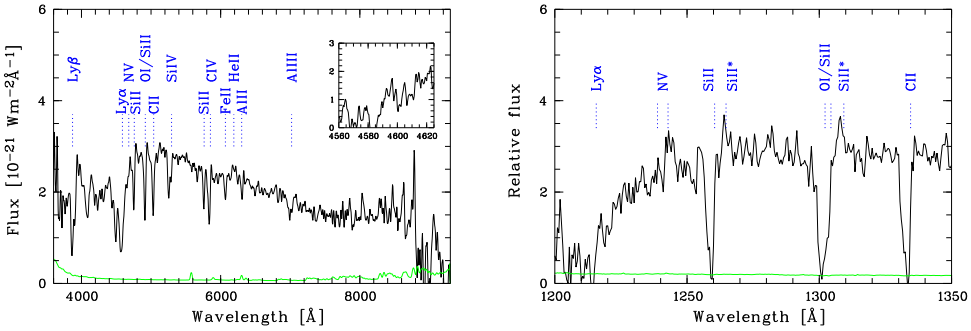

(a) **(b)**

Figure 3.17: (a) Low-resolution spectrum of FDF-5903. The inset shows the medium-resolution spectrum centered at the Lyα line.(b) Medium-resolution spectrum of FDF-5903. The spectrum is shifted into the restframe of the galaxy.

bright cD-galaxy[4] FDF-5908.

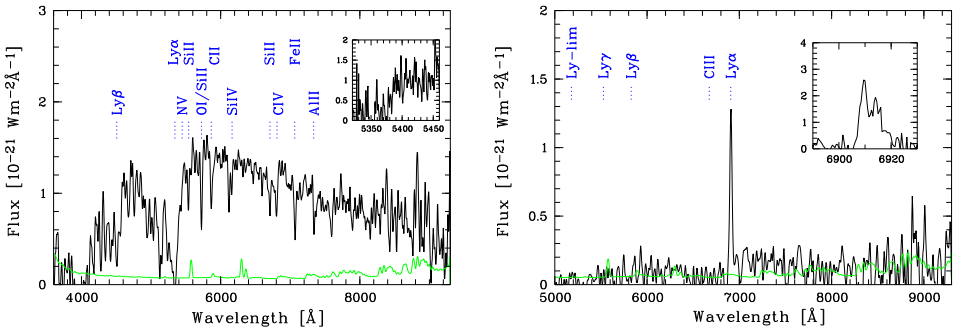

(a) **(b)**

Figure 3.18: (a) Low-resolution spectrum of FDF-6063. (b) Low-resolution spectrum of FDF-6557. Both insets show the corresponding medium-resolution spectra centered at the Lyα line.

The medium-resolution spectrum does not show any Lyα emission and only a broad absorption profile. Besides the lines listed in Tables A.9 to 3.3 the lines SiII* λ1264.74 ($F = 4.64 \pm 1.18 \times 10^{-21}$ W m^{-2} and $EW = 0.85 \pm 0.31$ Å), SiII* λ1309.28 ($F = 3.81 \pm 1.17 \times 10^{-21}$ W m^{-2} and $EW = 0.71 \pm 0.33$ Å) and SiII* λ1533.40 ($F = 6.03 \pm 1.00 \times 10^{-21}$ W m^{-2} and $EW = 1.21 \pm 0.37$ Å) are seen in emission. The interstellar absorption lines corresponds to a redshift of $z = 3.3935 \pm 0.0005$, lower than the redshift derived from the low-resolution spectrum.

The medium-resolution spectrum of FDF-6063 is modelled with a STARBURST99

[4]cD-galaxies have a (c)ompact core and a (D)iffuse envelope. They are among the brightest elliptical galaxies and are often found in galaxy clusters.

spectrum with old age (≈ 100 Myr), SMC/LMC metalicity and an E(B-V) = 0.25.

FDF-6557

FDF-6557 is a galaxy at z=4.6818. The low-resolution spectrum shows the strong Lyα line only (see Fig. 3.18). The Lyα profile is affected by atmospheric lines.

FDF-7539

FDF-7539 (z = 3.2878 and $m_{\rm R}$= 24.1 mag) is a starburst galaxy with a weak Lyα emission (see Fig. 3.19). The galaxy was observed in both medium-resolution setups. The combined medium-resolution spectrum ranges from 1121 to 1697 Å in the rest-frame of the galaxy. The Lyα line shows a double peak profile. The blue component with a flux of $F_{\rm Ly\alpha}$ = 10.22 ± 1.36 × 10^{-21}Wm^{-2} is at a wavelength of 5203.3 Å and the red component with flux of $F_{\rm Ly\alpha}$= 30.99 ± 1.53 × 10^{-21}Wm^{-2} is at a wavelength of 5221.9 Å. Both components are separated by ≈ 1070 kms^{-1}. The central absorption component is located at 5211.8 Å, corresponding to a redshift of z = 3.2872. For FDF-7537 we assume that the redshift of the Lyα is given by the central depression.

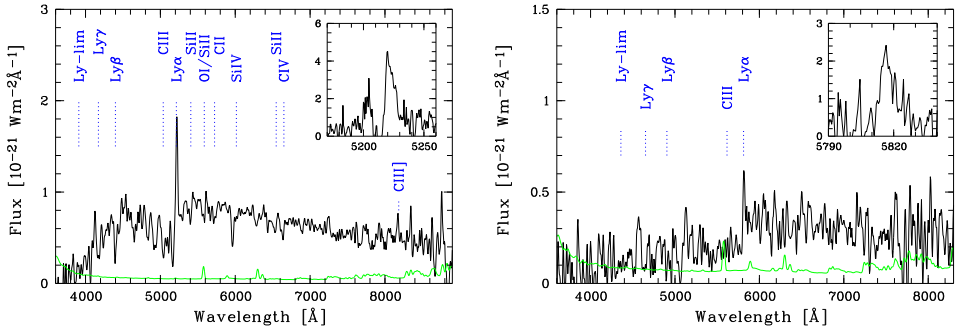

Figure 3.19: (a) Low-resolution spectrum of FDF-7539, the inset shows the medium-resolution spectrum centered at the Lyα line. (b) Low-resolution spectrum of FDF-7683, the inset shows the medium-resolution spectrum centered at the Lyα line

The medium-resolution spectrum of FDF-7539 is modelled with STARBURST99. In Fig. 3.7 a STARBURST99 spectrum with old age (≈ 100 Myr), SMC/LMC metalicity and an E(B-V) = 0.2 is compared to the medium-resolution spectrum. While the spectrum is noisy and the parameters are only an estimate, the small width of the absorption through of CIV $\lambda\lambda$1548, 1551 is in agreement with SMC/LMC metalicity and the non-detection of the NV $\lambda\lambda$1238.82, 1242.80 line demonstrate that FDF-7539 is an old starburst.

FDF-7683

FDF-7683 (z = 3.7812 and $m_{\rm R}$= 24.93 mag) shows a weak, asymmetric Lyα line. The most prominent spectral feature is the continuum break at the Lyα-

wavelength, no other lines except Lyα are detected (see Fig. 3.19). The Lyα line is measured in the low-resolution spectrum.

FDF-8304

FDF-8304 was not observed during the FDF-spectroscopic survey and was selected for observation with the 1200R setup because of the photometric redshift of $z_{\rm phot} = 4.02$. The detection of the Lyα line at 6330.1 Å, the detection of three interstellar medium lines and the continuum break at the wavelength of the Lyα line allows to derive a redshift of $z = 4.205$ (see Fig. 3.20).

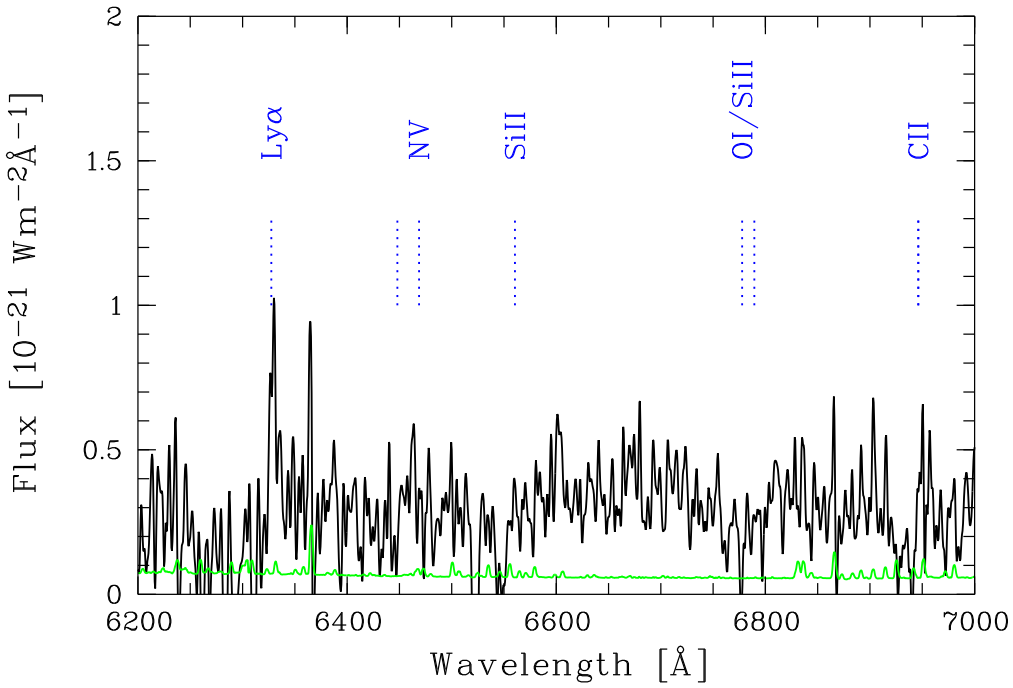

Figure 3.20: Medium-resolution spectrum of FDF-8304.

The slope of the continuum could not be derived. The signal-to-noise ratio of the Lyα line is low and is affected by atmospheric lines, and only the central wavelength and $FWHM = 500 \pm 100$ kms^{-1} can be derived.

The medium-resolution spectrum only covers the rest-frame wavelength range of 1145 to 1432 Å and the continuum signal-to-noise ratio is only $SNR = 3.3$. If the emission line at 6462.9 Å is the emission component of a NV $\lambda\lambda$1239, 1243 P-Cygni profile, only starburst models with a young age (< 100 Myr) can explain this emission.

FDF-9002

FDF-9002 was observed by the FDF spectroscopic survey but is not included in the FDF photometric catalog. The low-resolution spectrum shows a strong line and a continuum (see Fig. 3.21). The object is in the vicinity (4 arcseconds, which

corresponds at this redshift to 30 kpc) of the bright QSO 0103-260 (FDF-4683). The strong line falls at the wavelength of the Lyα of the QSO. The emission line is likely Lyα. FDF-9002 is at a redshift of $z = 3.374$.

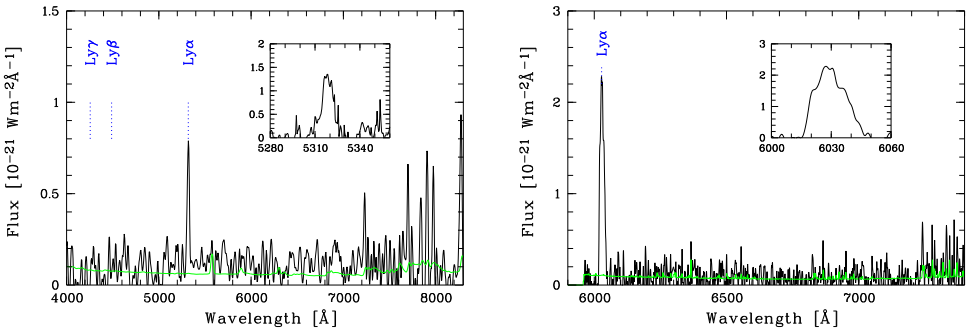

(a) **(b)**

Figure 3.21: (a) Low-resolution spectrum of FDF-9002, the inset shows the medium-resolution spectrum centered at the Lyα line. (b) Medium-resolution spectrum of FDF-9015, inset shows the spectrum centered at the emission line

The object is diffuse ($\approx$ 1.5 arcseconds) and complex (three knots) in the I-Band image. The narrow band image centered at 5300 Å shows also a diffuse object.

The medium-resolution spectrum has obtained only 50 % of the Lyα flux observed with the low-resolution spectrum, which can be explained by different observed regions. The flux of the Lyα line (measured in the low-resolution spectrum) is $F_{\mathrm{Ly}\alpha} = 20.63 \pm 2.72 \times 10^{-21}\mathrm{Wm}^{-2}$, the equivalent width is $EW_{\mathrm{Ly}\alpha} = 56.74 \pm 36.4$ Å. The corresponding Lyα luminosity is $L_{\mathrm{Ly}\alpha} = 2.04 \pm 0.08 \times 10^{35}$ W and the star-formation rate is $SFR_{\mathrm{Ly}\alpha} = 1.86 \pm 0.25\ \mathrm{M}_{\odot}\mathrm{yr}^{-1}$. The Ly$\alpha$ line has a width of FWHM = 480 kms^{-1} and no asymmetry ($a_{\mathrm{wave}} = 1.03$, $a_{\mathrm{flux}} = 1.5$).

Several scenarios are possible for this object, including recombination, which occurs in a infalling cloud around FDF-4683. Or FDF-9002 can be a star-forming region and the Lyα emission is caused by the young stars. The spatial extension of this galaxy makes it plausible, that this galaxy could be a so-called Lyα blob (Steidel et al. 2000; Matsuda et al. 2004). A scenario for FDF-9002 is that an extended cloud (HI and dust) reflects light of the QSO, or the QSO itself ionise the HI cloud and causes a Lyα line (as discussed in Noll 2002). Because the QSO is near, it is likely that a part of the emission is caused by the QSO.

FDF-9015

FDF-9015 is a serendipitous detection and was neither observed by the FDF spectroscopic survey nor it is included in the FDF photometric catalog. The spectrum only shows a single line (Flux = $40.05 \pm 1.19 \times 10^{-21}\mathrm{Wm}^{-2}$ $\mathrm{Å}^{-1}$) at 6027.71 Å and a weak continuum of $F_{\mathrm{cont}} = 0.053 \pm 0.008 \times 10^{-21}\mathrm{Wm}^{-2}$ $\mathrm{Å}^{-1}$ (see Fig. 3.21). The emission line cannot be the [OII] doublet $\lambda\lambda$ 3726.2, 3728.9 or the [OIII] λ5007 with the same arguments as noted for FDF-1267. But the identification of the line remains uncertain. The line is unusual broad (FWHM = 970 kms^{-1}) for

Lyα emission and shows only a slight asymmetry, $a_{\rm wave}$= 1.42 and $a_{\rm flux}$= 1.09. If the line is identified as Lyα the corresponding redshift is $z = 3.957$. The equivalent width would be $EW_{\rm Ly\alpha} = 162 \pm 33$ Å much higher as usual the equivalent width normally derived for high-redshift galaxies.

Chapter 4

Modelling the Lyα emission profile

4.1 Physics of the Lyα line

Lyα photons are emitted by the transition $2^2\mathrm{P} \rightarrow 1^2\mathrm{S}$ of hydrogen. The photons have a wavelength of 1215.67 Å (Wiese et al. 1966). The lifetime of the upper state of 1.25 ns leads to a natural line width of $\approx 10^{-4}$ Å. This line widths is much smaller than line widths caused by Doppler broadening in astrophysical situations. The line profile of Lyα is described by a Voigt profile which is the convolution of a Doppler profile with a Lorentz profile. In the core of the Voigt profile, called the Doppler profile, the absorption is stronger than compared to the absorption in the damping wings of the profile. But since the damping wings decline with λ^{-2} and the Doppler profile with $\mathrm{e}^{-\lambda^2}$ for high neutral column densities the absorption profile is dominated by the damping wings for high optical depths.

Since Lyα is a very important line in astrophysics major efforts have been accomplished to compute and understand the radiative transfer process. The profiles and other quantities like optical path have been computed by Monte-Carlo technics (e.g., Auer 1968; Adams 1972; Ahn et al. 2001), or by Finite Element Methods (Richling et al. 2001) or analytically (Osterbrock 1962; Neufeld 1990).

The Lyα line is a resonance line. Its lower state is the ground state of neutral hydrogen. Resonance lines have a high transition probability, hence Lyα photons are resonance scattered by neutral hydrogen. Compared to, e.g., Hα photons Lyα photons exhibit a different behaviour. In neutral hydrogen Lyα photons experience a diffusion in space, while Hα photons are not scattered and can leave the neutral hydrogen. But with each scattering event, the Lyα photons also change frequency. In HII-regions any collisional broadening can be neglected and Lyα photons are scattered coherently in the rest-frame of the scattering atom. Any thermal motion of the atom will lead to a frequency shift of the Lyα photon (Zanstra 1949). Especially they can be scattered by a rapidly moving atom in the tail of the Maxwell-Boltzmann distribution. While the frequency of the photon does not change in the rest-frame of the atom, the Lyα photons have a high frequency shift in the rest-frame of the gas. If the velocity offset is sufficiently high, the Lyα photon is shifted out of the resonance frequency and become a wing photon. Since the

effective opacity is lower, the escape probability is higher.

Escape mechanism

Adams (1975) realised that there are different escape mechanisms in a neutral hydrogen cloud for Lyα photons, depending on the optical depth τ_0 in line centre. He called the different escape mechanisms single longest flight (for low optical depths) and single longest excursion (for high optical depths). In the following discussion a static hydrogen cloud with a velocity dispersion $\delta\nu_{\rm Doppler}$ is assumed, a = 6.05 $\times$ 10^{-5} / $\rm v_{Doppler}$[100km/s] is the Doppler parameter. Lyα photons with a frequency of ν are generated by a light source within the neutral cloud.

Ahn et al. (2002) expanded the scenario of Adams (1975) and subdivided the optical thickness into three regimes. In the low density limit $\tau_0 < 10^3$ the single longest flight occurs. $10^3 < \tau_0 < 10^3/a$ is a intermediate regime between the single longest flight and the single longest excursion. For $10^3/a < \tau_0$ the single longest excursion occurs.

Single longest flight: After the photon is injected into the neutral medium, the photon is scattered in the Doppler core of the profile and experience only small velocity shifts $\delta\nu_{Doppler}$. The spatial diffusion is also small. But after scattering with a hydrogen atom in the tail of the Maxwell-Boltzmann distribution, the Lyα photon is shifted out of the resonance frequency and become a wing photon. The effective optical depth $\tau_{\rm eff}$ is much lower than the optical depths at line center τ_0 and the photon can escape. If the optical depth at line center is as low as $\tau_0 < 10^3$, the photon can escape without further scatterings in the single longest flight. In moderate optical depths $10^3 < \tau_0 < 10^3/a$ the photon experiences further wing scatterings before it can escape (Ahn et al. 2001).

Single longest excursion: The single longest excursion occurs at high optical depths, $\tau_0 > 10^3/a$. As in the single longest flight the Lyα photon is scattered locally in the line centre and is then scattered by a hydrogen atom in the tail of the Maxwell-Boltzmann distribution. The Lyα photon becomes a wing photon. The Lyα photons are scattered many times in the wings of the Voigt profile of neutral hydrogen atoms. These scatterings are asymmetric, each scattering event shifts the frequency back to the line centre, until they are trapped again in the Doppler core of the profile. This is the so-called restoring force (Osterbrock 1962). After the Lyα photons are trapped they experience further scatterings in the Doppler core until they are scattered by hydrogen atom in the tail of the Maxwell-Boltzmann distribution. The next excursion follows. During one of these excursions the Lyα photon can escape in the single longest excursion.

Emergent Lyα profile

In a static neutral medium the emergent Lyα profile shows a double peak profile, the separation of the double peaks and widths exhibiting the physical properties of the neutral medium. The peak frequency $\nu_\star = \frac{\nu}{\nu_{\rm Doppler}}$ gives the frequency shift

from the line centre for the two peaks. For the low optical depth regime the peak frequency is (Osterbrock 1962)

$$\nu_\star = (ln\tau_0)^{1/2} \tag{4.1}$$

and for high optical depth the peak frequency is (Adams 1972)

$$\nu_\star = (a\tau_0)^{1/3}. \tag{4.2}$$

E.g., for a optical depth of $\tau_0 = 10^3$ and a Doppler width of the neutral medium $v_{\rm Doppler} = 100$ kms^{-1} the Lyα profile would show two peaks at $\pm$ 260 kms^{-1} shifted from the initial frequency of the photons.

Number of scatterings and optical path

The actual number of scatterings is very high and is roughly proportional to the optical depth $< N > \propto \tau_0$ (Adams 1972), independing of the damping parameter a. In a random walk in physical space the number of scatterings is proportional to the square of the optical depth $< N > \propto \tau_0^2$. The number of scattering for Lyα photons is reduced compared to a random walk in physical space, because the Lyα diffuses in frequency and physical space. The optical path l is expressed by the ratio f of the distance travelled by the photon to the physical radius of the neutral medium. For a spherical distribution of the neutral hydrogen in the limit of high optical depth is (Adams 1975)

$$f = (a\tau_0/\sqrt{\pi})^{1/3} \tag{4.3}$$

The optical path l of a Lyα photon depends only weakly on the optical depth and is of the order of $l = 15 \times r$ for moderate Doppler widths Adams (1975), where r is the radius of the neutral region. The optical path is lower for a moderate optical depth, also a higher turbulence would decrease the optical path.

Destruction of Lyα photons

The Lyα photons can be destroyed by several mechanisms including conversion of Lyα into the two-photon continuum by collision. But the most import is the absorption by dust. UV photons have a high probability to be absorbed by dust especially if the optical path is increased.

We estimate the column density of the neutral hydrogen when Lyα photons are absorbed, assuming a Galactic dust-to-gas ratio and a homogenous ISM. For a large range of τ_0 the optical path is $f \approx 15$, we further assume $A_{\rm Ly\alpha} = 11.5$ $E(B-V)$ (Leitherer et al. 2002), and $< N_{\rm HI}/E(B-V) > = 5 \times 10^{-21}$ cm^{-2}/ mag (Milky Way, Savage & Mathis 1979). These assumptions leads to a critical column density of the neutral hydrogen $N_{\rm HI} \approx 2.2 \times 10^{19}$ cm^{-2}, where the flux of Lyα is reduced by dust of factor of two. This estimation was also done also by Charlot & Fall (1993) or Auer (1968).

In the above arguments a homogenous interstellar medium is assumed. But as Neufeld (1991) pointed out an inhomogeneous medium and geometrical configuration like a two-phase interstellar medium, where the dust-gas-ratio is constant,

can lead to the increase of Lyα photons emission to continuum radiation. In the two-phase interstellar medium described by Neufeld (1991) regions with a neutral column density and large amount of dust are embedded in a low-density gaseous, almost dust-free phase. The UV-continuum is not scattered by neutral hydrogen and will travel through the high density regions. Hence it will be affected by a larger amount of dust. Lyα photons, which originate in the low-density phase, are reflected at the outskirts of the dense neutral regions and hence travelling only in a environment with a low amount of dust.

4.2 Finite elements calculations

In order to constrain the physical properties of the Lyα emitting regions of the galaxies, we calculated model profiles using the finite element line formation code of Richling and Meinköhn (Richling et al. 2001; Meinköhn & Richling 2002). The code is particularly well suited for calculating the radiative transfer in a non-static scattering medium. In Richling et al. (2001), Meinköhn (2002), Meinköhn & Richling (2002), and Richling (2003) the code is described in detail. Here we give a short overview of the code. The finite element code solves the non-relativistic radiative transfer equation in the comoving frame. Since complete distribution is assumed and the Voigt profile is approximated by a Dopper profile, the code is only valid for low optical depths (up to $\tau_0 \approx 10^4$). The multi-frequency transfer equation are transformed into N monochromatic radiative transfer equations, which are discretised using Standard Galerkin finite elements. The resulting equations are solved in a iterative way, using a posteriori error estimation strategy to redefine the grid.

4.2.1 Radiative transfer equation

The non-relativistic radiative transfer equation in the comoving frame for a three-dimensional domain Ω is:

$$\big(T + D + S + \chi(x,\nu)\big) I(x,n,\nu) = f(x,\nu). \tag{4.4}$$

The transfer operator T, the Doppler operator D, and the scattering operator S are defined by

$$TI(x,n,\nu) = n \cdot \nabla_x I(x,n,\nu), \tag{4.5}$$

$$DI(x,n,\nu) = w(x,n)\,\nu \frac{\partial}{\partial \nu} I(x,n,\nu), \tag{4.6}$$

$$SI(x,n,\nu) = -\frac{\sigma(x)}{4\pi} \int_0^\infty \int_{S^2} R(\hat{n},\hat{\nu};n,\nu) I(x,\hat{n},\hat{\nu})\, d\hat{\omega}\, d\hat{\nu}. \tag{4.7}$$

x is the three-dimensional space variable, n is the direction which points to the solid angle dω of the unit sphere S^2, ν is the frequency, $f(x,\nu)$ is the source term, the invariant specific intensity I is six-dimensional.

The extinction coefficient $\chi(x,\nu) = \chi(x,\nu)_L + \kappa(x)_C$ is the sum of the extinction coefficient of the line center $\chi(x,\nu)_L = \kappa(x,\nu)_L + \sigma(x,\nu)_L$ and the absorption coefficient of a continuous absorber.

A Doppler profile is adopted

$$\phi(\nu) = \frac{1}{\sqrt{\pi}\,\Delta\nu_D} \exp\left[-\left(\frac{\nu-\nu_0}{\Delta\nu_D}\right)^2\right], \tag{4.8}$$

where ν_0 is the frequency of the line center. The Doppler width $\Delta\nu_D$ is determined by

$$\Delta\nu_D = \frac{\nu_0}{c}\sqrt{v_{\text{therm}}^2 + v_{\text{turb}}^2}. \tag{4.9}$$

The Doppler profile is a reasonable description for of a line profile, if the turbulence velocity v_{turb} exceeds the v_{therm} and the Doppler core is very broad.

Wehrse et al. (2002) found a non-relativistic formulation of the Doppler parameter D, which describes the Doppler shift of the photons $DI(x,n,\nu) = w(x,n)\cdot \nu\frac{\partial}{\partial\nu}I(x,n,\nu)$. $w(x,n)$ is the gradient of the velocity field $v(x)$ in direction n

$$w(x,n) = -n\cdot\nabla_x\left(n\cdot\frac{v(x)}{c}\right). \tag{4.10}$$

For the redistribution function $R(\hat{n},\hat{\nu},n,\nu)$ isotropic scattering and complete redistribution is assumed.

$$R(\hat{\nu},\nu) = \phi(\hat{\nu})\phi(\nu). \tag{4.11}$$

The scattering term S^{crd} is in the case of complete redistribution

$$S^{\text{crd}}I(x,n,\nu) = -\frac{\sigma(x,\nu)}{4\pi}\int_0^\infty \phi(\hat{\nu})\int_{S^2} I(x,\hat{n},\hat{\nu})\,d\hat{\omega}\,d\hat{\nu}. \tag{4.12}$$

4.2.2 Finite element discretisation

General description of the FEM

Before we discuss the finite element discretisation for the radiative transfer equation, a short general overview over the finite element method is here given. In Meinköhn (2002) a detailed description of the finite element method is provided.

Basis of the finite element method is the weak formulation of the corresponding differential equation. The weak formulation of the differential equation is to find a $u \in S$ for

$$a(u,v) = \langle l, v\rangle \forall v \in S \tag{4.13}$$

where S is the Sobolew space, $a(.,.)$ is a bilinear function and $\langle .,.\rangle$ is the scalar product. u is the solution of the weak formulation of the differential equation.

Instead of solving 4.13 on S, the weak formulation can be solved on the finite space S_{h}, where h is the discretisation parameter. Eq. 4.13 is in discrete formulation

$$a(u_{\text{h}}, v_{\text{h}}) = \langle l, v_{\text{h}}\rangle \forall v_{\text{h}} \in S_{\text{h}} \tag{4.14}$$

For $h > 0$, u_{h} becomes $u_{\text{h}} = \text{u}$ under certain conditions (see Meinköhn 2002).

If v_{h} is chosen as a bases of S_{h}, e.g., $(\psi_1, \psi_2, ..., \psi_N)$ and with

$$u_{\text{h}} = \sum_{k=1}^{N} z_k\psi_k, \tag{4.15}$$

the equation 4.14 can be written in matrix-vector formulation as

$$Az = b \tag{4.16}$$

where $A = a(\psi_k, \psi_i)$ and $b = l, \psi_i$. The complete problem is now described by linear equations. A and b are known, the vector z contains the coefficients of the solution.

The differential equation is defined in a spatial domain Ω with the corresponding boundary conditions. The discretisation of the spatial domain Ω with finite elements is needed. It is called a triangulation. The space of the allowed function $\mathrm{V_h}$ is defined by polynomial of low order. The coefficients of the polynomial are defined on the knots of the triangulation. In order to solve the linear equations in short computation time the matrix A in 4.16 should be as simple as possible. This can be reached by chosing the bases ψ_i as the knots of the triangulation.

Finite element discretisation for the radiative transfer calculations

The trial space W_h is a product of three sets $W_\mathrm{h} = \Omega \times S^2 \times F$. Ω is the spatial domain and S^2 is the unity sphere and F is here the space of frequencies. All subspaces have to be triangulated to solve discrete equations. Since using standard Galerkin discretisation for the frequency-dependent transfer problem needs large amounts of computation time, the frequency is discretisated into equidistantly distributed frequency intervals and an implicit Euler method is used to discretisize the Doppler term. The resulting equations are rewritten as a monochromatic radiative transfer equations and the Galerkin discretisation is used to triangulate the unity sphere and the spatial domain for each of the monochromatic radiative transfer equations.

An implicit Euler method for N equidistantly distributed frequency points $\nu_i \in \{\nu_1, \nu_2, ..., \nu_N\} \subset \Lambda$ is used, where $\Lambda := [\nu_0, \nu_{N+1}]$. Since the function $w(x, n)$ may change its sign, the Doppler term reads

$$w(x,n)\nu\frac{\partial I}{\partial \nu} \longrightarrow w\nu_i\frac{I_i - I_{i-1}}{\Delta\nu} \qquad (w_i > 0) \tag{4.17}$$

and

$$w(x,n)\nu\frac{\partial I}{\partial \nu} \longrightarrow w\nu_i\frac{I_{i+1} - I_i}{\Delta\nu} \qquad (w_i < 0), \tag{4.18}$$

where $\Delta\nu$ is the constant frequency step size. All quantities referring to the discrete frequency point ν_i are denoted by an index "i". Employing the Euler method and using a quadrature method for the integral over the frequency in the scattering operator, eq. 4.4 can be written as

$$\Big(T + \chi_i + \phi_i q_i S^{\mathrm{coh}} + \frac{|w|\nu_i}{\Delta\nu}\Big) I_i = \tilde{f}_i + \frac{\sigma_i}{4\pi}\sum_{j\neq i}^{N} \phi_j q_j \int_{S^2} I_j d\hat{\omega} \tag{4.19}$$

where the scattering term for coherant scattering S^{coh} is defined as

$$S^{\mathrm{coh}} I(x,n,\nu) = -\frac{\sigma(x,\nu)}{4\pi}\int_{S^2} I(x,\hat{n},\nu)\, d\hat{\omega} \tag{4.20}$$

The quantity I_i in eq. 4.19 is the unknown variable, where the intensities I_j are known from solving the last iteration. The q_i are the weights from the quadrature method, used to solve the frequency integral in the scattering operator. The additional terms on the left side can be interpreted as a artificial opacity and the additional terms on the right side as artificial source terms. Eq. 4.19 can be written as

$$A_i I_i = f_i \tag{4.21}$$

This semi-discrete monochromatic equation is triangulated in the spatial domain and in the unity sphere using the Galerkin-approach (Richling 2003). On the unity sphere S^2 a discretisation based on a refined icosahedron is used.

The resulting complete discrete system in matrix form is:

$$A^{\mathrm{crd}} u = f. \tag{4.22}$$

where u is the vector containing the discrete intensities and vector f the source. The complete discrete system is not solved, because the resulting linear system would be too large. The discrete system is rewritten as

$$\tilde{A}_i^{\mathrm{crd}} u_i = \hat{f}_i, \tag{4.23}$$

with a modified right hand side

$$\hat{f}_i = f_i + R_i u_{i+1} + B_i u_{i-1} + \sum_{j \neq i} Q_j u_j. \tag{4.24}$$

Factors B_i and R_i are containing the contribution of the Doppler factor $w(x,n) \cdot \nu_i/\Delta\nu$, and Q_j holds the terms from the quadrature scheme. This can be interpreted as an monochromatic transfer equation. Not the complete matrix is solved, but N monochromatic transfer equations are solved in a iterative way. The iterative procedure is necessary, because each of the monochromatic transfer equations needs the solution of the other monochromatic transfer equations.

The algorithm states:

1. Start with $I = 0$ for all frequencies.
2. Solve Eq. 4.23 for $i = 1, .., N$.
3. Repeat step 2 until convergence is reached.
4. Refine grid and repeat step 2 and 3.

The grid is refined on bases of a posteriori error estimator. The cells are ordered according the size of the error and the cells with the largest errors are refined.

Boundary conditions

The frequency discretisation is restricted to a finite interval $\Lambda := [\nu_0, \nu_{N+1}]$. Since the Doppler operator shifts the photon to lower and higher frequency, a boundary

condition on the lowest and highest allowed frequency is necessary. The following boundary condition has to be applied:

$$I(x, n, \nu) = 0 \qquad \text{on } \Sigma \tag{4.25}$$

where $\Sigma = \Omega \times S^2 \times \{\nu_0, \nu_{N+1}\}$. No continuum is assumed. In addition the following boundary condition has to imposed

$$I(x, n, \nu) = 0 \qquad \text{on } \Gamma^- \times \Lambda. \tag{4.26}$$

where $\Gamma^- \times \Lambda = \big\{(x, n, \nu) \in \Gamma |\, n_\Gamma \cdot n < 0\big\}$. The second boundary condition implies that no light source is outside the model. n_Γ is the unit vector perpendicular to the boundary surface Γ of the spatial domain Ω.

Model configuration

A spherical two-component model with a central line emission region surrounded by a shell of neutral HI gas is assumed. Configurations of this type have been suggested and investigated earlier by Tenorio-Tagle et al. (1999), Ahn et al. (2001, 2003) and Mas-Hesse et al. (2003). The width and the shape of the lower part of the profile of FDF-4691 is best explained by the emission of (high-velocity) turbulent HII regions, while the narrow central absorption can be produced only in a low-velocity HI layer in front of the emission region. Moreover this model may explain the observed P-Cygni profiles of LAEs galaxies in the FDF.

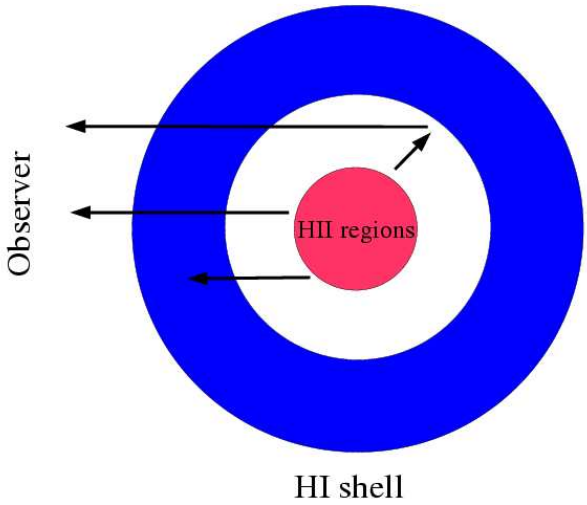

Figure 4.1: Sketch of the model used.

The velocity field is assumed to be of the form

$$v_{\rm io} = v_0 \left(\frac{r_0}{r}\right)^l \frac{x}{r}, \tag{4.27}$$

where $r = |x|$ and v_0 the scalar velocity at radius r_0. l is a free parameter and is set l = -0.5. This parameter has only a marginal impact on the emergent profile.

The shell is located between $r = 0.6$ and $r = 0.7$. The turbulent core has $r = 0.15$. Also these parameters have little influence on the resulting profiles.

Transformation into the observer's restframe

A normalised form of the radiative transfer equation is used. Coordinates in physical units can be obtained by simple transformation. A particular line and the corresponding frequency scale has to be defined when transforming into the observer's frame.

¿From the solution $I(x, n, \nu)$ in the comoving frame, the solution $\tilde{I}(x, n, \tilde{\nu})$ in the observers frame is obtained by performing the transformation (Mihalas 1978):

$$\tilde{I}(x, n, \tilde{\nu}) = I(x, n, \tilde{\nu}) \left(\frac{\tilde{\nu}}{\nu}\right)^3, \tag{4.28}$$

where

$$\tilde{\nu} = \nu \left(1 + n \cdot \frac{v(x)}{c}\right). \tag{4.29}$$

4.2.3 Lyα profile modelling for FDF-4691

For the emission from the central region we assumed a broad Gaussian Lyα emission profile. This assumption seems reasonable in view of the expected supernova rate and stellar wind activity in the observed compact starburst region. The turbulent velocity of the central source was adjusted to fit the outer wings of the observed profile which are not affected by the low-velocity gas of the shell.

The computed model profile best fitting the observed profile is reproduced in Fig. 4.2. The theoretical model was convolved with the instrumental profile. The parameters for this model are turbulence velocities of about 600 km s^{-1} in the emission region, of 63 km s^{-1} in the scattering shell, and an outflow velocity of the shell of 12 km s^{-1}. The central HI column density of the shell was $N(HI) \approx 4{\times}10^{17}$ cm^{-2}, corresponding to an optical depth of the shell in the line centre of $\tau_0 \approx 5000$.

In the model described above the central absorption of the line profile is produced by the removal of Lyα photons from the line centre by multiple resonance scattering. Without dust absorption the resonance scattering redistributes all these photons in velocity space to produce the blue and and red peaks framing the central absorption.

Since the rest intensity at the line centre is too high in our model, we expect that we underestimated the neutral column density. A higher neutral column density would increase the separation between the two peaks, allowing to reproduce a similar model as in Fig. 4.2 with lower shell turbulence velocity. Unfortunately, at present, the code cannot handle much higher optical depths.

Influence of dust

Calculations with Galactic dust/gas ratio and Galactic dust properties and without dust in the neutral shell showed that with the model parameters given above the

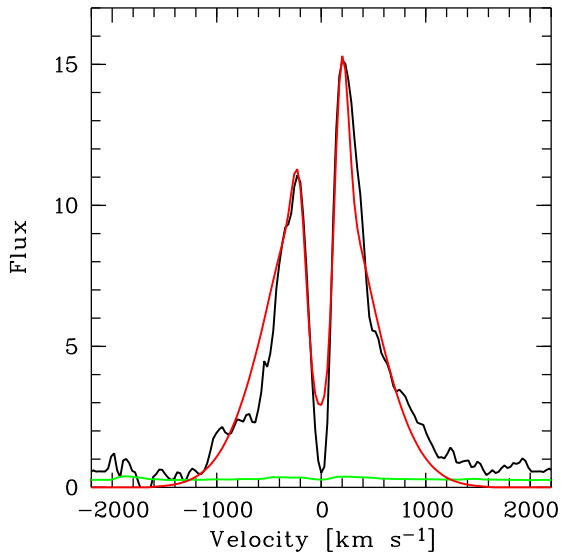

Figure 4.2: Comparison of the Lyα line of FDF-4691 (black line) and the best-fit theoretical model (red line).

dust in the shell had no detectable effect on the line profile. As shown in Sec. 4.1 estimations suggest that a up to 100 × higher column density of the neutral shell with a Galactic dust/gas ratio will not result in a significant reduction of Lyα photons in the shell. At higher neutral column densities the destruction of Lyα photons will become important. One can assume that dust in the central emission region, if not destroyed by the strong radiation field, only reduces the total emission without modifying the profile. But Ahn (2004) showed that an expanding shell will cause several redshifted peaks, unless dust is distributed within the core. Since Lyα photons are reflected by neutral hydrogen, they cross the interior several times and are likely affected by dust within the shell.

Note that with a Galactic dust/gas ratio the amount of dust in the shell is very low. In this model the strong Lyα emission line is caused by an intrinsically broad Lyα line, allowing a high fraction of Lyα photons to escape unaffected by the neutral shell, and a low column density of the neutral shell.

4.2.4 Lyα profile modelling for FDF-5215

Model configurations

For FDF-5215 the same geometrical model was assumed as in the case of FDF-4691. A two-dimensional configuration was assumed.

Results

The parameters for this model (see Fig. 4.2.4) are turbulence velocities of about 500 km s^{-1} in the emission region, of 125 km s^{-1} in the scattering shell, and an

outflow velocity of the shell of 125 km s^{-1}. The central HI column density of the shell was $N(HI) \approx 2 \times 10^{15}$ cm^{-2}, corresponding to an optical depth of the shell in the line center of $\tau_0 \approx 10$. While τ could not well constrained for the model of FDF-4691, an upper limit can be found here. τ can not exceed $\tau = 10$ by an order of magnitude. This limits the HI colum density to $N(HI) < 2 \times 10^{16}$ cm^{-2}. As discussed in Sec. 4.4 it is likely that the shell is ionised and only a fraction is neutral.

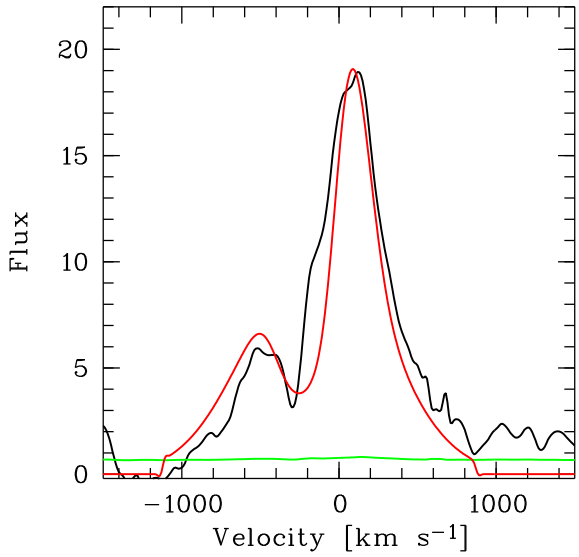

Figure 4.3: Comparsion of the Lyα line of FDF-5215 (black line) and the best-fit theoretical model (red line).

4.3 Modelling Lyα with Gauss emission and Voigt absorption profiles

4.3.1 Method

Kunth et al. (1998), van Ojik et al. (1997), and Dawson et al. (2002) modelled Lyα profiles with Gauss emission(s) and a Voigt absorption components. The components are computed and simply multiplied. A simple radiative transfer process is assumed, all photons absorbed by the neutral component are absorbed by dust or scattered away and hence are not re-emitted. The assumption is valid for dusty neutral clouds or large neutral clouds (Kunth et al. 1998). The extended neutral cloud absorbs the Lyα photons. If the Lyα photons are not destroyed by dust, the photons are emitted again, but the surface brightness of the cloud is too low to be observed (Kunth et al. 1998). The assumption might not be correct for compact neutral clouds, where the surface brightness is higher.

We model the profiles of the LAEs in the FDF with Gauss components and Voigt absorptions profiles. In some cases a continuum is added. The continuum

decrement caused by the Lyα forest is accounted by adopting an effective opacity $\tau_{\rm eff}$ of the intergalactic medium. The continuum decrement by the combined effect of many Lyα lines is given by Madau (1995):

$$\tau_{\rm eff} = 0.0036(z+1)^{3.46} \tag{4.30}$$

Since a wide range of parameters is possible for these fits, the number of components is to be kept as low as possible. For this reason, the fits are made for one single component only, adding further components only if the normalised χ^2 is too high.

4.3.2 Results on individual objects

FDF-1267

The profile of FDF-1267 is modelled with two emission components and one absorption component. No continuum was assumed. Models with less than three components had a significantly higher χ^2. In Fig. 4.4 a theoretical model is shown. The parameters for the main emission line are: $z = 2.7872$, $F_1 = 35.5 \times 10^{-21}\mathrm{Wm}^{-2}$ and $FWHM_1 = 341$ kms^{-1}. The second emission component with $F_2 = 1.35 \times 10^{-21}\mathrm{Wm}^{-2}$ and $FWHM_1 = 41.7$ kms^{-1} is redshifted with respect to the first emission line by 326 kms^{-1} . The absorption component with $\mathrm{v_{Doppler}} = 20$ kms^{-1} and $N_{\rm HI} = 5 \times 10^{17}$ cm^{-2} is blue-shifted by -130 kms^{-1} . The velocity offset of 326 kms^{-1} is an upper value, the second emission component can be modelled with lower velocity offset to the main emission component by increasing the flux and the width of the line. Also the range of neutral column densities which fit the profile is large.

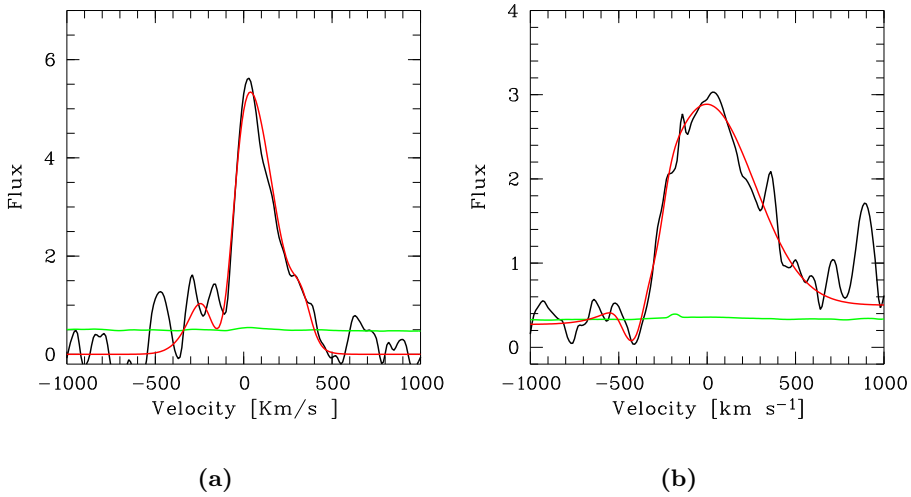

(a) **(b)**

Figure 4.4: Comparison of the observed Lyα (black line) with the theoretical model (red line). The green line indicates the noise level. a) FDF-1267, b) FDF-1337.

FDF-1337

The profile of FDF-1337 was modelled with one emission and one absorption component. The addition of a second emission component minimised χ^2 further, but not significantly. The fit shown in Fig. 4.4 has a emission component with $z = 3.4079$, $F = 29.0 \times 10^{-21}\mathrm{Wm}^{-2}$ and $FWHM = 640$ kms^{-1} , and a blue-shifted (-420 kms^{-1}) absorption with $\mathrm{v_{Doppler}} = 20$ kms^{-1} and $N_{\mathrm{HI}} = 10^{17}$ cm^{-2}. The parameter space is not well constrained. However, assuming that the absorption component is at the same redshift as the low-ionisation absorption lines, the hydrogen absorption component has an upper limit of $N_{\mathrm{HI}} = 10^{19}$ cm^{-2} .

FDF-2384

For FDF-2384 two emission and one absorption components are needed. In Fig. 4.5 a fit with the three components is plotted. The first emission component has the parameters: $z = 3.3141$, $F_1 = 135 \times 10^{-21}\mathrm{Wm}^{-2}$ and $FWHM_1 = 310$ kms^{-1}. The second emission component is red-shifted by 315 kms^{-1} , $F_2 = 20.5 \times 10^{-21}\mathrm{Wm}^{-2}$ and $FWHM_2 = 242$ kms^{-1}. The absorption component is blue-shifted by -200 kms^{-1} , $\mathrm{v_{Doppler}} = 40$ kms^{-1} and $N_{\mathrm{HI}} = 5 \times 10^{17}$ cm^{-2}. The second emission component can be modelled with lower velocity offset with respect to the main velocity offset. Both emission components can be placed at the same redshift, the broad emission component has a line width of $FWHM_2 = 650$ kms^{-1} .

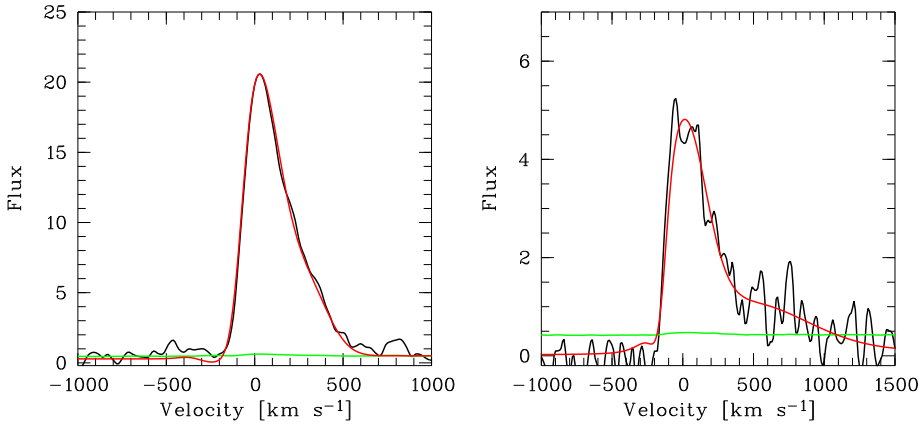

(a) **(b)**

Figure 4.5: Comparison of the observed Lyα (black line) with the theoretical model (red line). The green line indicates the noise level. a) FDF-2384, b) FDF-3389.

FDF-3389

Two emission components and one absorption component are needed to model the profile of FDF-3389. The first emission component in the model shown in Fig. 4.5 is at $z = 4.5817$ kms^{-1} with $F_1 = 37.5 \times 10^{-21}\mathrm{Wm}^{-2}$, $FWHM_1 = 360.0$ kms^{-1}

. The second emission component is red-shifted by 429 kms^{-1} with $F_2 = 25.0 \times 10^{-21}$Wm^{-2} , $FWHM_2 = 1037$ kms^{-1} . The absorption component is blue-shifted by -181 kms^{-1} with $v_{\rm Doppler} = 10.0$ kms^{-1}and $N_{\rm HI} = 2 \times 10^{17}$ cm^{-2}. Also a weak continuum is assumed (0.1×10^{-21}Wm^{-2} Å^{-1}). The same degeneracy as in the modelling of FDF-1267 occurs. The Lyα profile can be modelled with two emission components at the same redshift. The broader component is unusual broad with $FWHM_2 = 2000$ kms^{-1}.

FDF-4454

The blue edge of the profile of FDF-4454 does not drop off steeply. The profile can be fitted by two Gaussian emission components without any additional absorption component. In Fig. 4.6 the model is shown. The parameters for the first emission are $z = 3.0845$ kms^{-1} with $F_1 = 26.5 \times 10^{-21}$Wm^{-2} , $FWHM_1 = 295$ kms^{-1} and the second emission component is redshifted by 278 kms^{-1} and has $F_2 = 3.5 \times 10^{-21}$Wm^{-2} , $FWHM_2 = 137$ kms^{-1}. The profile cannot be described by two Gaussian components at the same redshift, unless an additional absorption component is added.

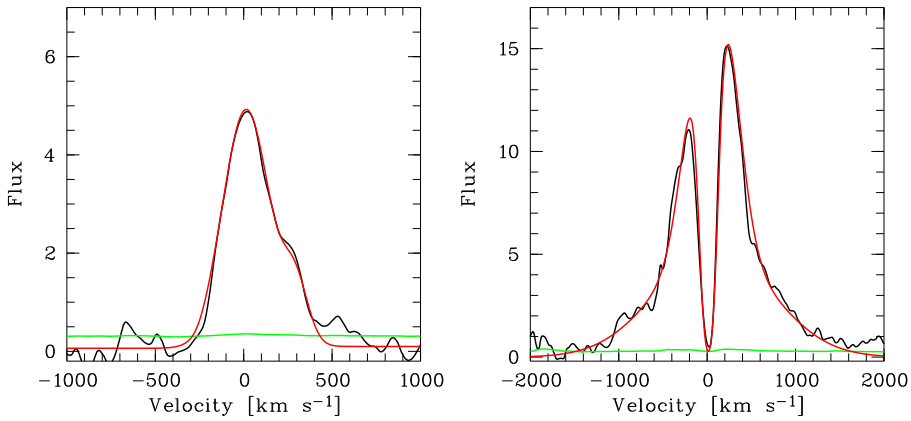

(a) **(b)**

Figure 4.6: Comparison of the observed Lyα (black line) with the theoretical model (red line) The green line indicates the noise level. a) FDF-4454, b) FDF-4691.

FDF-4691

FDF-4691 is modelled with two emission components and one absorption component. A variety of parameters are suitable for this emission profile. The model shown in Fig. 4.6 has the following components: an emission at $z = 3.3141$, with $F_1 = 150 \times 10^{-21}$Wm^{-2} and $FWHM_1 = 1500$ kms^{-1} and a second emission component shifted by -17 kms^{-1} to the first component with a flux of $F_2 = 210 \times 10^{-21}$Wm^{-2} and a width of $FWHM_2 = 520$ kms^{-1} . The absorption component

with $v_{Doppler} = 20$ kms^{-1} and $N_{HI} = 5 \times 10^{18}$ cm^{-2} is blue-shifted by 57 kms^{-1}.The Dopper width and the neutral colum density are degenerated, the observed profiles can be described by increasing the neutral column density with a corresponding lowering of $v_{Doppler}$. The possible neutral column densities ranges from $N_{HI} = 5\times 10^{14}$ to $N_{HI} = 10^{19}$ cm^{-2} with $v_{Doppler}$ ranging from 100 kms^{-1} to 10 kms^{-1} .

FDF-5215

The model shown in Fig. 4.7 consists of one emission component and one absorption component. The emission component is at a redshift of $z = 3.1479$ kms^{-1} with a flux of $F_1 = 160 \times 10^{-21}$Wm^{-2} , and a width of $FWHM_1 = 730.0$ kms^{-1} . The absorption component with $v_{Doppler} = 100$ kms^{-1} and $N_{HI} = 2.5 \times 10^{14}$ cm^{-2} is blue-shifted by 268 kms^{-1} . The possible neutral column densities ranges from N_{HI} $= 2.5 \times 10^{14}$ to $N_{HI} = 2.5 \times 10^{18}$ cm^{-2} with $v_{Doppler}$ ranging from 100 kms^{-1} to 10 kms^{-1} .

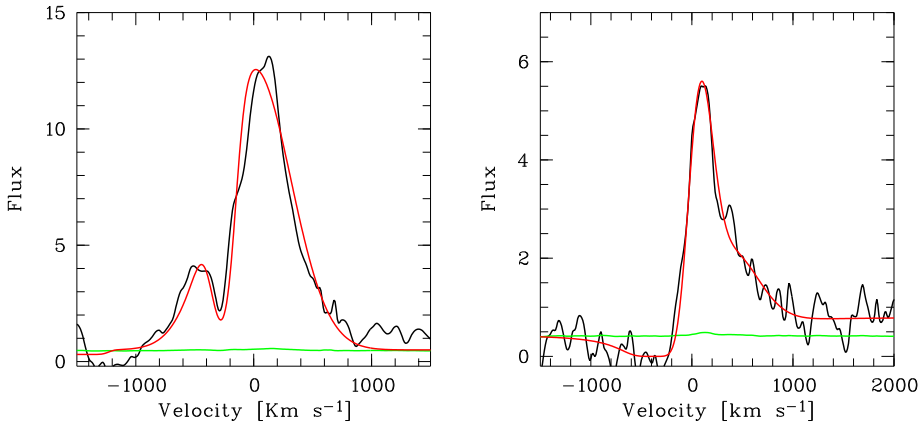

(a) **(b)**

Figure 4.7: Comparison of the observed Lyα (black line) with the theoretical model (red line). The green line indicates the noise level. a) FDF-5215, b) FDF-5550.

FDF-5550

The profile of FDF-5550 is modelled with three components consisting of two emission and one absorption component. A model is shown in Fig. 4.7. The main emission line is at redshift of $z = 3.3844$ with $F_1 = 60.5 \times 10^{-21}$Wm^{-2}and $FWHM_1 =$ 300 kms^{-1} and the second line red-shifted with respect to the first by 310 kms^{-1} , $F_2 = 23.5 \times 10^{-21}$Wm^{-2} , FWHM$_2$ = 650 kms^{-1}. The velocity offset between the two emission lines of 310 kms^{-1} is an upper limit. The Lyα profile can be modelled with a smaller velocity offset between the two lines, increasing the line width of the second emission line. The absorption component is blue-shifted with respect to main emission line by 390 kms^{-1}. The neutral column density of $N_{HI} = 5 \times$

10^{19} cm^{-2} is partly constrained by the absorption of continuum blue-wards of the Lyα emission line.

FDF-5812

The line is fitted with two emission and one absorption component. The parameters of the model shown in Fig. 4.8 are: $z = 4.993$, $F_1 = 75.5 \times 10^{-21}$Wm^{-2}, $FWHM_1$ = 300 kms^{-1} and the second line red-shifted with respect to the first by 270 kms^{-1}, $F_2 = 12.5 \times 10^{-21}$Wm^{-2} , $FWHM_2 = 241$ kms^{-1}. The absorption component with $N_{\rm HI}$ = 2.0 × 10^{-18} cm^{-2} and v$_{\rm Doppler}$ = 20.0 kms^{-1} is blue-shifted with respect to the main emission line by -227 kms^{-1} . The velocity offset of 270 kms^{-1} is an upper limit. The Lyα profile can be modelled with no velocity offset between the two emission components. This implies one narrow emission component ($FWHM$ = 160 kms^{-1}) and one broad (600 kms^{-1}).

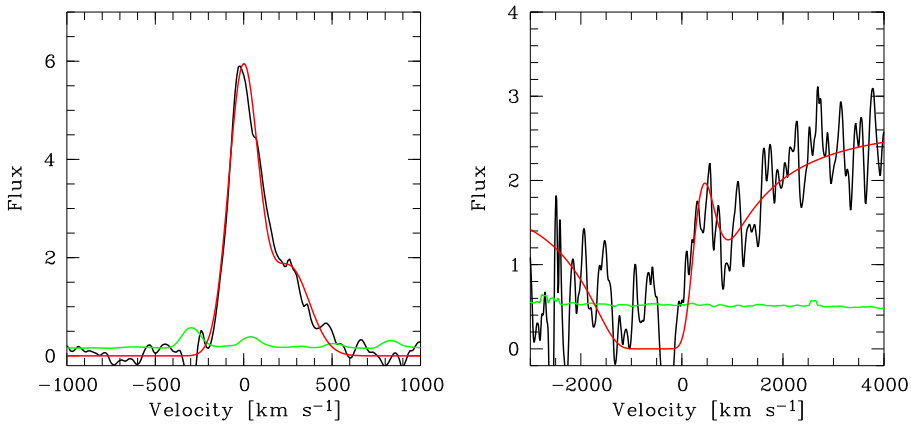

(a) **(b)**

Figure 4.8: Comparison of the observed Lyα (black line) with the theoretical model (red line). The green line indicates the noise level. a) FDF-5812, b) FDF-5903.

FDF-5903

The profile is described by a strong absorption component and an emission component. The model shown in Fig. 4.8 has an emission line at $z = 2.7745$ with F_1 = 300 × 10^{-21}Wm^{-2} , $FWHM_1$ = 700 kms^{-1} and a blue shifted (-590 kms^{-1}) absorption component with v$_{\rm Doppler}$ = 10 kms^{-1} and $N_{\rm HI}$ = 7 × 10^{20} cm^{-2}.

FDF-6063

The profile of FDF-6063 can be modelled with a single absorption component. The absorption shown in Fig. 4.9 has a redshift of $z = 3.4054$ with v$_{\rm Doppler}$ = 10.0 kms^{-1} and $N_{\rm HI}$ = 5 × 10^{20} cm^{-2}.

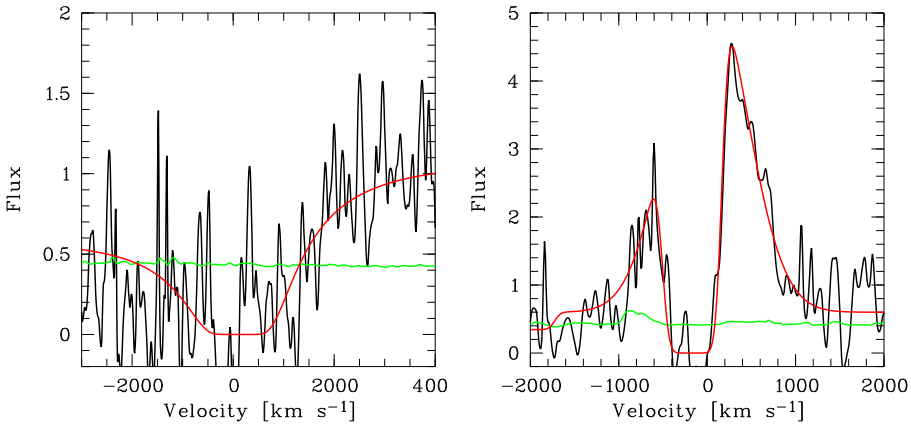

(a) **(b)**

Figure 4.9: Comparison of the observed Lyα (black line) with the theoretical model (red line). The green line indicates the noise level. a) FDF-6063, b) FDF-7539.

FDF-7539

The double-peak profile of FDF-7539 can be modelled with one emission and one absorption component. Additionally a continuum of of 0.6×10^{-21}Wm^{-2} Å^{-1} is assumed. One model is shown in Fig. 4.9. The emission component is at a redshift of $z = 3.29$ with $F_1 = 95.0 \times 10^{-21}$Wm^{-2}, $FWHM_1 = 1000$ kms^{-1} . The absorptions component has a neutral column density in the range of $N_{\rm HI} = 3 \times 10^{17}$ to 6×10^{19} cm^{-2} with a corresponding Doppler width of $v_{\rm Doppler} = 120$ kms^{-1} to $v_{\rm Doppler} = 10$ kms^{-1} .

FDF-7683

The profile of FDF-7683 is noisy, but a clear asymmetry is seen. The profile can either be modelled with two emission components or one emission and one absorption component. The χ^2 is for both configurations sufficiently small. In Fig. 4.10 one emission and one absorption component is displayed. The emission component is at a redshift of $z = 3.7842$ kms^{-1} with a flux of $F_1 = 19 \times 10^{-21}$Wm^{-2}, and a width of $FWHM_1 = 450$ kms^{-1} . The absorption component is blue-shifted by -258 kms^{-1} with $v_{\rm Doppler} = 20$ kms^{-1}and $N_{\rm HI} = 5 \times 10^{17}$ cm^{-2}.

FDF-9002

The profile can be modelled with one emission component. The emission component in Fig. 4.10 has a redshift of $z = 3.375$ kms^{-1} a flux of $F_1 = 11.0 \times 10^{-21}$Wm^{-2} and a width of $FWHM_1 = 470.0$ kms^{-1} .

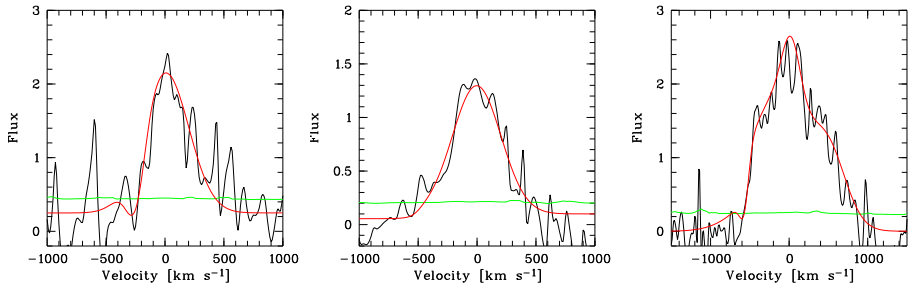

Figure 4.10: Comparison of the observed Lyα (black line) with the theoretical model (red line), green line indicates the noise level. a) FDF-7683, b) FDF-9002, c) FDF-9015

FDF-9015

The model shown in Fig. 4.10 has three emission components and one absorption component. The χ^2 values of models with fewer components were significantly higher as the χ^2 value of the fit with four components.

4.4 Results of the Lyα profile modelling

Lyα profile modelled with Gauss and Voigt components

Gauss emission and Voigt absorption components were used to model the Lyα profiles. Also a continuum were added in some cases. In addition the absorption by the intergalactic medium were considered. The quality of most Lyα profiles of the medium-resolution sample were sufficiently high to be modelled. Only FDF-5744, FDF-6557 and FDF-8304 were heavily affected by atmospheric lines or/and had a too low signal-to-noise ratio. The number of components were kept as low as possible, but most Lyα lines with emission were modelled with more than one component (see Table 4.1).

Table 4.1: Number of Lyα profiles modelled with different number of components

modell	number
total	15
Voigt	1
Gaussian	1
Gaussian + Voigt	4 (+1)
Two Gaussian	1 (+1)
Two Gaussian + Voigt	6
Three Gaussian + Voigt	1

The disadvantage of this technique is the high degeneracy of the parameters. Two gauss emission components and one Voigt absorption component results in eight

free parameters, which can not be constrained from the Lyα profile alone. Nevertheless, some conclusions can be drawn from the modelling using Gauss emission and Voigt absorption.

Five asymmetric profiles were modelled with two Gaussian emission and one Voigt absorption components. As Dawson et al. (2002) already pointed out, a degeneracy between the velocity offset of the two emission components and the line width of the second emission exists. The profile can be modelled with a high velocity offset and a narrow second emission component. The profile can be described by decreasing the velocity offset and increasing the line width of the second emission component, resulting in a model with a narrow and a broad emission component at the same redshift. A parameter which have been constrained is the maximal velocity offset between the secondary emission-peak and the main emission peak. The maximal offset ranges between 280 and 430 kms^{-1} for the galaxies with an asymmetric profile. On the other hand, if both components have the same redshift, the line width of the broad component is large. It ranges from 400 to 2000 kms^{-1}, with an average value of 890 kms^{-1}. The narrow components have line widths from 300 to 360 kms^{-1}.

The neutral column densities are in the range of $N_{\mathrm{HI}} \approx 10^{15}$ to 10^{20} cm^{-2} . But unless the profiles are not double-peaked or the continuum is affected by the absorption, the parameters of the neutral component are not well constrained. However, the sharp cutoff of the blue wing as seen in the asymmetric profiles is likely caused by the Doppler core of the asymmetric profile. This indicates that the neutral column density is for the asymmetric profiles rather low. For the double peaks profiles an upper limit for the neutral column density can be given (FDF-4691: $N_{\mathrm{HI}} \leq 10^{19}$ cm^{-2}; FDF-5215 $\leq 2.5 \times 10^{18}$ cm^{-2};FDF-7539 $\leq 6 \times 10^{19}$ cm^{-2}). For FDF-5550, FDF-5903 and FDF-6063 the neutral components are additionally affecting the continuum and hence the column density N_{HI} is better constrained.

Comparison of the different modelling technics

FDF-4691 and FDF-5215 have been modelled with the finite element calculations and with Gauss emission and Voigt absorption. Both models assume a Gaussian emission component, which is optical thin for Lyα photons. The differences arises because the neutral component acts different on absorbed photons. The absorption component of the finite element calculations re-emits the photons. The re-emitted photons are redistributed in frequency space leading to two peaks. The model with Gauss emission and Voigt absorption assumes that all absorbed photons are not detected. They are either absorbed by dust or they are absorbed by extended neutral clouds, which distribute the photons in physical space and thus have a too low surface brightness to be detected (Kunth et al. 1998).

The amount of neutral hydrogen has the same order of magnitude in both models, if the same turbulence is assumed for the neutral shell. The neutral shell in the finite element calculations not only absorbs, but also redistributes the Lyα photons in frequency space. Emission comes from the redistribution of the absorbed photons. As a consequence the total emission flux needed in the modelling with Gauss emission and Voigt absorption is higher than the total flux used in the finite element calculations. Also differences arises in the number of components needed.

For the profile of FDF-4691 the finite element calculations need two components to model the profile, a neutral shell and a emission component, while the model using Gauss emission and Voigt absorption needs three components. The differences arise also in this case because the neutral shell in the finite element calculations absorbs and re-emits photons.

The emission component

In both models a Gaussian emission component was assumed. This central emission component reflects the velocity dispersion of the emitting gas, if the emitting material is optical thin for Lyα photons. Ionisation-bounded HII regions are optical thin for ionising radiation, but not for Lyα photons (Osterbrock 1989), and the resulting Lyα line profile of a single HII region will be broadened due to resonance scattering. Therefore it is very likely that the derived width of the main emission component is larger than the velocity dispersion of the emitting gas.

We speculate that comparing the widths of Lyα with other non-resonance lines, .e.g., Hα, might give insight whether the width of the Lyα is determined by the velocity dispersion or by resonance scatterings effects in the emitting material. Unfortunately, only a limited number of nearby and high-redshift galaxies have been observed with UV-restrame medium-resolution spectra and additionally with corresponding optical-restframe medium-resolution spectra. For the nearby galaxy Haro 2 (Kunth et al. 1998) the Lyα width is even smaller than the Hα width because absorption blue-wards the Lyα line occurs. For the Lynx arc at a redshift of $z = 3.36$ described in Fosbury et al. (2003) the width of the Lyα is about five times larger as the width of the Hβ line. The physical properties which determine the width of the emission component of the Lyα are not known.

Mass estimates The Lyα emission lines modelled in this work and elsewhere (Dawson et al. 2002; Hu et al. 2004) assume a central Gaussian emission component. If the radius of the galaxy is known, a mass can be estimated by using the virial theorem, assuming that the FWHM of the Lyα emission reflects the velocity dispersion of the emitting gas.

For ten galaxies of the medium resolution sample both the radii and the widths of the Lyα emission profile could be measured. The masses have been estimated from eq. 4.31:

$$M_{\rm virial}[M_\odot] = 1.26 \times 10^{10} {\rm M}_\odot \times \sigma^2[100 {\rm kms}^{-1}] \times {\rm R[kpc]} \qquad (4.31)$$

The resulting masses ranges between $M_{\rm virial} = 1.1 \times 10^9$ M$_\odot$ and $M_{\rm virial} = 1.6 \times 10^{11}$ M$_\odot$, with an average virial mass of $M_{\rm virial} = 6.1 \times 10^{10}$ M$_\odot$. Pettini et al. (2001) analysed the optical rest-frame spectra of high-redshift Lyman-Break galaxies and derived virial masses using [OIII] λ 5007. While the galaxies in Pettini et al. (2001) have larger radii (they assumed $r_{1/2} = 2.3$ kpc), their median $\sigma = 70$ kms^{-1} translates into a virial mass of $M_{\rm virial} = 1.3 \times 10^{10}$ M$_\odot$. The virial masses of the Lyα emission galaxies are about a factor 5 times higher than the masses of the galaxies in Pettini et al. (2001). As described above, resonance scattering occurs also in the emitting gas. This may explain the larger masses of the galaxies in this sample.

Absorption by neutral hydrogen

Many Lyα profiles show an asymmetric profile, in the sense that the blue side drops sharply and a red extended wing is seen. Lequeux et al. (1995) and Kunth et al. (1998) observed asymmetric Lyα profiles of nearby star-forming galaxies. They modelled the profiles with a Gauss emission component and a blue-shifted Voigt absorption component and argued that the profiles arise from a galactic outflow of the interstellar medium. They found no secondary peaks, redshifted with respect to the primary peak. In the high-redshift universe the situation is more complex. Ajiki et al. (2002) found a possible superwind galaxy at a redshift of $z = 5.69$ and modelled the line profile with one Gauss emission and Voigt absorption. They attributed the absorption component to a superwind. Hu et al. (2004) observed 19 LAEs at a redshift of $z \approx 5.7$, they modelled the composite profile also with a Gauss emission and a Voigt absorption, but attributed the absorption profile to the intergalactic medium.

Indeed the amount of information that can be derived from the blue wing of the profile is limited, because the neutral hydrogen of the intergalactic medium absorbs the light of the galaxy blue-wards the Lyα line. The hydrogen clouds between us and the emitting galaxy along the line of sight are situated at different redshifts and cause in addition metal absorption lines, Lyman continuum absorption and strong Lyα absorption lines. The absorption components in the line profiles can be attributed to neutral hydrogen in the galaxy itself or in the intergalactic medium, leading to ambiguities. If the absorption is caused by the IGM, the apparent blue-shift results from the expansion of the universe and the corresponding clouds have distances of several Mpc from the galaxy. There is no physical relation between the clouds and the galaxy. The photons are absorbed by the cloud and even if all of the photons are re-emitted, the flux would be far too low to be detected.

For the galaxies in the FDF at a redshift of $z \approx 3$ the influence of the IGM can be estimated by using the results of Frank et al. (2003). Frank et al. (2003) analysed the high-resolution spectra of the QSO Q0103-206 in the FDF and derived several properties of the Lyα forest, including the column density distribution function. The CDDF measures the number of absorption lines per unit column density and per unit absorption path as a function of N_{HII}. The CDDF is defined as

$$f(N_{HI})dNdX = \frac{n}{\Delta N \Delta X(z)} dNdX \tag{4.32}$$

It follows a single power-law distribution and is parameterised as

$$f(N_{HI}) = A \times N_{HI}^{-\beta}, \tag{4.33}$$

where n is the number of lines in the column density bin (N,N+δN) and per absorption distance bin (X(z), X(z) + δX(z)). X(z) depends on the cosmology.

Using the best-fit parameters ($A = 7.1 \times 10^9$, $\beta = 1.62$) for the FDF, based on HI absorption systems from z = 2.729 to z = 3.245 in the high-resolution spectrum of QSO Q0103-206 (Frank et al. 2003), the number of HI clouds in the vicinity of the LAEs is estimated:

$$n = \int \int f(N_{HI})dNdX \tag{4.34}$$

If $N_{HI} > 10^{16}$ cm^{-2}, the number of Lyα absorption line systems n in the interval δv blue-wards the Lyα line is $n = 0.07\ \frac{\Delta v}{1000 km/s}$. For $N_{HI} > 10^{19}$ cm^{-2} the number of Lyα absorption line systems is $n = 9 \times 10^{-5}\ \frac{\Delta v}{1000 km/s}$. The probability for finding a cloud of the IGM causing a strong Lyα absorption in the vicinity of the Lyα is rather low. We conclude that most of the absorption lines of the $z \approx 3$ galaxies are intrinsic absorption lines originating in the galaxies itself.

The neutral shell

A neutral, homogeneous shell was assumed in the finite element modelling of the Lyα profiles. Using the derived parameters of finite element models of FDF-4691 and FDF-5215 densities of $n_{HI} = 10^{-3}$ cm^{-3} and $n_{HI} = 10^{-6}$ cm^{-3} are derived. Moreover a high turbulence is derived for both shells (FDF-4691 and FDF-5215). A rate of ionisating photons of 10^{54} 1/s is estimated, which escape the emission region, if the emission region is optical thin for ionisating photons. The high turbulence, the low density, and the (probably) high flux of ionisating photons makes is plausible, that the shell is ionised and is in a recombination equilibrium. The Lyα flux caused by recombination in the shell would be two orders of magnitude lower than the Lyα flux from the core of FDF-4691 or FDF-5215. Also if the neutral shell is clumpy, the total neutral column density is higher, because the observations are biased against the line-of-sight with the lowest neutral column densities.

The modelling of the Lyα lines described in this section resulted in rather small neutral hydrogen column density for the medium-resolution sample. The galaxies in the medium-resolution sample with $EW_{Ly\alpha} < 20$ Å have an average neutral column density of 2×10^{20} cm^{-2}, while galaxies with higher Lyα equivalent widths ($EW_{Ly\alpha} > 20$ Å) have 5×10^{17} cm^{-2}. For FDF-4691 and FDF-5215 it was argued that the shell is indeed ionised and in recombination equilibrium. In addition Venemans et al. (2005) found low-column densities for their Lyα emission galaxies, ranging from $N_{HI} = 10^{13}$ to 10^{16} cm^{-2} . Kunth et al. (1998) modelled their sample of nearby galaxies with neutral column densities ranging from 5×10^{19} to 3×10^{21} cm^{-2}. They found that galaxies with no Lyα emission have also higher hydrogen neutral column densities. These are indications that the Lyα emission galaxies have a low neutral hydrogen column density.

In the superbubble model of Mas-Hesse et al. (2003) the detection of Lyα emission is explained as follows: in later stages of the evolution of the suberbubble, the ionising radiation can escape the supershell, ionise the surrounding HI halo and reduce the optical opacity. But not only the optical path decreases, also the escape mechanism changes. The photons do not escape anymore by a single longest excursion, but by a single longest flight. The spatial diffusion is lower and the surface brightness is increased, allowing a better detection of the Lyα photons. In this picture, LAEs are galaxies where a starburst has ionised the neutral hydrogen along the line of sight. Since the HII region in the model of Mas-Hesse et al. (2003) has a conical structure, the detection of the Lyα emission depends on the viewing angle. Galaxies with strong or weak Lyα emission are essential the same galaxies, only viewed from a different angle.

If the hydrogen in the line of sight shows a high degree of ionisation, it is likely that the galaxy is optically thin for hydrogen ionising photons. The escape frac-

tion of hydrogen ionising photons can be observed with, e.g., narrow-band images (Inoue et al. 2005), and the escape fraction from LAEs can be compared with the escape fraction from LBGs. If the low-column density of the neutral hydrogen is caused by a high degree of ionisation of the surrounding hydrogen, Lyα emission line galaxies will show a higher flux of hydrogen ionisating photons as Lyman-break galaxies. To investigate this issue two composite spectra derived from low-resolution spectra of the FDF spectroscopic survey are constructed. One consists of galaxies with strong Lyα emission and one consists of galaxies with weak or no Lyα emission. The wavelength range from $z = 3$ to 4 is selected. Unfortunately, the number of galaxies in the sample with strong Lyα emission is too low and the mean error of the ionisation flux is too large to derive useful constraints. Steidel et al. (2001) analysed a composite spectrum of 29 galaxies at a redshift of $z = 3.1$ and found a significant Lyman-continuum flux. The galaxies of Steidel et al. (2001) are blue galaxies with a strong Lyα flux. Other searches for Lyman-continuum flux in high-redshift galaxies were not successful (Inoue et al. 2005).

The secondary emission peak

In seven Lyα profiles of this sample, a second peak, red-shifted with respect to the main peak, is observed (see Table 4.1). In some LAEs at high-redshift this second peak is observed (Djorgovski et al. 1996; Franx et al. 1997; Dawson et al. 2002; Westra et al. 2004) but not all studies detect it (Hu et al. 2004). In Djorgovski et al. (1996) the red wing of the Lyα emission line of DLA2233+131 is interpreted as emission from rotating disks, while Franx et al. (1997) analysed a pair of lensed galaxies and found evidence for a galactic outflow. Dawson et al. (2004) introduced the idea that the redshifted peak originates from a receding shell. The model shown in Fig. 4.2.2 illustrates this concept. A starburst ionises the central region and the superwind accerelates a neutral shell. The Lyα photons are absorbed by the approaching shell, hence leading to blue-shifted absorption components. Lyα photons can escape from the central emission and cause a central emission component, if the shell has a sufficient velocity offset. Also Lyα is backscattered from the receding shell.

Dawson et al. (2002) observed a Lyα emission galaxy at a redshift of $z = 5.190$ with $F_{\mathrm{Ly}\alpha} = 30 \times 10^{-21}$ $10^{-21}\mathrm{Wm}^{-2}$ and $EW_{\mathrm{Ly}\alpha} = 120 \pm 40$ Å. Dawson et al. (2002) modelled the profile with three components, including a narrow (280 kms^{-1}) central Gaussian emission and a broad (560 kms^{-1}) by 320 kms^{-1} redshifted component.

The model of an expanding shell surrounding an emission region describes the asymmetric line profiles. The model of a expanding shell is also used for the finite element computations. Here the red wing in the Lyα profiles is caused by the intrinsic broad emission component and not by a receding shell. The differences arise because the finite element method could not reach sufficient optical depths.

Ahn et al. (2003) and Ahn (2004) could reach higher optical depths using Monte-Carlo simulations. They showed that a receding neutral shell in spherical symmetric model is indeed producing a secondary peak. Ahn et al. (2003) showed that the Lyα photons escape the system by multiple backscatterings, which leads to a series of emission peaks red-ward of the systematic redshift. They concluded that

the velocity differences between the peaks and widths of the peaks give information about the kinematics of the outflow. Ahn (2004) showed that multiple peaks are suppressed when dust is distributed inside the ionised bubble and inside the neutral shell itself.

Because the photons are coherently scattered in the atoms restframe, a moving mirror effect occurs. The mirror sees already redshifted photons, which are reflected with an additionally frequency shift. The photons from the receding shell will have a frequency shift of twice the shift of the receding shell. Ahn et al. (2003) showed that the center of the redshifted peak is at the velocity of the receeding shell. The peaks of the second Lyα emission lines of the medium-resolution sample are in the range of 280 and 430 kms^{-1}, leading to typical shell outflow velocities of 280 and 430 kms^{-1}. Since the second Lyα emission line can fitted with a broader, but less redshifted peak, the derived shell velocities are only an upper limit.

While a high ambiguity exist, the model of an expanding shell surrounding a emission region can successfully describe the majority of the Lyα profiles. Since also the interstellar absorption lines are blue-shifted (see Sec. 3.3), the evidence for outflow is strong. Most of the 18 galaxies with observed Lyα profile in the FDF show outflow, indicated either by the line profile or/and the blue-shifted interstellar absorption lines. Only FDF-9002 shows no indication for an outflow, but here is the starburst interpretation not clear.

The superbubble model

As discussed in Sec. 4.4 there is evidence for an expanding shell. Since the expanding shell is likely driven by starburst activity, the model of a superbubble might describe the expanding shell.

The superbubble model describes an expanding bubble, driven by the energy of a starburst. The kinetic energy of supernovae is thermalized and forms a hot gas. The pressure of the hot gas drives the expansion of a superbubble. Ambient interstellar gas is shocked and accelerated. The bubble expands towards the density gradient into lower density material, hence in a disk-like geometry along the disk minor axis. After the shell has been formed and is expanding, in the shell Rayleigh-Taylor instability occurs and the shell begins to fragment. The wind can enter the free wind phase or sweep up material again. The superwinds are a source of energy and metals for the Intra Cluster Medium (ICM) of galaxy clusters and the Intergalactic Medium (IGM). The phenomena of superwinds and the superbubbles is well studied in the local universe (Heckman et al. 1990, 1993), some examples for superwinds are M82 or Arp 220.

Pettini et al. (2000); Shapley et al. (2003) suggest that the outflow observed in high-redshift galaxies is caused by a superwind generated by the starburst in the galaxy. To test the possibity that the LAEs are showing a superwind, we model the galaxies assuming a simple model. We assume a simple spherical symmetric model. A starburst is initiated in ambient medium of constant density. The expansion of a thin, radiative cooling shell of swept-up material can be described with the following parameters (Heckman et al. 1993):

$$r_{\rm shell} = 5 L_{\rm Bol}^{1/5} n_o^{-1/5} t^{3/5} {\rm kpc} \tag{4.35}$$

$$v_{\rm shell} = 100 L_{\rm Bol}^{1/5} n_o^{-1/5} t^{-2/5} {\rm kms}^{-1} \quad (4.36)$$

Here $L_{\rm Bol}$ is the bolometric luminosity in units of 10^{11} $L_\odot$, t is the age in units of 10^{15} s (≈ 32 Myr), n_0 is the density of the ambient medium in units of cm^{-3}. In the above equations the kinetic energy has been converted into bolometric luminosity using scaled models of M82 (Heckman et al. 1993). The bolometric luminosities are estimated from the spectral UV-luminosities by using $log(L) = log(L_{\rm UV}) + 3.2$ following Noll et al. (2004). The spectral UV-luminosities are corrected from dust attenuation using the slope of the continuum (Noll et al. 2004). Eq. 4.35 and 4.36 are scaled versions of the solutions found by Castor et al. (1975), which describes the so-called snowplow phase of swept-up material caused by stellar wind interacting with the interstellar medium.

FDF-4691 is, when it is indeed a starburst, one the youngest starbursts in the sample, FDF-5215 is somewhat older starburst and FDF-5550 has been modelled with even older starbursts (see Sec. 3.3.2). FDF-4691 shows only a weak outflow, FDF-5215 shows a stronger outflow and FDF-5550 an even stronger outflow. This is qualitative in agreement with an expanding superbubble. But the simple model described by eqs. 4.35 and 4.36 are not in agremeent with the observations. If a density of $n_0 = 1$ cm^{-3} and an age of 3 Myrs are assumed for FDF-4691 the radius of the neutral shell will be at $r_{\rm shell} = 1.1$ kpc and having a velocity $v_{\rm shell} = 240$ kms^{-1} . While the radius of the neutral shell is consistent with the observations (the 5300 Å narrow-band image, which wavelength range covers the Lyα line, has not a sufficient resolution to exclude this radius), the velocity of $v_{\rm shell} = 250$ kms^{-1} is much too high. For FDF-5215 a radius of $r = 10$ kpc and a velocity of 100 kms^{-1} is derived, assuming a age of 60 Myrs. The observed radius of $r = 0.7$ kpc is only reached, if a much higher density of $n_0 = 5 \times 10^5$ cm^{-3} which is not reasonable, is assumed. Also the velocity is much smaller as observed. Hence this model does not well describe the observed properties of FDF-4691 and FDF-5215.

A more sophisticated model for an expanding superbubble was developed by Tenorio-Tagle et al. (1999). They computed the evolution of a superbubble caused by a starburst in a disk-like structure. They showed that the different phases of the superbubble will lead to certain Lyα profiles. In the first phase the starburst generates a supershell embedded into a neutral halo. Since the colum density of the neutral Halo is very high, no Lyα emission is seen. The shell accelerates and drives into the low-density HI halo. The shell becomes Rayleigh-Taylor unstable and breaks up. The hot gas inside the shell can escape and the UV-radiation ionise a conical HII region, which reaches the outskirts of the galaxy. A second ionised shell with a expansion velocity of several hundred kms^{-1} will form later. A strong Lyα emission is seen, if the starburst is seen through the ionised region. The expanding ionised shell will begin to recombine in the next phase, leading to a secondary Lyα emission and an absorption by the neutral component of the shell. After a while the ionisation front has become trapped inside the shell and slowed down its expansion. Lyα is seen in absorption with a small blue shift.

In this model FDF-4691 would corresponds to the phase, when the first shell has just become unstable and the HI halo is almost ionised. The observed absorption component of FDF-4691 comes from the neutral fraction of the highly ionised halo.

The other galaxies would be observed in the phase, where the second shell begins to recombine, forming a neutral absorption component, blue-shifted by several 100 kms^{-1} in respect to the central starburst region. FDF-5550 is in the phase where the second shell recombines and becomes neutral.

The Lyα double peak profiles

FDF-4691, FDF-5215, and FDF-7539 show double peak profiles. Complex Lyα profiles, like double peak profiles, are known from radio galaxies (van Ojik et al. 1997), but in starburst galaxies only asymmetric single lines were widely known. In some observations a double peak profile was observed, but the profiles were modelled with a Gaussian emission(s) and Voigt absorption(s) and not attributed to a frequency redistribution of the Lyα photons. In the nearby galaxy IRAS 08339+6517 a secondary blue peak is observed in a UV-HST spectrum (Kunth et al. 1998). Fosbury et al. (2003) observed a gravitational arc at the cluster RXJ0848+4456. The Lynx arc, which is magnified by a factor of 10, has a redshift of 3.357 and shows strong, narrow emission lines. A double peak profile of Lyα and of CIV is seen. Christensen et al. (2004) observed an extended Lyα emission nebula at the $z = 3.295$ DLA galaxy in Q2233+31. The integral field spectroscopy shows a double peaked profile of the Lyα line. Venemans et al. (2005) observed also several galaxies with a double peak profile at the redshift of $z \approx 3.13$. They modelled the profiles with Gauss emission and Voigt absorption.

Meinköhn & Richling (2002) and Ahn et al. (2003) modelled Lyα with an expanding neutral shell using radiative transfer technics. The profiles have the characteristic double peak profile, but the flux of the blue peak is decreasing, if the expansion velocity is increasing. Only galaxies with a rather static envelope have double peak profile. Up to now not many galaxies with a double peak profile have been observed. But double peak profiles are only observed if the signal-to-noise ratio and the spectral resolution is sufficient high. Only in the high-redshift regime ($z > 5$) up to now many Lyα lines have been observed with high signal-to-noise and sufficient spectral resolution. The intergalactic medium affects the blue part of the Lyα profiles, not the red part. Even if a significant number of the high-redshift galaxies show double peak profiles, the blue part of the Lyα is absorbed by the intergalactic medium. Only one asymmetric line is observed. This may explain that all double-peak Lyα profiles have been observed at a redshift of $z \approx 3$.

Limitation of the models

The Lyα profiles were modelled either with finite element computation or with a combination of Gauss emission and Voigt absorption. While the finite element computation is more sophisticated as the combination of Gauss emission and Voigt absorption, the finite elements calculations also simplifies the problems. Only complete redistribution and a Doppler profile is used for solving the radiative transfer calculations. Partial redistribution and the Voigt profile has to be included for larger optical depths ($\tau_0 > 10^4$). The effects at smaller optical depths are likely not very important. The technique of combination of Gauss emission and with Voigt emission neglects the redistribution of absorbed photons.

For the model of the finite element computation a spherical symmetric neutral shell was assumed around a core, which emitted Lyα photons. The model with the combination of Gauss emission and with Voigt emission could be explained qualitativly also by a spherical expanding symetric shell around a emitting core. Since the Lyα profiles were fitted successfully, the model of neutral shell around a emitting core might describe the Lyα emission galaxies. But this model might oversimplify the high-redshift galaxies.

It was assumed that the central emission region shows a Gaussian emission profile. If the central emission component is not optical thin for Lyα photons, the emission component might also be a double peak or an even more complicated profile. A further assumption of the model is that the shell is homogenous. This is unlikely, given the complicated hydrodynamics. Rayleigh-taylor instabilities will lead to knots and denser regions. Pettini et al. (2000) analysed the spectrum of MS1512cb-58 and reported that the absorption lines of the different species have different mean velocities and line widths. This suggests that the galactic scale outflow of the ISM is inhomogeneous and that the assumption of an homogenous outflow is not valid. But the detailed physics of the outflow can only be computed, when a sufficient number of parameters are known, e.g. the density profile of the surrounding gas. A further assumption is that the model is spherical symmetric. If the galaxies are the bulges of today's galaxies or the elliptical galaxies, spherical asymmetry might be a good approximation. The HST/ACS images show, that not all galaxies show a spherical symmetry. Indeed, merger events or a disk-like structure would lead a aspherical distribution of the gas and stars.

It is necessary to expand the spherical symmetric model and to model the starburst in detail. The radiative transfer of the Lyα photons and the hydrodynamics of the ISM and the physics of the starburst have to be computed in a self-consistent way. But this would lead to an increase of the free parameters,e.g. the density of the surrounding neutral halo. The Lyα profiles alone would not give enough information to constrain the parameters of such a sophisticated model.

Chapter 5

Correlations

5.1 Parameters affecting the interstellar absorption lines

Shapley et al. (2003) and Noll et al. (2004) showed that the equivalent width of the interstellar absorption lines $EW_{\rm LIS}$ in composite spectra correlates with the slope of the continuum and the strength of the Lyα emission. Since the strongest low-ionisation lines are saturated (Shapley et al. 2003), the dependence of the equivalent width $EW_{\rm LIS}$ on the other properties cannot be explained by metalicity abundance, but by geometrical or kinematic effects. The equivalent width of saturated lines changes for a different covering fraction or a different velocity dispersion of the blue-shifted clouds, or both. The fraction of the stellar continuum, which is not affected by the interstellar clouds, is given by the covering fraction. Since Shapley et al. (2003) and Noll et al. (2004) used only low-resolution spectra, the two effects, covering fraction and velocity dispersion, could not be distinguished. In Fig. 5.1 the equivalent width of the interstellar absorption lines is plotted as a function of the the mean line width of the interstellar absorption lines. Note that the only the strongest interstellar absorption lines SiII λ1260 and CII λ1335 are included. SiII/OI λ1303 was excluded, because the line widths of the blended two lines could not be distinguished. In addition further two galaxies are included (FDF-3312 and FDF-3810, see Table A.5). A correlation is intended in Fig. 5.1. A linear regression gives a slope of $m = 4.6\ (\pm\ 1.4)\ 10^{-3}$ and $b = 0.04 \pm 0.6$, where m and b are defined by $y = mx + b$. The scattering is large and indicates that the covering fraction play also a role. However the correlation shows that the velocity dispersion is the major factor that dominates the equivalent width of the interstellar absorption lines.

If the equivalent width of the low-ionisation interstellar absorption lines is complete determined by the line width, the covering fraction is rather constant for the galaxies of the medium-resolution sample. Shapley et al. (2003) and Noll et al. (2004) showed that the equivalent width of the interstellar absorption lines anti-correlates with the Lyα equivalent width. If the equivalent width of the interstellar absorption lines is determined by the velocity dispersion of the outflowing material, the Lyα equivalent width anti-correlates with the velocity dispersion of the outflowing gas.

Using Voigt absorption profiles, the interstellar absorption line profiles were mod-

elled with different column densities and velocity dispersions. From the neutral column density of the hydrogen the column densities of SiIIλ1260 and CIIλ1335 can be derived, assuming solar abundances. Only for column densities, which exceed the values expected from solar abundance by several orders of magnitude, the large line width is entirely caused by the large abundances. The velocity dispersion is indeed the parameter, which determines the strength of the absorption lines, unless the metalicity is extremely large.

Only for seven galaxies of the medium-resolution sample (and further two galaxies) the $EW_{\rm LIS}$ and $FWHM_{\rm LIS}$ can be measured. These nine galaxies have a much lower average Lyα equivalent width ($EW_{{\rm Ly}\alpha}$ = 3.5 Å) as the complete medium-resolution sample ($EW_{{\rm Ly}\alpha}$ = 53 Å). Galaxies with stronger Lyα emission have a weaker UV-continuum and hence their absorption lines strengths are more difficult to derive. It remains unclear, whether the correlation found above is still valid for galaxies with much stronger Lyα emission.

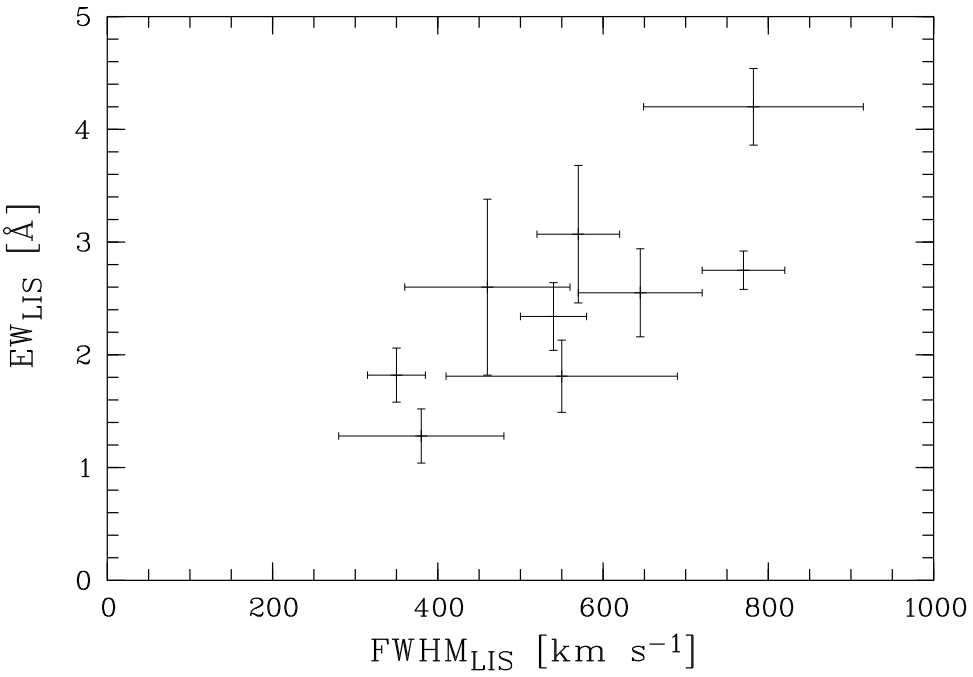

Figure 5.1: The equivalent width of the interstellar absorption lines is plotted as a function of the line width of the interstellar absorption lines

5.2 Parameters affecting the Lyα equivalent width

5.2.1 Slope of the UV-continuum

Since the slope of the continuum β is a good tracer of the attenuation (see Sec. 3.1.2), $EW_{{\rm Ly}\alpha}$ vs. β should correlate. In Fig. 5.2 the continuum slope β is plotted as a function of the Lyα equivalent width. Note that we analysed single galaxies, not composite spectra as in Noll et al. (2004) and Shapley et al. (2003). The

Lyα equivalent width is not independent of the slope of the continuum, but a linear correlation is not seen. Lyα Galaxies with a continuum slope of β > -2, have $EW_{\mathrm{Ly}\alpha}$ below 50 Å while galaxies with a blue continuum β < -2 have Lyα equivalent width in the range of $EW_{\mathrm{Ly}\alpha}$ = -20 to 100 Å . The only exception is FDF-4752, which has a high equivalent width of $EW_{\mathrm{Ly}\alpha}$ = 150 Å and a red continuum. FDF-4752 is one of the Lyα emission galaxies in the vicinity of the QSO (FDF-4683).

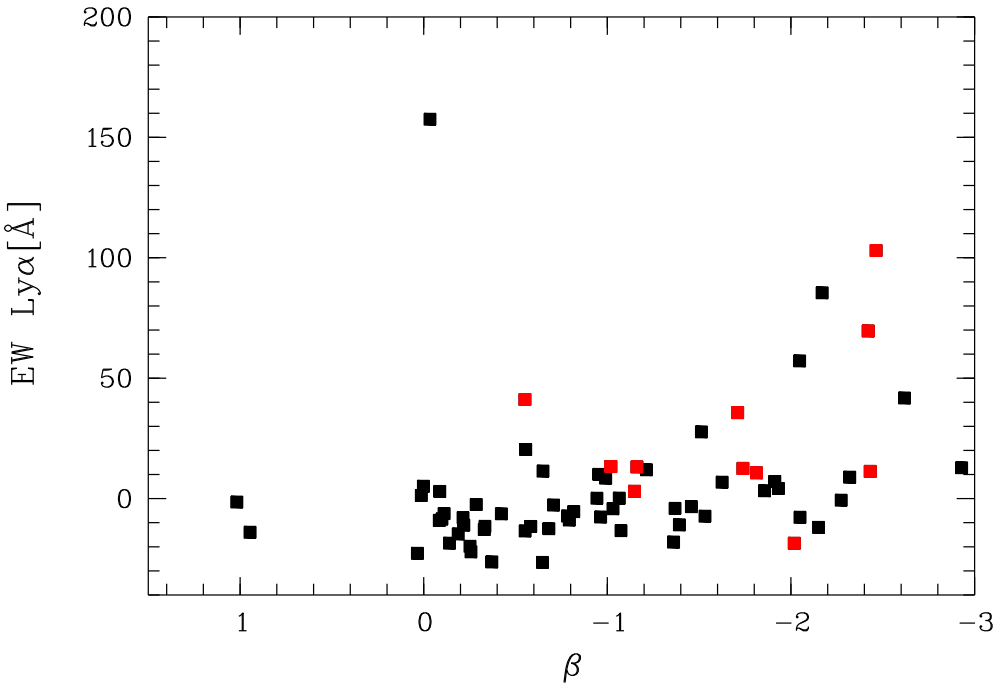

Figure 5.2: The $EW_{\mathrm{Ly}\alpha}$vs. the continuum slope β for the FDF spectroscopic sample (black squares). Red squares indicates the galaxies with the Lyα line observed with the medium-resolution spectra.

Fig. 5.2 shows that galaxies with strong Lyα line are bluer than galaxies with weak or no apparent Lyα emission. Assuming the same age and metalicities for all galaxies a steeper slope is caused by less dust attenuation. There are two possible explanations for the low dust content. The galaxies are so young that the amount of produced dust is very low. Dust is produced in the later phases of stellar evolution. Moreover the dust grains could be destroyed in the violent conditions of the young starburst. The hard UV-radiation field could evaporate the dust grains. Dust grains are further destroyed by shocks due to sputtering, sublimation and grain-grain collisions. (Draine & Salpeter 1979) concluded that only high velocity shocks (v = 300 kms^{-1}) can destroy dust grains. These velocities are likely reached in the emission region of FDF-4691.

The observational results are not clear: Noll et al. (2004) find a correlation from z ≈ 2 to 3, while galaxies from z ≈ 3 to 4 show only a weak correlation. Shapley et al. (2003) find a strong correlation for high-redshift LBG galaxies. Giavalisco et al. (1996) find only a weak correlation of $EW_{\mathrm{Ly}\alpha}$ with β for local starburst

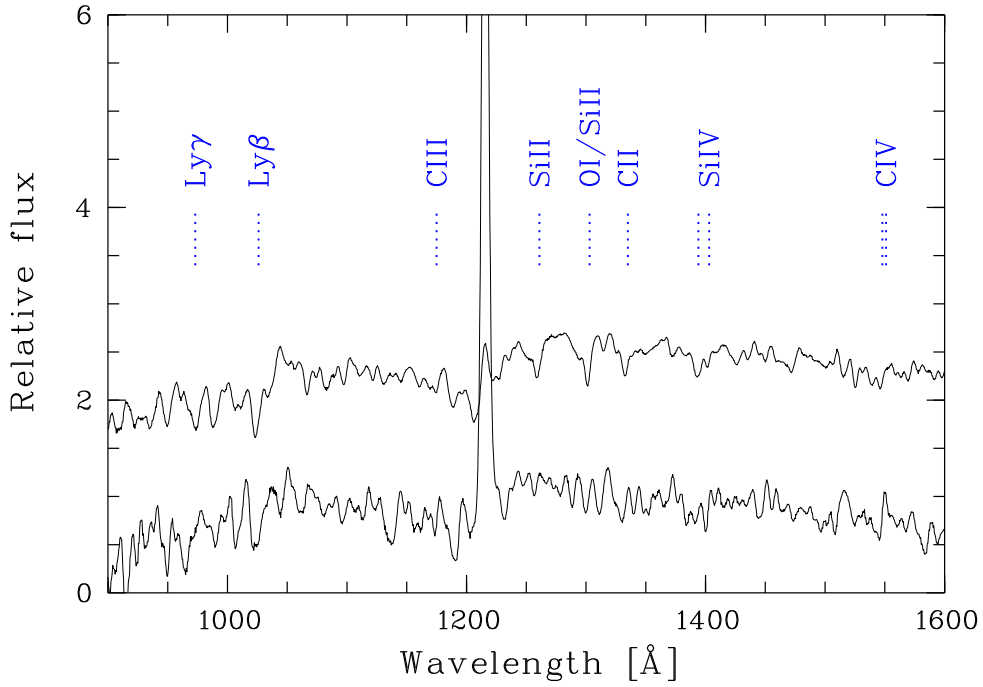

Figure 5.3: A composite spectra constructed from galaxies with a blue slope ($\beta < -2$). Upper spectrum: galaxies with low Lyα emission equivalent width ($EW_{\mathrm{Ly}\alpha} < 20$ Å) . Lower spectrum galaxies with high Lyα equivalent width ($EW_{\mathrm{Ly}\alpha} > 20$ Å).

galaxies. They reanalysed 20 IUE spectra and HST spectra of nearby galaxies. In this study the galaxies of Noll et al. (2004) are used, hence the same trends as reported by Noll et al. (2004) are seen in the medium-resolution sample.

Many galaxies in the FDF spectroscopic sample with a blue continuum do not show a strong Lyα emission (Fig. 5.2). The total amount of dust is not the only parameter, which determines the detection of the Lyα emission. To find further parameters, which determine the strength of the Lyα emission, composite spectra were constructed from low-resolution spectra. Composite spectra were constructed with galaxies with a slope of $\beta < -2$ and low Lyα equivalent width ($EW_{\mathrm{Ly}\alpha} < 20$ Å) and with high equivalent width ($EW_{\mathrm{Ly}\alpha} > 20$ Å). The two composite spectra are shown in Fig. 5.3. While the slope of the continuum is the same in the composite spectra, the low-ionisation interstellar absorption lines are stronger in the spectra with low Lyα equivalent width.

5.2.2 Width of the Lyα line

If the emission component of the Lyα line has a large width, caused, e.g., by a high turbulence of the emitting material, the escape probability of photons and thus the probability of detection the emission is increased. The Lyα photons are distributed over a broader wavelength range. In the case of FDF-4691 a significant fraction of the emitting photons is not affected by the neutral shell (Tapken et al. 2004). The shifted Lyα photons are not resonance scattered by the neutral cloud and thus

their optical path is not increased. These photons and the UV-continuum photons are affected by the same amount of dust. Also Lyα photons which are emitted red-wards with respect to the system redshift are less affected by absorption of the intergalactic medium. The shift of the Lyα photons for the low-opacity cases is proportional to the velocity dispersion of the emitting material (see Sec. 4.1). Fig. 5.4 shows the $EW_{\mathrm{Ly}\alpha}$as a function of the line width of the emission line. But the values of the line width show only a possible anti-correlation with the Lyα equivalent widths. The galaxies with strong Lyα emission and high line width are FDF-4691 and FDF-9015. In addition FDF-7537 shows a strong line width, but as FDF-4691 the Lyα line has a double peak profile.

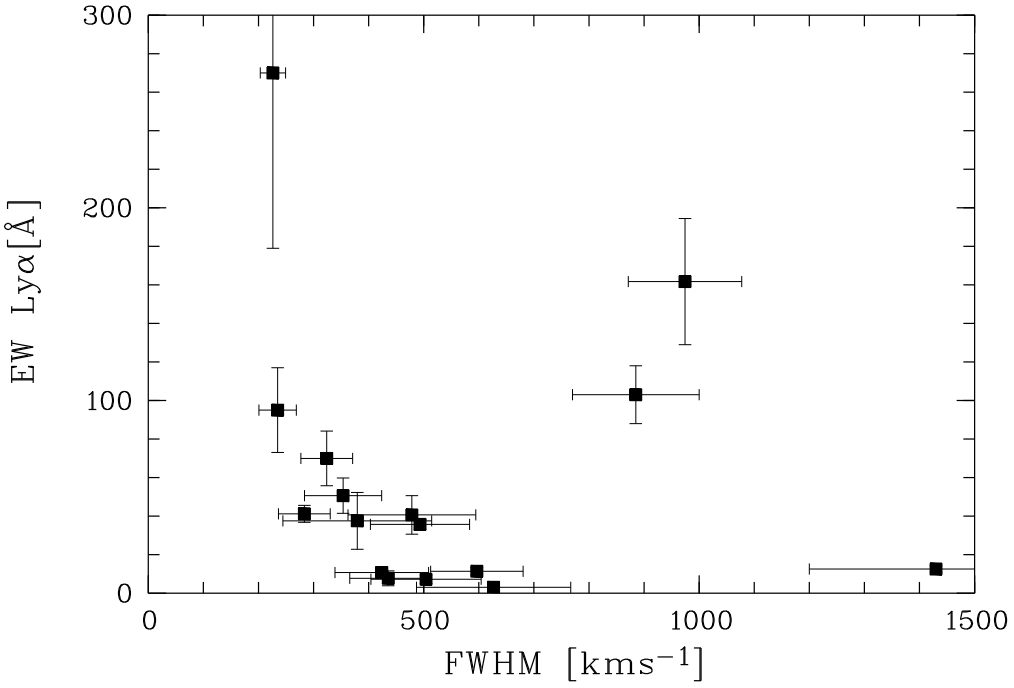

Figure 5.4: The Lyα emission line equivalent width as function of the Lyα emission line width.

To analyse the dependence of the equivalent width of the Lyα line on its line width, the galaxies with $EW_{\mathrm{Ly}\alpha} > 100$ Å and with double peak profiles were excluded. A linear regression gives m = -0.29 ($\pm$ 0.07) and b = 140 $\pm$ 10, where m and b are defined by $y = mx + b$. For galaxies with moderate Lyα equivalent width and a single line profile in the medium-resolution sample, the Lyα equivalent strength decreases with the width of the line. Fig. 5.4 may be showing two distinct populations of Lyα emitters. The larger line widths may be caused by AGN activity, where the anti-correlation between the equivalent width and the line width of Lyα may be found only in starburst galaxies.

5.2.3 Radii of the galaxies

In Fig. 5.5(a) the Lyα equivalent widths of the medium-resolution sample are plotted as a function of the half-light radii. In Fig. 5.5(b) the Lyα equivalent widths are plotted as a function of the half-light radii of the FDF spectroscopic sample. The half-light radii are taken from Pannella et al. (2005). The stronger the Lyα equivalent width the smaller the radii. This is in agreement with the results of Venemans et al. (2005), who found that their Lyα emission line galaxies are on average smaller than Lyman-break galaxies. Venemans et al. (2005) searched for Lyα emission line galaxies around the radio-galaxy MRC 0316-257 at a redshift of $z = 3.13$. The resolved galaxies in Venemans et al. (2005) have an average radius of 0.9 kpc. Four galaxies in their sample are not resolved, thus the mean value is likely lower. The galaxies of the medium-resolution sample have also an average radius of 0.9 kpc. As Venemans et al. (2005) pointed out, Lyman-break galaxies at a redshift of $z \approx 3$ have an average radius of $r \approx 2.3$ kpc (Ferguson et al. 2004).

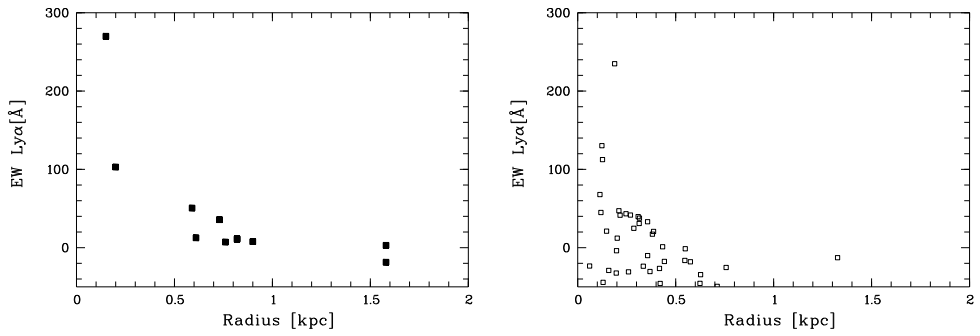

Figure 5.5: (a) The Lyα equivalent widths are plotted as a function of the half-light radii measured in rest-frame UV of the galaxies (medium-resolution sample). (b) The Lyα equivalent widths are plotted as a function of the half-light radii of the FDF spectroscopic survey (radii taken from Pannella et al. 2005).

5.2.4 Outflow velocities

In Sec. 4.4 the velocity of the outflow of the ISM was estimated from the velocity offset between the two emission components. In addition the blue-shifted interstellar absorption lines were used to estimate the outflow velocity. The velocity of outflows derived from the redshifted peaks only place an upper limit on the velocity. In Fig. 5.6 the Lyα equivalent widths are plotted as a function of the velocity of the outflow. Except for FDF-4691, the galaxies with smaller outflow velocities (< 150 kms^{-1}) have Lyα equivalent widths of $EW_{\mathrm{Ly}\alpha} < 50$ Å, and galaxies with higher velocities (> 280 kms^{-1}) distribute on a wider range of Lyα equivalent widths. The range of Lyα equivalent widths is larger for higher outflow velocities. The average Lyα equivalent width is $EW_{\mathrm{Ly}\alpha} = 33$ Å for galaxies with a outflow velocity $v < 260$ kms^{-1} and $EW_{\mathrm{Ly}\alpha} = 80$ Å for galaxies with $v > 260$ kms^{-1} .

This is in accordance with the results of Kunth et al. (1998). Kunth et al. (1998) analysed the UV-restframe spectra of eight nearby galaxies. Four galaxies showed Lyα emission (with $EW_{\mathrm{Ly}\alpha}$ ranging between 13 and 37 Å), while the other four showed no Lyα emission. The four galaxies showing Lyα in emission have HI absorption lines at the blue side of the Lyα line and additionally interstellar absorption lines, blue-shifted with respect to the system redshift (-58 to -227 kms^{-1}). The four other galaxies, which show no emission, have interstellar absorption lines at the system redshifts of the galaxies (+40 to -32 kms^{-1}). Since the Lyα emission in their sample show no correlation with the metalicity, e.g. the galaxy with the lowest well determined metalicity known, they concluded that the Lyα emission detectability is depending on the kinematics of the neutral gas. If the gas shows an outflow the Lyα photons are not absorbed by the blue-shifted gas.

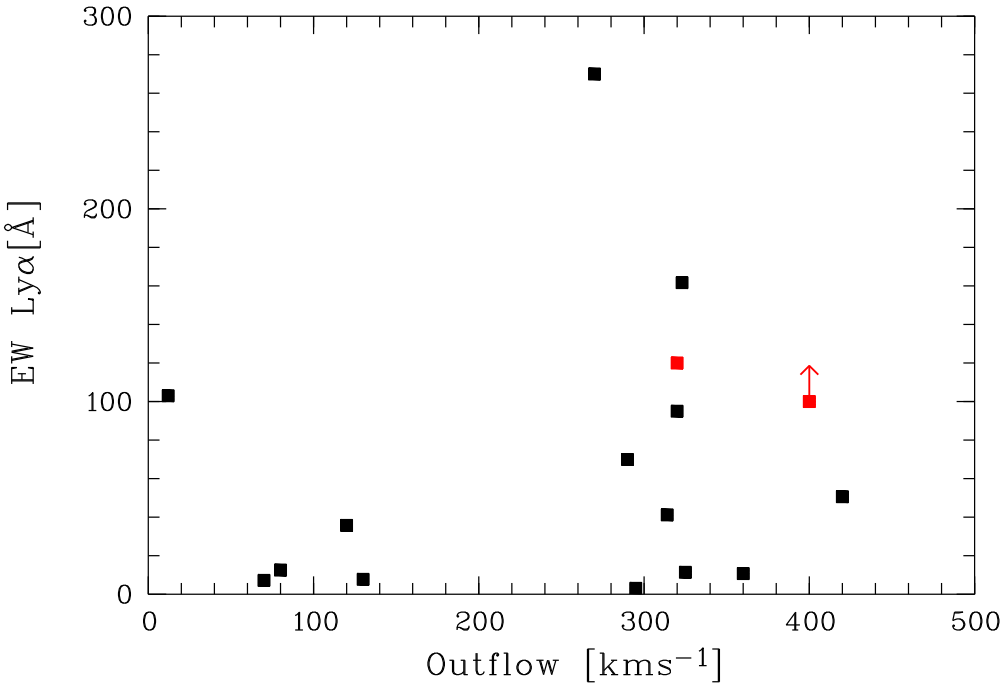

Figure 5.6: The Lyα equivalent width is plotted as function of the velocity of the outflow. The red dots are from Dawson et al. (2004) and Westra et al. (2004).

5.2.5 UV luminosity

In Fig. 5.7 the Lyα equivalent width as a function of the UV luminosity uncorrected from dust attenuation (given by SFR_{UV}) and as a function of the dust corrected UV luminosity (given by the bolometric luminosity) is shown. Note that only galaxies with $2 \leq\ z \leq 4$ are included, because galaxies with z $\geq$ 4 have an uncertain UV continuum. As described in Sec. 4.4 the dust-corrected luminosity is derived by using the continuum slope as indicator for the dust attenuation (Noll et al. 2004). The bolometric luminosity is computed from the dust-corrected luminosity by assuming a constant factor (Noll et al. 2004). Both plots seems to indicate

that strong Lyα emitters have a weaker UV continuum luminosity. Galaxies in the redshift regime $2 \leq\ z \leq 4$ and $EW_{\mathrm{Ly}\alpha} \geq 20$ Å have $SFR_{\mathrm{UV}} \approx 10$, while galaxies with $2 \leq\ z \leq 4$ and $EW_{\mathrm{Ly}\alpha} \leq 20$ Å have $SFR_{\mathrm{UV}} \approx 17$. This in agreement with Ouchi et al. (2004), who find that they strong Lyα emitters have on average a weaker continuum as their Lyman-break galaxies.

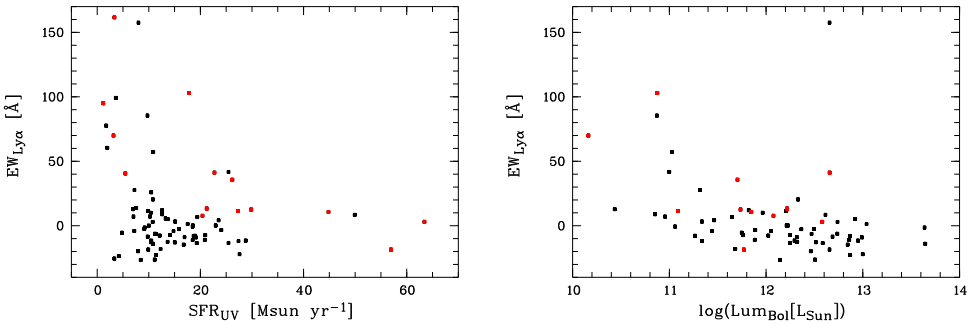

(a) **(b)**

Figure 5.7: (a) The Lyα equivalent width of the FDF spectroscopic sample (black dots) as a function of the UV star-formation rate SFR_{UV}. Red dots indicate the medium-resolution sample. (b) The Lyα equivalent width of the FDF spectroscopic sample (black dots) as a function of the bolometric luminosity for the FDF spectroscopic sample (black dots). Red dots indicate the medium-resolution sample. For both plots only galaxies with $2 \leq\ z \leq 4$ have been indicated.

Chapter 6

Discussion

6.1 Origin of the Lyα emission line

The morphology and the strength of the Lyα emission show a great range in starburst galaxies. The different strengths of the Lyα emission can be explained either by different production mechanisms or by different escape probabilities of the Lyα photons, or both. As described in Sec. 3.2.2, the intrinsic Lyα equivalent width varies for starburst galaxies, with continuous star-formation and properties of nearby galaxies only in a limited range (50 - 200 Å, Charlot & Fall 1993). The observed range of Lyα equivalent widths in the FDF spectroscopic survey ranges from -25 to 270 Å. The UV-restframe spectra of most objects analysed in this work have been explained by starburst activity. Starburst models, with continuous star-formation and properties of nearby starbursts, well describe the observed spectral properties (see Sec .3.3.2). Any high-ionisation emission lines, which indicate AGN activity has not been observed (Sec. 3.3). Most of the analysed galaxies are thus starburst galaxies. Hence their strength of the Lyα emission is determined by the escape probability of the Lyα photons. Possible exceptions are FDF-4691, FDF-9002 and FDF-9015. FDF-4691 may be an unusual BALQSO. But without further observations this cannot be determined. FDF-9002 is in the vicinity of a bright AGN. Thus FDF-9002 is probably not a starburst galaxy and the emission is powered by an AGN. The Lyα emission line of FDF-9015 is unusual broad. Moreover the $EW_{\mathrm{Ly}\alpha}$ is larger as expected from starburst activity.

In the literature a wide variety of possible mechanisms have been discussed which could determine the escape probability of the Lyα photons. The global dust content of the galaxies has been suggested as the main parameter (Kudritzki et al. 2000). The relative spatial distribution of dust, HI, and stars (Charlot & Fall 1993; Neufeld 1991) has also been suggested as the most important parameter determining the detectability of the Lyα line. Kunth et al. (1998) suggested that the kinematics of the neutral material determines the escape probability of the Lyα photons.

For FDF-4691 it was found that the low neutral column density of the surrounding shell and the large turbulence width of the central emission profile increases the escape probability of the Lyα photons. The amount of dust and the distribution of the dust has a minor influence (see Sec. 4.2.3). FDF-5215 also has a low

neutral column density and large velocity dispersion of the emission component (Sec. 4.2.4), but not all Lyα photons, which are produced in the starburst, are detected, as indicated by the Lyα equivalent width. The UV-spectrum of FDF-5215 shows that the starburst of FDF-5215 is older, also the UV-continuum is redder (see Table 3.5) indicating a more dustier environment of the galaxy.

In Sec. 5.2.1 it has been shown that the slope of the continuum is not independent of the Lyα equivalent width. The global amount of dust is indeed important for the detectability of the Lyα emission. The dust content of these galaxies is lower, thus the escape probability of the Lyα photon is increased. But a large fraction of galaxies with $\beta <$ -2 have $EW_{\mathrm{Ly}\alpha} < 20$ Å . The Lyα photons are not detected, despite the low amount of dust in the galaxies. Composite spectra of galaxies with a blue continuum were constructed. They showed that the galaxies with strong Lyα emission show no or weak interstellar absorption lines in contrast to galaxies with no or weak Lyα emission. The Lyα emission line galaxies FDF-4691 and FDF-5215 show no interstellar absorption lines.

Shapley et al. (2003) and Noll et al. (2004) found in composite spectra a strong anti-correlation between $EW_{\mathrm{Ly}\alpha}$and EW_{LIS}. In Sec. 5.1 a correlation between the EW_{LIS} and $FWHM_{\mathrm{LIS}}$ was found. The equivalent width of the interstellar absorption lines are mainly determined by the velocity dispersion of the interstellar medium. Thus the strength of the Lyα emission anti-correlates with the velocity dispersion of the outflowing material. Note that this correlation was found only for galaxies with a weak Lyα emission. Galaxies with stronger Lyα emission strengths had a too faint UV continuum to analyse the interstellar absorption lines. A higher velocity dispersion of the outflowing material has several effects on the Lyα emission. First the Lyα photons are scattered more strongly in frequency space, leading to a stronger blue-shift and red-shift of the Lyα emission peaks (see Sec. 4.1). The blue-shifted peaks are not observed due to absorption by the IGM, hence the resulting Lyα peak is redshifted. Moreover, by a given intrinsic emission profile and given mean outflow velocity more Lyα photons are absorbed, if the outflow has a higher velocity dispersion. Thus the Lyα emission is weaker and more redshifted, if the equivalent width of the interstellar absorption line increases. This is observed by Shapley et al. (2003). Shapley et al. (2003) measured the velocity offset between the Lyα line and the interstellar absorption lines in composite spectra. They found that the equivalent width of Lyα decreases with increasing velocity offset between the Lyα line and the interstellar wind lines.

Since for FDF-4691 the high line width of the central emission component allows the escape of the Lyα photons, a search was made for a possible correlation of the Lyα line width and the equivalent width (see Sec. 5.2.2). An anti-correlation of the Lyα line width and the equivalent width was found for Lyα emission galaxies with $EW_{\mathrm{Ly}\alpha} < 100$ Å . An increase of the Lyα emission width is observed in spectra with lower Lyα equivalent width. This result can be explained by a higher velocity dispersion of the outflowing material, which decreases the detectability of the Lyα emission, but scatters the Lyα photons over a broader frequency space. An alternative explanation for the anti-correlation of the Lyα line width and the Lyα equivalent width is a possible correlation of the line width with the mass of the galaxy. A higher mass could indicate a more evolved galaxy, which is likely more dust enriched. This would lead to stronger attenuation of the Lyα line.

In the model of Mas-Hesse et al. (2003) the state of ionisation of the hydrogen halo surrounding the starburst region determines the detectability of the Lyα photons (see Sec. 4.4). In Sec. 4.4 we showed that galaxies with strong Lyα emission indeed show a low amount of neutral hydrogen in the line of sight.

Almost all galaxies in the medium-resolution sample show an outflow, regardless of their Lyα emission strength. Outflow occurs in many high-redshift galaxies, possibly enriching the intra cluster medium and the intergalactic medium with metals. This is also demonstrated by FDF-5550, which shows interstellar absorption lines of another high-redshift galaxy (see Sec.3.4). Analysing the outflow velocity and the Lyα equivalent width of the medium-resolution sample show that the strength of the Lyα emission line is not independent of the outflow velocity (see Sec. 5.2.4). For a stronger outflow, there is a higher probability of stronger Lyα emission.

Several factors determine the Lyα emission strength in spectra of high-redshift galaxies. Most important are the properties of the outflowing material, its mean velocity, degree of ionisation and velocity dispersion. Galaxies with a strong Lyα emission have a lower neutral column density than galaxies with Lyα in absorption (see Sec. 4.4). They are on average smaller (see Sec. 5.2.3; Venemans et al. 2005) as galaxies selected by the Lyman-break technique. They have a weaker UV-continuum as Lyman-Break galaxies (see Sec. 5.2.5; Ouchi et al. 2004). Also the number in dark halos is higher for strong Lyα emission galaxies as for Lyman-Break galaxies (Ouchi et al. 2004). The low neutral column density, the small size and the weaker UV-continuum are consisting with a picture, where the LAEs are in a earlier state of evolution than Lyman-break galaxies. Moreover, the on average smaller galaxies have likely lower masses than Lyman-break galaxies. Hence the superwinds of galaxies with strong Lyα emission can more easily leave the potential well of the host galaxies than the superwinds of the heavier Lyman-break galaxies. The galaxies with strong Lyα have lost more metals and dust grains during the starburst. This is maybe an explanation for the strong Lyα emission. In the hierarchical model, galaxies are build up by merger of smaller galaxies. There exits the possibility that the LBG galaxies are build up by merging of galaxies with strong Lyα emission. An alternative scenario is that galaxies with strong Lyα emission evolve with time into Lyman-break galaxies.

6.2 Two populations of Lyα emission galaxies?

UV-selected galaxy samples include few galaxies with exceptionally strong Lyα emission. The samples of Shapley et al. (2003) and Noll et al. (2004) include only very few galaxies with Lyα equivalent width $EW_{\mathrm{Ly}\alpha} > 100$ Å . Lyα emission galaxies found in narrow-band surveys have often Lyα equivalent width $EW_{\mathrm{Ly}\alpha} >$ 100 Å (Hu et al. 2004; Dawson et al. 2004). Note that the UV-selected galaxies and the narrow-band selected galaxies are defined by their selection method. It is not clear whether these are two distinct populations or there is only one population. Steidel et al. (2000) compared the luminosity function of galaxies at a redshift of $z \approx 3$ found by the LBG method and by narrow-band searches, which targets galaxies with large Lyα equivalent widths and allows to detect galaxies with low continuum fluxes. Based on the results of Steidel et al. (2000), Giavalisco (2002)

concluded that both techniques see the same population of galaxies.

The FDF spectroscopic survey selected galaxies by their photometric redshifts. This is an effective way of selecting galaxies, also demonstrated by FDF-8304 (see Sec. 3.4), which was targeted for medium-resolution spectroscopy by its photometric redshift. As shown in Sec. 3.2.2 galaxies selected by the LBG have the Lyα equivalent distribution as galaxies detected by their photometric redshift. The LBG surveys and the FDF spectroscopic survey select only galaxies with a certain spectral flux in the UV continuum. Galaxies with weak continuum are not detected. FDF-1267 and FDF-9015 have no photometric redshift and were serendipitously detected during the medium-resolution spectroscopy, due to their strong emission line. Thus the possibility exists, that a fraction of high-redshift galaxies with large Lyα equivalent widths but low continuum fluxes are missed. Moreover, the distribution of the Lyα equivalent width can be described by two Gaussian distributions (3.2.2). This may indicate that two different populations exist. The Lyα equivalent width were displayed as a function of several parameters, e.g., the continuum slope β and the Lyα line width (see Chapter 5). Some combinations indicate a distinct population. E.g., for most galaxies a anti-correlation between the Lyα line width and the Lyα equivalent width was found while galaxies with a large Lyα line width were not following this trend. However since no parameter combination was found, which clearly separates the possible two populations, there is no clear evidence for two populations. A larger number of analysed galaxies could improve the situation.

Lyα equivalent widths higher than $EW_{\mathrm{Ly}\alpha} = 200$ Å are not explained by synthesis models, which assume galaxies with properties of the local universe (Charlot & Fall 1993). FDF-5812 has a Lyα equivalent width of $EW_{\mathrm{Ly}\alpha} = 270^{+91}_{-51}$ Å, but since the continuum could not be well determined the error of the Lyα equivalent width is large. Since FDF-5812 shows no indication of AGN activity or an unusual stellar population, FDF-5812 is likely a normal starburst galaxy (Sec. 3.4). Other galaxies with large equivalent widths have been detected also in other surveys (Dawson et al. 2004). But its still debated whether these measurements of the large Lyα equivalent widths are significant (Hu et al. 2004). Dawson et al. (2004) argued that some galaxies have $EW_{\mathrm{Ly}\alpha} > 200$ Å and concluded that these galaxies have properties, which are very different from those in the local universe, like having very low metalicity. The Lyα emission galaxies with a very large equivalent width are found at redshifts of $z = 4$ to 7. Noll et al. (2004) found an evolution of spectral properties of galaxies in the FDF. Galaxies at redshifts of $z = 2$ to 3 have a higher metalicity and show stronger attenuation by dust than galaxies at redshifts of $z = 3$ to 4. If this trend continue to higher redshifts, the population of galaxies at redshifts of $z = 5$ to 7 is less affected by dust and thus contain more Lyα emission galaxies. The strong Lyα emitters at redshifts of $z = 4$ to 7 have not to be a distinct population with unusual parameters, but rather a part of the UV-bright starburst population, which is on average bluer. To explain the high equivalent widths no unusual parameters like zero metalicity have to be assumed. However, without high signal-to-noise spectra of the UV continuum or further informations like the rest-frame optical spectra, the nature of the galaxies with extremely strong Lyα emission ($EW_{\mathrm{Ly}\alpha} \geq 200$ Å) remains unclear.

Chapter 7

Conclusions

R $\approx$ 2000 spectra including the Lyα line were obtained of a sample of 18 galaxies in the redshift range of $z = 2.7$ to 5 (Sec. 3.1.1). 15 of the 18 galaxies are also part of the FDF spectroscopic survey, which includes over 90 high signal-to-noise, low-resolution spectra of high-redshift galaxies. The Lyα profiles, the UV-continuum properties, the kinematics of the interstellar medium, the physical properties of the starburst and the evolutionary state of the 18 galaxies (the so-called medium-resolution sample) were derived. Moreover, the high-redshift galaxies of the FDF spectroscopic survey were analysed and their properties concerning the Lyα emission line were investigated.

The line fluxes of the Lyα emission line of the medium-resolution sample range from 6 to 190 $\times$ 10^{-21}Wm^{-2}, which converts to star-formation rates of $SFR_{\mathrm{Ly}\alpha}$ = 0.5 to 16.5 $\mathrm{M}_{\odot}\mathrm{yr}^{-1}$ (Sec. 3.2.1). The profiles of the Lyα emission lines have $FWHM$ line widths in the range of 260 to 1500 kms^{-1} (Sec. 3.2.3). Most of the lines show asymmetric profiles in the sense that the red wings are more extended and the blue wings show a sharp cutoff. In addition three Lyα lines show double-peak profiles. The observed Lyα profiles are explained by a simple model, which consists of an expanding shell surrounded by a compact starburst region (Chap. 4). The profiles were approximated by a combination of a Gauss emission line and a Voigt absorption profile. Additionally in two cases the profiles were fitted using a finite element radiative transfer code. The approach using Gauss emission lines and Voigt absorption profiles has the disadvantage of a high degeneracy of the derived parameters (Sec. 4.4). The model of a neutral shell surrounding a starburst region may oversimplify the physics, but a more sophisticated model increase the number of free parameters. The limited information on the galaxies would make it difficult to constrain the parameters. The double-peak profiles are observed when the surrounding shell is close to static. The double-peak profiles are not commonly observed in Lyα emission galaxies. This may be explained by the fact, that the intergalactic medium absorbs the blue peak. Indeed all double-peak Lyα profiles have been observed at redshifts below $z = 3.5$. The asymmetric profiles are produced, when the surrounding shell has a rather high expansion velocity. While the blue wing of the asymmetric profiles is affected by the intergalactic medium, the observed secondary peak, redshifted with respect to the main emission peak, can be explained by backscattered Lyα photons from a receding shell. This, together

with the blue-shifted interstellar absorption lines, indicates that outflows occurs frequently in the high-redshift universe.

The star-formation rates of the galaxies in the FDF spectroscopic survey derived from the UV fluxes are higher and range up to 60 $M_{\odot}yr^{-1}$(Sec. 3.1.2). The broad blue-shifted interstellar absorption lines found in the medium-resolution sample indicate a galaxy scale outflow (Sec. 3.3). A comparison of six rest-frame UV spectra of the medium-resolution sample with synthetic spectra calculated with STARBURST99 shows that the galaxies experience young continuous starbursts with SMC/LMC metalicity (Sec. 3.3.2). There is no indication for extreme metal poor starbursts, such as starbursts formed of gas with zero metalicity. For example, FDF-4691 has a strong Lyα emission line and SMC/LMC metalicity. For most of the galaxies there is no indication for an AGN activity, thus the Lyα emission is produced by the starburst. Since the intrinsic Lyα equivalent width for starburst galaxies, assuming continuous star-formation and properties of nearby galaxies, is much larger than the observed one, many Lyα photons are absorbed by dust (Sec. 3.2.2). Thus the strength of the Lyα line is determined by the escape probability of the Lyα photons.

To determine the properties which influence the strength of the Lyα emission line, spectral properties were analysed for possible correlations (Chap. 5). Dust attenuated galaxies with a strong Lyα emission line have not been found in the FDF spectroscopic survey, thus the global amount of dust is indeed important for the detectability of the Lyα emission (Sec. 5.2.1). However, also galaxies with low dust attenuation, which show no or only a weak Lyα line in emission, have been found. The total amount of dust is not the only parameter, which determines the detection of the Lyα emission. The kinematic of the outflowing material also determines the strength of the Lyα emission line (Sec. 5.2.1). Since the equivalent width of the interstellar medium was found to be correlating with the velocity dispersion of the interstellar medium (see Sec. 5.1), the velocity dispersion of the interstellar medium plays an important role of the detectability of the Lyα photons. There are indications in the medium-resolution sample that the strength of the Lyα emission is not independent of the outflow velocity (Sec. 5.2.4) and the degree of ionisation of the outflowing material (Sec. 4.4). However, the correlations were found mainly for galaxies with a strong UV continuum and a weak Lyα emission line. It is remains unclear, whether this conclusions are still valid for galaxies with much stronger Lyα emission.

It was found that galaxies in the FDF spectroscopic survey with strong Lyα emission have a lower neutral column density, are smaller, and have a weaker UV-continuum than galaxies with a weaker Lyα emission. This indicates that galaxies with strong Lyα emission are in a earlier state of evolution than Lyman-break galaxies. Moreover, the on average smaller galaxies have likely lower masses as Lyman-break galaxies at the same redshift. The galaxies with strong Lyα may have lost more metals and dust grains during the starburst, because of the lower potential. This could reduce the dust attenuation of the galaxies further. In the hierarchical model, galaxies are build up by merger of smaller galaxies, thus the possibility exists that the Lyman-break galaxies are build up by merging of galaxies with strong Lyα emission. An alternative scenario is that galaxies with strong Lyα emission evolve with time into Lyman-break galaxies.

The distribution of the Lyα equivalent widths of the FDF spectroscopic survey indicates that a distinct population with strong Lyα emission exists (Sec. 3.2.2). Furthermore the Lyα equivalent width has been plotted as a function of several parameters, e.g., the continuum slope β and the Lyα line width (Chap. 5). Some combinations, e.g., the Lyα line width and the Lyα equivalent width, indicate a distinct population. However since no parameter combination was found, which clearly separates the possibly two populations, there is no clear evidence for two populations.

Appendix A

Tables

Table A.1: Log of 1400V observations. Seeing is from Astronomical Site Monitor. The airmass gives the amount of air in the line of sight during the observations in units of the zenith airmass.

Date [UT]	Exposure time [s]	Seeing["]	Airmass
06.08.2002	2814	0.66	1.01
13.08.2002	2814	0.73	1.61
13.08.2002	2814	0.68	1.30
13.08.2002	2814	0.68	1.11
13.08.2002	2814	0.71	1.03
14.08.2002	2814	1.15	1.14
14.08.2002	2814	1.025	1.05
15.08.2002	2814	0.81	1.20

Table A.2: Log of 1200R observations. Seeing is from Astronomical Site Monitor. The airmass gives the amount of air in the line of sight during the observations in units of the zenith airmass.

Date [UT]	Exposure time [s]	Seeing["]	Airmass
29.07.2003	2759	0.78	1.31
29.07.2003	2759	0.97	1.15
08.08.2003	2159	0.85	1.33
19.09.2003	2699	1.03	1.01
20.09.2003	2759	0.95	1.11
20.09.2003	2759	1.15	1.03
23.09.2003	2759	0.78	1.04
23.09.2003	2759	0.81	1.05
24.09.2003	2159	0.81	1.02
24.09.2003	2159	0.84	1.08
24.09.2003	2759	0.77	1.18
24.09.2003	2159	0.92	1.35
28.09.2003	2759	1.13	1.08
28.09.2003	2759	1.07	1.02

Table A.3: List of objects observed with 1400V grism. The object number (ID), right ascension [h:min:sec], declination [deg:arcmin:arcsec], and apparant magnitude $m_{\mathrm{R}}$are taken from Heidt et al. (2003). Coordinates of FDF-9002 are taken from Noll et al. (2004). In addition the average continuum signal-to-noise ratio is given.

ID	RA(2000)	Dec(2000)	m_{R}	wavelength range [Å]	SNR
0511	01:05:49.08	-25:48:41.3	20.0	4319.0 - 5605.0	70.37
1267	01:05:52.103	-25:48:39.2	27.08	4385.5 - 5550.0	0.36
1331	01:05:52.376	-25:47:29.0	24.8	4302.0 - 5397.5	0.67
1337	01:05:52.401	-25:48:33.4	24.15	4385.5 - 5550.0	3.53
1383	01:05:52.619	-25:48:29.5	24.53	4385.5 - 5550.0	5.43
2368	01:05:56.277	-25:48:21.5	24.96	4458.0 - 5757.5	1.17
2384	01:05:56.327	-25:47:37.1	24.61	4390.0 - 5684.0	2.61
3810	01:06:1.318	-25:45:27.9	23.41	4314.0 - 5604.5	6.52
4115	01:06:2.378	-25:47:24.8	22.35	4528.0 - 5826.0	27.57
4186	01:06:2.61	-25:47:23.9	24.97	4528.0 - 5826.0	2.47
4454	01:06:3.605	-25:45:28.7	26.11	4372.5 - 5664.5	0.65
4683	01:06:4.392	-25:46:51.3	19.16	4522.5 - 5824.5	296.82
4691	01:06:4.421	-25:48:34.4	24.79	4685.0 - 5996.5	3.78
5215	01:06:6.245	-25:45:4.1	24.53	4403.5 - 5694.5	3.01
5550	01:06:7.515	-25:47:0.4	23.95	4615.5 - 5922.5	3.78
5744	01:06:8.21	-25:45:33.8	24.81	4499.0 - 5797.5	2.05
5903	01:06:8.785	-25:44:54.5	23.14	4457.0 - 5750.0	12.27
6024	01:06:9.227	-25:48:14.1	23.0	4778.5 - 6093.5	10.28
6063	01:06:9.362	-25:48:7.4	23.37	4778.5 - 6086.5	4.18
6934	01:06:12.364	-25:44:56.8	23.99	4553.5 - 5851.0	4.24
7539	01:06:14.433	-25:47:8.4	24.1	4809.0 - 6123.5	3.45
9002	01:06:04.30	-25:46:55		4522.5 - 5826.5	0.88

Table A.4: List of objects observed with 1200R grism. The object number (ID), right ascension [h:min:sec], declination [deg:arcmin:arcsec], and apparant magnitude m_R are taken from Heidt et al. (2003). In addition the average continuum signal-to-noise ratio is given.

ID	RA (2000)	Dec(2000)	m_R	Wavelength range [Å]	SNR
672	01:05:49.8	-25:44:59.0	22.29	6026.5 - 7527.0	38.65
960	01:05:50.924	-25:45:37.2	24.31	5920.5 - 7420.5	3.96
970	01:05:50.967	-25:45:37.7	25.02	5920.5 - 7420.5	2.8
1064	01:05:51.352	-25:45:39.7	23.88	5917.0 - 7416.0	9.6
1337	01:05:52.401	-25:48:33.4	24.15	5436.0 - 6908.0	4.72
1474	01:05:52.928	-25:45:23.5	24.47	5974.0 - 7482.0	2.82
1502	01:05:53.05	-25:45:22.8	24.3	5970.0 - 7482.0	3.96
1555	01:05:53.263	-25:45:20.8	24.48	5974.0 - 7482.0	1.99
2384	01:05:56.327	-25:47:37.1	24.61	5611.5 - 7090.0	3.01
3173	01:05:59.188	-25:46:25.8	24.48	5821.0 - 7316.0	4.29
3312	01:05:59.661	-25:47:43.7	24.51	5610.5 - 7089.5	2.75
3389	01:05:59.924	-25:44:39.9	25.57	6125.0 - 7637.5	0.71
3741	01:06:1.074	-25:48:35.1	24.32	5478.0 - 6947.0	3.37
4682	01:06:4.392	-25:46:15.3	24.71	5877.0 - 7375.5	3.37
5215	01:06:6.245	-25:45:4.1	24.53	6089.0 - 7600.0	3.98
5504	01:06:7.328	-25:46:59.0	24.82	5761.0 - 7263.5	2.23
5550	01:06:7.515	-25:47:0.4	23.95	5761.5 - 7259.5	6.47
5812	01:06:8.493	-25:44:16.7	27.55	6237.0 - 7756.0	0.69
6063	01:06:9.362	-25:48:7.4	23.37	5597.5 - 7075.0	5.83
6557	01:06:11.087	-25:47:32.6	25.95	5702.0 - 7186.5	0.69
7341	01:06:13.695	-25:46:11.9	24.85	5943.0 - 7441.5	2.04
7452	01:06:14.138	-25:46:12.6	24.98	5943.0 - 7442.0	2.2
7539	01:06:14.433	-25:47:8.4	24.1	5791.0 - 7279.0	4.88
7683	01:06:14.931	-25:47:30.0	24.93	5735.0 - 7218.5	2.2
8304	01:06:17.261	-25:46:14.7	24.98	5958.5 - 7457.0	3.37
8360	01:06:17.498	-25:46:14.1	23.09	5958.0 - 7457.0	3.63
9015	01:06:16.859	-25:46:12.97		5959.5 - 7457.5	1.23

Table A.5: List of high-redshift galaxies with medium-resolution spectra. The redshift and the covered wavelength range in the rest-frame of the galaxies is shown

ID	z	Wavelength range 1400V [Å]	Wavelength range 1200R [Å]
960	3.16		1423.40 - 1784.03
970	3.16		1424.09 - 1784.89
1267	2.78	1157.80 - 1465.23	
1337	3.4	996.14 - 1260.65	1234.75 - 1569.11
1555	3.27		1399.69 - 1753.00
2384	3.31	1017.55 - 1317.48	1300.67 - 1643.37
3173	3.27		1363.17 - 1713.27
3312	3.39		1278.43 - 1615.44
3389	4.58		1097.18 - 1368.11
3741	2.64		1505.23 - 1908.88
3810	2.37	1279.47 - 1662.22	
4454	3.09	1070.27 - 1386.52	
4682	3.14		1418.61 - 1780.32
4691	3.3	1088.62 - 1393.37	
5215	3.15	1061.60 - 1372.83	1467.94 - 1832.21
5550	3.38	1053.07 - 1351.27	1314.54 - 1656.30
5744	3.4	1022.24 - 1317.28	
5812	4.99		1040.42 - 1293.81
5903	2.77	1180.88 - 1523.46	
6024	2.37	1417.15 - 1807.14	
6063	3.4	1086.84 - 1384.33	1273.11 - 1609.16
6557	4.68		1003.48 - 1264.74
6934	2.44	1321.77 - 1698.4	
7452	3.15		1433.46 - 1795.03
7539	3.29	1121.66 - 1428.25	1350.70 - 1697.77
7683	3.78		1199.49 - 1509.77
8304	4.2		1144.76 - 1432.66
9002	3.35	1033.79 - 1331.86	
9015	3.96		1201.40 - 1503.52

Table A.6: UV spectral luminosity $L_{\rm UV}$, star-formation rate $SFR_{\rm UV}$ and continuum slope β of the medium-resolution sample (galaxies with the Lyα line in one of the medium-resolution grism).

ID	$L_{\rm UV}[10^{34}$ WÅ^{-1}]	$SFR_{\rm UV}[{\rm M}_\odot{\rm yr}^{-1}]$	β
1267	0.13 ± 0.02	1.16 ± 0.15	
1337	2.60 ± 0.11	27.28 ± 1.15	- 1.89
2384	2.17 ± 0.07	22.74 ± 0.77	-0.55
3389	1.41 ± 0.24	14.85 ± 2.47	
4454	0.30 ± 0.05	3.17 ± 0.50	-2.42
4691	1.70 ± 0.07	17.88 ± 0.75	-2.46
5215	2.49 ± 0.08	26.20 ± 0.80	-1.71
5550	4.26 ± 0.10	44.78 ± 1.07	-1.81
5744	2.02 ± 0.08	21.23 ± 0.87	- 1.02
5812	0.62 ± 0.16	5.21 ± 1.31	
5903	6.01 ± 0.07	63.14 ± 0.75	-1.15
6063	5.39 ± 0.13	56.61 ± 1.28	-2.01
6557	1.51 ± 0.15	13.85 ± 1.39	
7539	2.84 ± 0.07	29.87 ± 0.78	- 1.74
7683	1.94 ± 0.14	20.40 ± 1.46	-1.16
8304	2.22 ± 0.02	23.28 ± 0.23	
9002	5.17 ± 0.94	5.43 ± 0.99	
9015	0.39 ± 0.06	3.35 ± 0.49	

Table A.7: The Lyα fluxes $F_{\rm Ly\alpha}$ the Lyα luminosity $L_{\rm Ly\alpha}$, the star-formation rate $SFR_{\rm Ly\alpha}$and the Lyα equivalent width $EW_{\rm Ly\alpha}$ of the medium-resolution sample (defined as galaxies with the Lyα line in one of the medium-resolution grism).

ID	$F_{\rm Ly\alpha}[10^{-21}{\rm Wm}^{-2}]$	$L_{\rm Ly\alpha}[10^{35}$ Wm$^{-2}]$	$SFR_{\rm Ly\alpha}[{\rm M}_\odot{\rm yr}^{-1}]$	$EW_{\rm Ly\alpha}$[Å]
1267	19.82 ± 2.98	1.28 ± 1.92	1.16 ± 1.16	95 ± 22
1337	24.47 ± 1.31	2.59 ± 0.14	2.35 ± 0.12	11.37 ± 1.90
2384	66.08 ± 2.65	6.48± 0.26	5.89 ± 0.24	41.17 ± 4.42
3389	48.01 ± 1.97	10.14 ± 0.42	9.2 ± 0.38	50.60 ± 9.17
4454	28.48 ± 1.11	2.35 ± 0.09	2.13 ± 0.08	69.93 ± 14.18
4691	185.81 ± 2.86	18.06 ± 0.28	16.44 ± 0.25	103 ± 15
5215	106.26 ± 2.91	9.19 ± 0.25	8.36 ± 0.22	35.70 ± 2.57
5550	35.84 ± 1.66	3.68 ± 0.17	3.35 ± 0.16	10.72 ± 1.52
5744				-4.34 ± 3.99
5812	65.58 ± 3.01	16.95 ± 0.07	15.42 ± 0.71	270^{+91}_{-51}
5903	8.24 ± 1.58	5.26 ± 1.00	0.48 ± 0.09	3.05 ± 1.07
6063				-18.53 ± 1.78
6557	32.42 ± 3.38	7.20 ± 0.75	6.55 ± 0.68	37.54 ± 14.75
7539	34.02 ± 2.40	3.26 ± 0.23	2.98 ± 0.21	12.54 ± 1.59
7683	10.09 ± 3.12		1.35 ± 0.41	7.73 ± 3.86
8304	6.53 ± 0.64	1.12 ± 0.11	1.02 ± 0.10	7.2 ± 2.18
9002	20.63 ± 2.72	2.11 ± 0.27	1.92 ± 0.25	40.61 ± 10.00
9015	40.05 ± 1.19	5.98 ± 0.18	5.44± .16	161.70 ± 32.74

Table A.8: The line widths ($FWHM$) , the asymmetrie parameters $a_{\rm wave}$and $a_{\rm flux}$of the Lyα lines of the medium-resolution sample.

ID	FWHM [kms^{-1}]	$a_{\rm wave}$	$a_{\rm flux}$
1267	235± 34	1.04 ± 0.26	1.24 ± 0.23
1337	597± 84	1.39 ± 0.24	1.19± 0.16
2384	283± 47	3.00± 0.57	2.03 ± 0.12
3389	354± 70	3.82 ± 1.46	2.29 ± 0.27
4454	323± 47	2.1 ± 0.79	1.37± 0.25
4691	840± 115	1.02 ± 0.06	1.37± 0.07
5215	483 ± 90	1.21 ± 0.38	0.94± 0.22
5550	424± 85	2.04 ± 0.55	1.71 ± 0.23
5744			
5812	226± 23	3.01± 0.89	2.66 ± 0.26
5903	627 ± 140		
6063			
6557	380 ± 135		
7539	1430± 230	2.12 ± 0.56	2.46 ± 0.31
7683	435 ± 70	1.95 ± 0.5	1.58 ± 0.4
8304	500 ± 100		
9002	480 ± 116	1.03 ± 0.23	0.95 ± 0.19
9015	970 ± 103	1.42 ± 0.14	1.09 ± 0.1

Table A.9: Equivalent width of the interstellar absorption lines SiII λ 1261, OI/SiII λ 1303, and CIIλ 1335.

ID	EW(SiII λ1261) [Å]	EW(OI/SiII λ1303) [Å]	EW(CIIλ 1335) [Å]
1337	- 2.03 ± 0.42	- 1.68 ± 0.4	- 1.62 ± 0.25
4691			- 3.0 ± 0.92
5550	- 2.61 ± 0.27	- 2.95 ± 0.70	- 2.07 ± 0.55
5744	-2.62 ± 0.43	-2.61 ± 1.1	-2.57 ± 1.52
5903	-2.54 ± 0.26	-3.53 ± 0.29	-2.96 ± 0.22
6063	-2.52 ± 0.59	-2.84 ± 0.65	-2.57 ± 0.66
7539	-1.4 ± 0.34	-1.14 ± 0.3	-1.17 ± 0.35
8304	-1.81 ± 0.32	-1.83 ± 0.38	-2.53 ± 0.44

Table A.10: Equivalent width of the interstellar absorption lines SiII λ1526, FeII λ1608, AlII λ1671 and AlIII $\lambda\lambda$ 1856,1863.

ID	EW(SiII) [Å]	EW(FeII) [Å]	EW(AlII) [Å]	EW(AlIII) [Å]
1337	- 0.95 ± 0.77			
5550	- 2.06 ± 0.55		1.33 ± 0.85	
5744			2.37 ± 1.70	-4.12 ± 2.22
5903	-2.2 ± 0.32	- 1.29 ± 0.34	-1.06 ± 0.65	-2.03 ± 0.6
6063	-1.37 ± 0.67	-2.67 ± 0.66		

Table A.11: Equivalent width of the lines SiIV $\lambda\lambda$1394,1403 and CIV $\lambda\lambda$1548, 1501. CIV $\lambda\lambda$1548, 1501 is separated into an absorption component and an emission component.

ID	EW(SiIV) [Å]	EW(CIV_{abs}) [Å]	EW(CIV_{em}) [Å]
1337		-1.47 ± 0.94	2.5 ± 1.42
4691	- 3.89 ± 1.42	-3.3 ± 0.93	3.52 ± 1.27
5215		-1.66 ± 0.67	1.56 ± 0.99
5550	- 3.72 ± 0.80	- 2.49 ± 0.69	
5744		-1.89 ± 1.00	
5903	-3.99 ± 0.38	-3.89 ± 0.41	
6063	-3.27 ± 0.7	-2.15 ± 0.68	
7539	-2.42 ± 0.36	-2.35 ± 0.39	

Table A.12: The equivalent width of Lyβ and SV* λ1501.76 are given.

ID	EW(Lyβ) [Å]	EW(1502) [Å]
4691	-7.2 ± 1.43	
5550	-14.04 ± 1.5	1.51 ± 0.54
5903	-5.04 ± 1.21	0.53 ± 0.25

Table A.13: The equivalent widths and fluxes of HeII λ1640 and of CIII] λ1909 are listed.

ID	EW(1640) [Å]	F(1640) [10^{-21}Wm^{-2}]	EW(1909) [Å]	F(1909) [10^{-21}Wm^{-2}]
4691	3.46 ± 1.82	4.30 ± 1.61	10.07 ± 4.55	8.55 ± 1.85
5903	1.96 ± 0.56	16.9 ± 3.9		
6063	2.14 ± 1.18	9.21 ± 4.01		
7539			7.67 ± 2.63	

Bibliography

Adams, T. F. 1972, ApJ, 174, 439

—. 1975, ApJ, 201, 350

Adelberger, K. L., Steidel, C. C., Shapley, A. E., & Pettini, M. 2003, ApJ, 584, 45

Ahn, S. 2004, ApJ, 601, L25

Ahn, S., Lee, H., & Lee, H. M. 2001, ApJ, 554, 604

—. 2002, ApJ, 567, 922

—. 2003, MNRAS, 340, 863

Ajiki, M., Taniguchi, Y., Fujita, S. S., et al. 2003, AJ, 126, 2091

—. 2004, PASJ, 56, 597

Ajiki, M., Taniguchi, Y., Murayama, T., et al. 2002, ApJ, 576, L25

Appenzeller, I., Bender, R., Bohm, A., et al. 2000, The Messenger, 100, 44

Appenzeller, I., Fricke, K., Furtig, W., et al. 1998, The Messenger, 94, 1

Appenzeller, I., Stahl, O., Tapken, C., Mehlert, D., & Noll, S. 2005, ArXiv Astrophysics e-prints

Auer, L. H. 1968, ApJ, 153, 783

Bender, R., Appenzeller, I., Böhm, A., et al. 2001, in Deep Fields, 96–+

Bentz, M. C., Osmer, P. S., & Weinberg, D. H. 2004, ApJ, 600, L19

Bithell, M. 1991, MNRAS, 253, 320

Bouchet, P., Lequeux, J., Maurice, E., Prevot, L., & Prevot-Burnichon, M. L. 1985, A&A, 149, 330

Calzetti, D., Armus, L., Bohlin, R. C., et al. 2000, ApJ, 533, 682

Calzetti, D., Kinney, A. L., & Storchi-Bergmann, T. 1994, ApJ, 429, 582

Castor, J., McCray, R., & Weaver, R. 1975, ApJ, 200, L107

Chapman, S. C., Blain, A. W., Smail, I., & Ivison, R. J. 2004, ArXiv Astrophysics e-prints

Charlot, S. & Fall, S. M. 1993, ApJ, 415, 580

Chen, W. L. & Neufeld, D. A. 1994, ApJ, 432, 567

Christensen, L., Sánchez, S. F., Jahnke, K., et al. 2004, A&A, 417, 487

Dawson, S., Rhoads, J. E., Malhotra, S., et al. 2004, ApJ, 617, 707

Dawson, S., Spinrad, H., Stern, D., et al. 2002, ApJ, 570, 92

Djorgovski, S. G., Pahre, M. A., Bechtold, J., & Elston, R. 1996, Nature, 382, 234

Draine, B. T. & Salpeter, E. E. 1979, ApJ, 231, 438

Ferguson, H. C., Dickinson, M., Giavalisco, M., et al. 2004, ApJ, 600, L107

Fosbury, R. A. E., Villar-Martín, M., Humphrey, A., et al. 2003, ApJ, 596, 797

Frank, S., Appenzeller, I., Noll, S., & Stahl, O. 2003, A&A, 407, 473

Franx, M., Illingworth, G. D., Kelson, D. D., van Dokkum, P. G., & Tran, K. 1997, ApJ, 486, L75+

Fynbo, J. P. U., Ledoux, C., Möller, P., Thomsen, B., & Burud, I. 2003, A&A, 407, 147

Gabasch, A., Bender, R., Seitz, S., et al. 2004a, A&A, 421, 41

Gabasch, A., Salvato, M., Saglia, R. P., et al. 2004b, ArXiv Astrophysics e-prints

Giavalisco, M. 2002, ARA&A, 40, 579

Giavalisco, M., Koratkar, A., & Calzetti, D. 1996, ApJ, 466, 831

Hall, P. B., Hoversten, E. A., Tremonti, C. A., et al. 2004, AJ, 127, 3146

Heckman, T. M., Armus, L., & Miley, G. K. 1990, ApJS, 74, 833

Heckman, T. M., Lehnert, M. D., & Armus, L. 1993, in ASSL Vol. 188: The Environment and Evolution of Galaxies, 455–+

Heckman, T. M., Robert, C., Leitherer, C., Garnett, D. R., & van der Rydt, F. 1998, ApJ, 503, 646

Heidt, J., Appenzeller, I., Gabasch, A., et al. 2003, A&A, 398, 49

Horne, K. 1986, PASP, 98, 609

Hu, E. M., Cowie, L. L., Capak, P., et al. 2004, AJ, 127, 563

Hu, E. M. & McMahon, R. G. 1996, Nature, 382, 231

Inoue, A. K., Iwata, I., Deharveng, J. ., Buat, V., & Burgarella, D. 2005, ArXiv Astrophysics e-prints

Kennicutt, R. C. 1998, ARA&A, 36, 189

Kudritzki, R.-P., Méndez, R. H., Feldmeier, J. J., et al. 2000, ApJ, 536, 19

Kunth, D., Mas-Hesse, J. M., Terlevich, E., et al. 1998, A&A, 334, 11

Larsen, S. S., Brodie, J. P., & Hunter, D. A. 2004, AJ, 128, 2295

Leitherer, C., Leão, J. R. S., Heckman, T. M., et al. 2001, ApJ, 550, 724

Leitherer, C., Li, I.-H., Calzetti, D., & Heckman, T. M. 2002, ApJS, 140, 303

Leitherer, C., Schaerer, D., Goldader, J. D., et al. 1999, ApJS, 123, 3

Lequeux, J., Kunth, D., Mas-Hesse, J. M., & Sargent, W. L. W. 1995, A&A, 301, 18

Madau, P. 1995, ApJ, 441, 18

Maier, C., Meisenheimer, K., Thommes, E., et al. 2003, A&A, 402, 79

Malhotra, S. & Rhoads, J. E. 2002, ApJ, 565, L71

Mas-Hesse, J. M., Kunth, D., Tenorio-Tagle, G., et al. 2003, ApJ, 598, 858

Matsuda, Y., Yamada, T., Hayashino, T., et al. 2004, AJ, 128, 569

Mehlert, D., Noll, S., Appenzeller, I., et al. 2002, A&A, 393, 809

Meinköhn, E. 2002, Ph.D. Thesis

Meinköhn, E. & Richling, S. 2002, A&A, 392, 827

Meynet, G. & Maeder, A. 2005, A&A, 429, 581

Mihalas, D. 1978, Stellar atmospheres /2nd edition/ (San Francisco, W. H. Freeman and Co., 1978. 650 p.)

Neufeld, D. A. 1990, ApJ, 350, 216

—. 1991, ApJ, 370, L85

Noll, S. 2002, Ph.D. Thesis

Noll, S., Mehlert, D., Appenzeller, I., et al. 2004, A&A, 418, 885

Noll, M. et al. 2005, in prep.

Osterbrock, D. E. 1962, ApJ, 135, 195

—. 1989, Astrophysics of gaseous nebulae and active galactic nuclei (Research supported by the University of California, John Simon Guggenheim Memorial Foundation, University of Minnesota, et al. Mill Valley, CA, University Science Books, 1989, 422 p.)

Ouchi, M., Shimasaku, K., Okamura, S., et al. 2004, ApJ, 611, 685

Pannella, M. et al. 2005, in prep.

Partridge, R. B. & Peebles, P. J. E. 1967, ApJ, 147, 868

Pettini, M., Shapley, A. E., Steidel, C. C., et al. 2001, ApJ, 554, 981

Pettini, M., Steidel, C. C., Adelberger, K. L., Dickinson, M., & Giavalisco, M. 2000, ApJ, 528, 96

Pritchet, C. J. 1994, PASP, 106, 1052

Rhoads, J. E., Dey, A., Malhotra, S., et al. 2003, AJ, 125, 1006

Rhoads, J. E., Xu, C., Dawson, S., et al. 2004, ApJ, 611, 59

Richling, S. 2003, MNRAS, 344, 553

Richling, S., Meinköhn, E., Kryzhevoi, N., & Kanschat, G. 2001, A&A, 380, 776

Savage, B. D. & Mathis, J. S. 1979, ARA&A, 17, 73

Schaerer, D. 2003, A&A, 397, 527

Schneider, D. P., Fan, X., Hall, P. B., et al. 2003, AJ, 126, 2579

Shapley, A. E. 2003, Ph.D. Thesis

Shapley, A. E., Steidel, C. C., Pettini, M., & Adelberger, K. L. 2003, ApJ, 588, 65

Spergel, D. N., Verde, L., Peiris, H. V., et al. 2003, ApJS, 148, 175

Steidel, C. C., Adelberger, K. L., Shapley, A. E., et al. 2000, ApJ, 532, 170

Steidel, C. C., Giavalisco, M., Pettini, M., Dickinson, M., & Adelberger, K. L. 1996, ApJ, 462, L17+

Steidel, C. C., Pettini, M., & Adelberger, K. L. 2001, ApJ, 546, 665

Stern, D., Moran, E. C., Coil, A. L., et al. 2002, ApJ, 568, 71

Taniguchi, Y., Shioya, Y., Ajiki, M., et al. 2003, Journal of Korean Astronomical Society, 36, 123

Tapken, C., Appenzeller, I., Mehlert, D., Noll, S., & Richling, S. 2004, A&A, 416, L1

Tenorio-Tagle, G., Silich, S. A., Kunth, D., Terlevich, E., & Terlevich, R. 1999, MNRAS, 309, 332

Thommes, E. & Meisenheimer, K. 2005, A&A, 430, 877

Thompson, D. & Djorgovski, S. G. 1995, AJ, 110, 982

van Ojik, R., Roettgering, H. J. A., Miley, G. K., & Hunstead, R. W. 1997, A&A, 317, 358

Venemans, B. P., Röttgering, H. J. A., Overzier, R. A., et al. 2004, A&A, 424, L17

Venemans, B. P., Rottgering, H. J. A., Miley, G. K., et al. 2005, ArXiv Astrophysics e-prints

Walborn, N. R. & Panek, R. J. 1984a, ApJ, 280, L27

—. 1984b, ApJ, 286, 718

Wang, J. X., Rhoads, J. E., Malhotra, S., et al. 2004, ApJ, 608, L21

Wehrse, R., Baschek, B., & von Waldenfels, W. 2002, A&A, 390, 1141

Westra, E., Jones, D. H., Lidman, C. E., et al. 2004, ArXiv Astrophysics e-prints

White, S. D. M. & Rees, M. J. 1978, MNRAS, 183, 341

Wiese, W. L., Smith, M. W., & Glennon, B. M. 1966, Atomic transition probabilities. Vol.: Hydrogen through Neon. A critical data compilation (NSRDS-NBS 4, Washington, D.C.: US Department of Commerce, National Buereau of Standards, 1966)

Willis, A.J. & Garmany, C.D. 1989, "Wolf-Rayet Stars" in Exploring the Universe with the IUE Satellite, eds. Y.Konda et al., 1989 Kluwer, p. 157

Wu, C.-C., Ake, T. B., Boggess, A., et al. 1983, "The IUE Ultraviolet Spectral Atlas", NASA Newsletter, No. 22

Zanstra, H. 1949, Bull. Astron. Inst. Netherlands, 11, 1

Danksagung

An dieser Stelle möchte ich mich ganz herzlich bei allen bedanken, die mich bei dieser Arbeit unterstützt haben.

Ich danke zuerst Prof. Dr. Immo Appenzeller, der diese Arbeit erst möglich gemacht hat. Trotz seiner zahllosen Verpflichtungen hat er immer Zeit gehabt, meine vielen Fragen ausführlich zu beantworten und wichtige Hilfestellungen zu geben.

Weiterhin danke ich

- Prof. Dr. Klaus Meisenheimer für die Erstellung des Zweitgutachtens
- Stefan Noll für zahlreiche Diskussionen und das Lesen der Doktorarbeit
- Dörte Mehlert für die zahlreichen Diskussionen
- Sabine Richling für die Herstellung der Finiten Elemente Modelle und der guten Zusammenarbeit und die vielen Diskussionen
- Erik Meinköhn für die Hilfen beim Verständnis des Finiten Elementen Codes
- Claus Möllenhoff für die vielen Diskussionen am Mittagstisch
- Otmar Stahl für die zahlreichen Hilfen bei Computerproblemen und der Unterstützung bei der Fehlerbeseitigung der Reduktionsroutinen
- Jochen Heidt für die vielen Antworten auf meine Fragen
- Stella Seitz, Armin Gabasch und Maurilio Pannela für die Zusammenarbeit bei der Photometrie und Morphologie des FDF und für viele Diskussionen
- allen Mitgliedern des FORS Deep Field Teams, die durch ihre harte Arbeit die Grundlage für diese Untersuchung geliefert haben
- der ESO
- den Mitarbeitern der Landessternwarte für die angenehme Atmosphäre und gute Zusammenarbeit
- Tilmann Althaus für das Lesen der Arbeit
- Gabriela Grüninger für ihre Unterstützung
- meinen Eltern für ihren Zuspruch und ihr Vertrauen